Title
Combining Calorimetry and Electrochemical Methods to Gain Insight Into the Charging Mechanisms of Electrochemical Capacitors and Batteries

Author
Frajnkovic, Matevz

Publication Date
2022

Peer reviewed|Thesis/dissertation

UNIVERSITY OF CALIFORNIA

Los Angeles

Combining Calorimetry and Electrochemical Methods to Gain Insight Into the Charging Mechanisms of Electrochemical Capacitors and Batteries

A dissertation submitted in partial satisfaction
of the requirements for the degree
Doctor of Philosophy in Mechanical Engineering

by

Matevz Frajnkovic

2022

ABSTRACT OF THE DISSERTATION

Combining Calorimetry and Electrochemical Methods to Gain Insight Into the Charging Mechanisms of Electrochemical Capacitors and Batteries

by

Matevz Frajnkovic
Doctor of Philosophy in Mechanical Engineering
University of California, Los Angeles, 2022
Professor Laurent G. Pilon, Chair

Increased demand for electrical energy storage to support the deployment of renewable energy sources and to decarbonize the transportation sector has established electrochemical capacitor (EC) and rechargeable batteries as the current frontier of science. Accurate understanding of the phenomena occurring during cycling of ECs and batteries can assist in determining their limitations, in optimizing their design and the material selection and in developing novel electrode materials. Recently, isothermal *operando* calorimetry has been successfully developed to identify the charging mechanisms occurring in ECs and batteries. It has identified the thermal signatures of (i) Joule heating, (ii) EDL formation/dissolution, (iii) redox reactions, (iv) overscreening effect, (v) electrolyte decomposition, (vi) irreversible ion intercalation into the electrode, and (vii) insulator to semiconductor transition.

Heat generation rates in hybrid supercapacitors consisting of positive α-MnO_2 cryptomelane electrodes and AC counter electrodes with different aqueous electrolytes were measured experimentally via isothermal *operando* calorimetry under galvanostatic cycling at 20 °C. First, two devices with 0.5 M K_2SO_4 or Cs_2SO_4 aqueous electrolytes were investigated for their different solvation shell thickness and bare ion size. The measured heat generation rate at the AC electrode was attributed to irreversible Joule heating and reversible EDL formation/dissolution. On the other hand, the heat generation rate at the α-MnO_2 electrode was caused by Joule heating and redox reactions. Moreover, for large potential windows,

an endothermic dip was observed at the α-MnO_2 at the end of the charging step and was attributed to the onset of hydrolysis. Hydrolysis was observed for potential window of 2 V in 0.5 M Cs_2SO_4 aqueous electrolyte and for 1.8 V for 0.5 M K_2SO_4. The wider potential window than the theoretical 1.23 V was attributed to the thinner solvation shell of Cs^+ compared to K^+ which limited the amount of water present near the electrode.

Heat generation rate measured in hybrid supercapacitors is often dominated by ion adsorption/desorption and redox reactions. However, during adsorption/desorption and redox reactions, ions fully or partially shed or form their solvation shells. Here, hybrid supercapacitors consisting of an α-MnO_2 and an AC electrode with $MgSO_4$ aqueous electrolytes with different concentrations were investigated via isothermal *operando* calorimetry. $MgSO_4$ salt was chosen for its high solubility in water ($\leq$ 2.9 M at 20 °C) near neutral pH and its large enthalpy of solvation compared to previously considered K_2SO_4 and Cs_2SO_4. The measured heat generation rates at the AC electrodes were similar to those previously measured in devices with K_2SO_4 and Cs_2SO_4 aqueous electrolytes. However, the heat generation rate measured at the α-MnO_2 electrodes was significantly different from those observed for K_2SO_4 and Cs_2SO_4 aqueous electrolytes. This was attributed to the heat generation due to solvation/desolvation of Mg^{2+} cations. However, the thermal signature of solvation was not observed at the AC electrode as the solvated Mg^{2+} cations were small enough to enter the pores in the AC electrodes without becoming partially desolvated. This interpretation was confirmed by a simple thermal model.

Ion size can also affect the charging mechanisms and capacity of hybrid supercapacitors. To assess the effect of ion size on the charging mechanisms and heat generation in hybrid supercapacitors three devices were tested and consisted of an α-MnO_2 and an AC electrode with either (i) 0.5 M Li_2SO_4, (ii) 0.5 M Na_2SO_4, or (iii) 0.5 M Cs_2SO_4 aqueous electrolyte. The thermal signatures measured at the AC electrodes in 0.5 M Na_2SO_4 and 0.5 M Cs_2SO_4 aqueous electrolyte were qualitatively similar and attributed to EDL formation/dissolution. However, they were different from the thermal signature measured in 0.5 M Li_2SO_4 aqueous electrolyte when Li^+ possibly participated in surface redox reactions with the AC electrode due to its small size and high electronegativity. Then, the heat generation rate was endother-

mic during charging due to the non-spontaneous Li^+ surface redox reactions and exothermic during discharging. Interestingly, Na^+ and Cs^+ cations did not participate in surface redox reactions into AC as their compounds with carbon are not stable.

The irreversible heat generation in the redox active α-MnO_2 electrode of hybrid supercapacitors exceeded Joule heating due to the contributions of polarization heating and the hysteretic ion concentration profile evolution at the electrode surface. This dissertation formulates expressions and performs numerical simulations of the irreversible heat generation rates associated with charge and mass transfer resistances based on the modified Poisson-Nernst-Planck model. These contributions to the total heat generation rate were expressed as resistive losses through the charge transfer or the mass transfer resistances by analogy with Joule heating. These resistances were not constant during cycling and instead depended on the state of charge of the electrode.

Finally, while batteries feature high energy density, their power density is often limited. $Li_xNa_{1.5-x}VOPV_4F_{0.5}$ (LNVOPF) has been identified as a promising high rate cathode material whose rate performance can rival that of pseudocapacitive electrodes such as α-MnO_2. This dissertation investigates the structural evolution of LNVOPF during lithiation and delithiation to elucidate the origin of its excellent rate performance. Open circuit voltage and entropic potential were measured in three different coin cells with LNVOPF cathodes and Li metal anodes in 1 M $LiPF_6$ in EC:DMC electrolyte. The cathodes consisted of either LNVOPF *micronbricks* or *nanoparticles* and were manufactured with either P3HT or PVDF as binders. The evolutions of open circuit voltage and entropic potential indicated that LNVOPF exhibits solid solution behavior with ion ordering. The device with the LNVOPF *nanoparticles* featured faster kinetics and larger apparent diffusion coefficient of Li^+ than that with LNVOPF *micronbricks*. This was attributed to the larger particle size and the large electrode resistance of the coin cell with LNVOPF *micronbricks* which retained more Na than LNVOPF *nanoparticles* after Li exchange. This interpretation was corroborated with thermodynamic calculation of the entropic potential evolution.

The dissertation of Matevz Frajnkovic is approved.

Adrienne G. Lavine

Bruce S. Dunn

Timothy S. Fisher

Laurent G. Pilon, Committee Chair

University of California, Los Angeles

2022

To Esther and Vasya Frajnkovič

TABLE OF CONTENTS

LIST OF FIGURES

LIST OF TABLES

NOMENCLATURE

a	Ion diameter, nm
A	Surface area, m^2
c	Concentration, mol/m^3
C	Capacity, mAh
C_{diff}	Differential capacitance, F
C_{eq}	Equilibrium differential capacitance, F
C_g	Gravimetric capacity, mAh/g
C_{int}	Integral capacitance, F
D	Diffusion coefficient, m^2/s
e	Elementary charge, 1.6×10^{-19} C
f	Frequency, Hz
F	Faraday constant, 96,485.33 C/mol
g	Molar Gibbs free energy, J/mol
H	Stern layer thickness, nm
I	Electric current, mA
j	Electric current density, A/m^2
k	Thermal conductivity, W/m·K
L	Thickness, μm
m	Mass loading, mg
N	Molar flux, $mol/m^2{\cdot}s$
N_A	Avogadro number, 6.022×10^{23} 1/mol
n_c	Cycle number
$\dot{q}$	Volumetric heat generation rate, W/m^3
$\dot{Q}$	Instantaneous heat generation rate, W
q''	Heat flux, W/m^2
R	Electrical resistance, Ω
R_u	Universal gas constant, 8.314 J/mol·K

s	Molar entropy, J/mol·K
S_i	Temperature dependent heat flux sensor sensitivity, μV/(W/m^2)
t	Time, s
T	Temperature, K
U_{ocv}	Open circuit voltage, V
V	Volume, m^3
x	Li content of the host material
z	Valency
Z	Electrical impedance, Ω
ΔH_{sol}	Solvation molar enthalpy, kJ/mol
ΔU_{ocv}	Open circuit voltage change between consecutive current pulses, V
ΔV	Voltage difference measured in the heat flux sensor, μV
ΔV_i	Change in cell potential due to current pulses excluding the IR drop, V

Greek symbols

α	Coefficient related to reversible EDL heat generation, W/A
β	Coefficient related to reversible faradaic heat generation, W/A
γ	Coefficient related to irreversible faradauc heat generation, W/A
ε_0	Vacuum permittivity, 8.854×10^{-12} F/m
ε_r	Relative permittivity
ε	Binding energy of Li lattice site, eV
η	Overpotential, V
θ	Ratio of binding energies of Li lattice sites
ν	Scan rate, mV/s
ρ	Density, kg/m^3
σ	Electrical conductivity, S/m
τ	Duration of a current pulse, s
ϕ	Phase angle, rad
ψ	Electric potential, V

$\Delta\psi$	Potential window, V

Superscripts and subscripts

$-$	Refers to anions
$+$	Refers to cations
∞	Refers to bulk
AC	Refers to activated carbon electrode
ct	Refers to charge transfer
dc	Refers to the time-independent DC contribution
EDL	Refers to the capacitive contribution
F	Refers to the faradaic contribution
irr	Refers to irreversible process
Im	Refers to the imaginary component of a complex number
J	Refers to Joule heating
Li	Refers to lithium metal electrode
Li^+	Refers to lithium ions
Li_xMA	Refers to Li_xMA electrode
MA	Refers to intercalation compound
max	Refers to maximum
min	Refers to minimum
MnO_2	Refers to cryptomelane electrode
mt	Refers to mas transfer
P	Refers to pseudocapacitive electrode
rev	Refers to reversible process
Re	Refers to the real component of a complex number
s	Refers to the cell
T	Refers to total

ACKNOWLEDGMENTS

I want to express my gratitude to Prof. Laurent Pilon for his guidance, help, and patience during my doctoral work. His tireless search of truth has taught me to not be satisfied with mediocrity but to always strive for excellence. I am grateful to the late Prof. Ivan Catton who welcomed me into his home and enriched my life with his words of wisdom and experience. I also want to thank Prof. Adrienne Lavine who has taught me the importance of clarity, kindness, and fairness inside and outside of the classroom. Moreover, I would like to thank Prof. Timothy Fisher and Dean Bruce Dunn for serving on my thesis committee. I want to thank my dear friend Prof. Ampol Likitchatchawankun for his encouraging words and for always having my back. Furthermore, I thank Dr. George DeMoulin for teaching me how to persevere and for always being there for me and lending me his ear. In addition, I want to thank my collaborators Yucheng Zhou, Dr. Sun Woong Baek, Camille Douard, Prof. Olivier Crosnier, Prof. Thierry Brousse, Dr. Danielle Butts, Dr. Grace Whang, and Randy Chen. Without them this work would not have been possible. A special thank you goes to my dear friends Leslie Insixiengmay, Mariah Gomez, Sonia Gomez, Ken Mei, Jan Klarič, Mariah Wright, and Andrea Oliva who made my life in Los Angeles amazing. I also want to acknowledge all my lab members. With a heavy heart I remember my dear departed friend Richard Wendel, who was one of the wisest and kindest souls I knew.

My mother and father, Lija and Dušan Frajnkovič, thank you for your unwavering support in failure and relentless encouragement in success.

Last but certainly not least, I want to thank my wife Esther Frajnkovič for always being there for me and believing in me when I did not.

This material is based on the work supported by The Frank Kerže and Therese Kerže-Cheyovich Research Assistanship for the Study of Transport Phenomena in Complex Systems. This material is also based on the work supported by the Center for Synthetic Control Across Length-scales for Advancing Rechargeables (SCALAR), an Energy Frontier Research Center funded by the U.S. Department of Energy, Office of Science, Basic Energy Sciences under Award # DESC0019381.

VITA

2012-2015 B.S. Mechanical engineering, University of Maribor, Slovenia.

2015-2017 M.S. Mechanical engineering, University of Maribor, Slovenia.

PUBLICATIONS

A. Likitchatchawankun, R. H. DeBlock, G.Whang, O. Munteshari, **M. Frajnkovič**, B. S. Dunn, and L. Pilon, 2021, Heat generation in electric double layer capacitors with neat and diluted ionic liquid electrolytes under large potential window between 5 and 80 °C, Journal of Power Sources 488, pp. 229368.

S. W. Baek, K. E. Wyckoff, D. M. Butts, J. Bienz, A. Likitchatchawankun, M. B. Preefer, **M. Frajnkovič**, B. S. Dunn, R. Seshadri, and L. Pilon, 2021, *Operando* calorimetry informs the origin of rapid rate performance in microwave-prepared $TiNb_2O_7$ electrodes, Journal of Power Sources 490, pp. 229537.

S. W. Baek, M. B. Preefer, M. Saber, K. Zhai, **M. Frajnkovič**, Y. Zhou, B. S. Dunn, A. Van der Ven, R. Seshadri, and L. Pilon, 2022, Potentiometric entropy and *operando* calorimetric measurements reveal fast charging mechanisms in PNb_9O_{25}, Journal of Power Sources 520, pp. 230776.

Y. Zhou, E. Le Calvez, S. W. Baek, **M. Frajnkovič**, C. Douard, E. Gautron, O. Crosnier, T. Brousse, and L. Pilon, 2022, Effect of particle size on thermodynamics and lithium ion transport in electrodes made of $Ti_2Nb_2O_9$ microparticles or nanoparticles, Energy Storage Materials 52, pp. 371-385.

M. Frajnkovič, A. Likitchatchawankun, C. Douard, Y. Zhou, S. W. Baek, I. Catton, O. Crosnier, T. Brousse, and L. Pilon, 2022, Calorimetry can detect the early onset of hydrolysis in hybrid supercapacitors with aqueous electrolytes, Journal of Power Sources 548, pp. 232069.

M. Frajnkovič, A. Likitchatchawankun, C. Douard, Y. Zhou, S. W. Baek, I. Catton, O. Crosnier, T. Brousse, and L. Pilon, 2022, Contribution of ion solvation/desolvation to heat generation in hybrid supercapacitors, (Manuscript in preparation).

A. Likitchatchawankun, **M. Frajnkovič**, C. Douard, Y. Zhou, S. W. Baek, I. Catton, O. Crosnier, T. Brousse, and L. Pilon, 2022, Calorimetric characterization of the effect of ions on α-MnO_2 charging mechanisms, (Manuscript in preperation).

M. Frajnkovič, A. Likitchatchawankun, Y. Zhou, I. Catton, and L. Pilon, 2022, Charge and mass transfer resistances cause irreversible heat generation in pseudocapacitive electrodes, (Manuscript in preperation).

M. Frajnkovič, Y. Zhou, D. M. Butts, R. Chen, G. Whang, S. W. Baek, I. Catton, B. S. Dunn, and L. Pilon, 2022, Potentiometric entropic measurements inform the structural evolution of $Li_xNa_{1.5-x}VOPO_4F_{0.5}$ (LNVOPF) during cycling, (Manuscript in preperation).

CHAPTER 1

Introduction

1.1 Electrochemical energy storage systems

Electrochemical capacitors (ECs) have received significant interest as fast charging electrical energy storage systems [5–10] for (i) memory protection in electronic circuitry and portable electronic devices [11], (ii) power quality of smart grids with intermittent renewable sources [11], and (iii) hybrid or all-electric vehicles [11] particularly for regenerative breaking systems [12, 13]. Indeed, compared to batteries, ECs offer large power density while suffering from relatively low energy density [5,14]. Electrochemical capacitors can be divided into (i) electric double layer capacitors (EDLCs) and (ii) hybrid supercapacitors [5, 12]. EDLCs consist of two highly porous carbon electrodes with large specific surface area ($\geq$1,000 m^2/g) [5]. They store energy via ion adsorption at the electrode surface with the formation/dissolution of the electric double layer (EDL) [5]. Such storage mechanism is very fast and highly reversible resulting in large power density, however their energy density is small [5]. On the other hand, hybrid supercapacitors consist of a pseudocapacitive metal oxide electrode and an AC counter electrode. They store charge predominantly through fast surface redox reactions or fast ion intercalation into the pseudocapacitive electrode material without inducing phase transition [5, 12, 15, 16]. Two different charging mechanisms have been proposed for pseudocapacitive electrodes, namely (i) charging through surface or near-surface redox reactions, such as in α-MnO_2 cryptomelane [17–22] and (ii) charging by fast ion intercalation/deintercalation into the channels or layers of the redox-active material without inducing a phase transition, such

as in Nb_2O_5 [16, 23]. In both cases, the reversible redox reaction can be written as [24],

$$[M_xO_y] + zC^+ + ze^- \underset{\text{charging}}{\overset{\text{discharging}}{\rightleftharpoons}} [(C_z^+)M_xO_{y-z}^-]. \tag{1.1}$$

Here, C^+ refers to alkali or alkaline earth metal cations (i.e., Li^+, Na^+, K^+, Cs^+, Mg^{2+}) in the electrolyte. Charging via fast surface redox reactions results in nearly rectangular cyclic voltammograms and almost linear temporal evolution of potential under galvanostatic cycling, similar to those observed in EDLCs [16]. On the other hand, charging via ion intercalation/deintercalation typically results in larger capacity, as the cyclic voltammograms often feature redox peaks. Similarly, the temporal evolution of the cell potential under galvanostatic cycling is typically non-linear [16].

In recent years, batteries established themselves as crucial components in applications where large energy density is required while still providing reasonable power density [16, 25–28]. This includes portable and flexible electronics, grid storage, implantable medical devices and electric vehicles [16, 25–28]. Batteries consist of a cathode and an anode immersed in an electrolyte solution. The cathode is an oxidizing electrode while the anode is the reducing electrode. In other words, during charging the cathode loses electrons while the anode gains electrons. Due to their high energy and power density, long cycle life, and low environmental impact, Li ion batteries (LIBs) and Na ion batteries (NIBs) are ideal candidates for these applications [29]. Metal oxides that can operate above 1 V vs. Li/Li^+ have been proposed as battery cathode materials to avoid solid-electrolyte interphase (SEI) formation and extending their cycle life [30–33].

1.2 EC and battery constituents

1.2.1 Electrodes

Electrodes used in EDLCs are typically made from highly porous carbon such as activated carbon (AC) [34], carbon nanotubes [35, 36], and ordered mesoporous carbon [37]. They are inexpensive, feature high specific surface area and have high electrical conductivity [5]. On

the other hand, pseudocapacitive electrodes are typically made out of transition metal oxides such as MnO_2, MoO_2, Nb_2O_5, V_2O_5, and Fe_3O_4 [38,39]. Moreover, redox active conducting polymers such as polyaniline, polypyrrole, PEDOT,and polythoiphene or their composites with carbon nanotubes can also be used as pseudocapacitive electrodes [40]. An intrinsic disadvantage of these polymers compared to conventional pseudocapacitive electrodes is their relatively low electrical conductivity [40]. This can lead to excessive potential drop across the electrode and lower energy density [40]. Moreover, the electrode thickness must be considered when designing pseudocapacitive electrodes as their resistance increases with increasing thickness. Another way to improve the electrode performance is through the use of a highly electrically conductive scaffold (i.e., carbon nanotubes) on which thin films of pseudocapacitive materials are deposited [41–44].

The cathodes used in the earliest LIBs were made of TiS_2 [45] while the earliest anode material was graphite [46]. Since then, materials such as $LiCoO_2$ have been proposed as prospective cathode materials [47]. The structure of $LiCoO_2$ features similar layered crystal structure as TiS_2. However, $LiCoO_2$ can operate at significantly higher voltage (4 V vs. Li/Li^+) compared to TiS_2 (2 V vs. Li/Li^+) [47]. To date, graphite anodes are still widely used due to their large theoretical capacity and inexpensive fabrication [48]. However, they suffer from solid-electrolyte interphase (SEI) formation due to their low operating potential (0.2 V vs. Li/Li^+) [49] and perform poorly at high C-rates [50]. Therefore, conducting oxides such as $TiNb_2O_7$ have been proposed as alternative high C-rate anode materials that can operate at higher voltage ($\leq$ 1.5 V vs. Li/Li^+) [30,51].

Moreover, binders are used during electrode manufacturing to hold their constituents together and increase the electrode conductivity [52,53]. The most commonly used binders are polyvinyldene fluoride (PVDF), polytetrafluoroethylene (PTFE), and carbomethyl cellulose (CMC) [54–61]. However, binders can introduce functional groups that affect the characteristics of the electrode and caution must be used when choosing them [61]. Furthermore, additives such as carbon black can enhance the electrical conductivity of the electrode [62,63]. Additionally, doping carbon with nitrogen can increase the electrode lifetime and improve its performance at higher voltages [64]. Surfactants such as TBAOH, CTAB, and SDBS can

also be used to increase the wettability of the electrodes [65]. Finally, addition of TiO_2 or $Ba(OH)_2$ can decrease the charge transfer resistance in MnO_2 electrodes by enhancing the electron transport properties of the electrodes [66].

Polymorphs of MnO_2

Crystalline manganese dioxide (MnO_2) is a naturally abundant mineral that is formed by MnO_6 octahedra sharing vertices and edges in various combinations resulting in one, two, or three-dimensional tunnel structures [39, 67, 68]. Their differences may be characterized by the size (n × m) and number of tunnels as well as the geometry of the tunnels (i.e., 1D, 2D, or 3D) in the MnO_2 unit cell [69]. Some MnO_2 polymorphs with small 1D tunnels such as pyrolusite (β-MnO_2) and nsutite (γ-MnO_2) are more likely to exhibit fast surface redox charging mechanism. Then, their capacity is proportional to their surface area, like in EDLCs [39]. By contrast, birnessite (δ-MnO_2) forms a 2D lamellar structure and exhibits larger capacity than β- and γ-MnO_2, due to cation intercalation/deintercalation [39, 70]. In contrast to birnessite, cryptomelane (α-MnO_2) features surface redox reactions despite having relatively large tunnels that could facilitate cation intercalation. This can be attributed to the sieve-like structure of α-MnO_2 tunnels [70]. Interestingly, both charging mechanisms may take place in other MnO_2 polymorphs [39,67,68]. Finally, during cycling of MnO_2 electrodes in mild aqueous electrolytes, Mn changes its oxidation state from Mn^{4+} to Mn^{3+} (with eventually dismutation of Mn^{3+} into Mn^{2+} and Mn^{4+}) when discharged with monovalent or bivalent cations, respectively [39, 67, 68].

1.2.2 Liquid electrolytes

Liquid electrolytes used in ECs and batteries can be split into three groups, namely (i) aqueous electrolytes, (ii) organic electrolytes, and (iii) ionic liquids (ILs). Aqueous electrolytes are limited by the electrochemical stability window of water of 1.23 V at 20 °C and pH of 7 [14,71]. They typically operate with a potential window of 1 V. Moreover, organic electrolytes consist of a salt dissolved in an organic solvent. The most commonly used organic solvents are ace-

tonitrile (AN), propylene carbonate (PC), ethylene carbonate (EC, and dimethyl carbonate (DMC) [14]. Although organic electrolytes offer the benefit of a larger operating potential window (> 2 V [71]), they face several challenges including (i) organic solvents are more expensive than water, (ii) their dielectric constant and electrical conductivity are inferior to those of aqueous electrolytes, and (iii) they are highly flammable and toxic [71]. Finally, ionic liquid electrolytes can operate under a high potential window (> 3 V) as they are not dissolved in any solvent. Similarly, they can operate below 0 °C. They are not flammable, and offer a wide variety of different ion configurations [14,71,72]. However, ILs are expensive and have a lower electrical conductivity than organic electrolytes [14, 71, 72]. In fact, to improve their electrical conductivity, they can be dissolved in organic solvents [73]. Common ILs include N-butyl-n-methylpyrrolidinium bis(trifluoromethanesulfonyl)imide ($PYR_{14}TFSI$) and N-methyl-n-propylpiperidinium bis(fluorosulfonyl)imide ($PIP_{13}FSI$) [74].

1.3 Electrochemical methods

1.3.1 Galvanostatic cycling

Galvanostatic cycling consists of imposing a rectangular constant current $I(t)$ as [75–77]

$$I(t) = \begin{cases} I_{GC} & \text{for } t_0 \leq t \leq t_0 + t_c \\ -I_{GC} & \text{for } t_0 + t_c < t \leq t_0 + t_c + t_d. \end{cases} \tag{1.2}$$

Here, I_{GC} is the imposed constant current, t_0 is the time at the start of the cycle, t_c is the charging time, and t_d is the discharging time. Moreover, the time of one cycle is the sum of charging and discharging times, i.e., $t_{cd} = t_c + t_d$. Then, the potential response $\psi_s(t)$ is measured. Figure 1.1 shows (a) the imposed current $I(t)$ under galvanostatic cycling and (b) the temporal evolution of the cell potential $\psi_s(t)$ as functions of time. The potential response $\psi_s(t)$ of an ideal capacitor is linear. Such behavior is typical for EDLCs and hybrid supercapacitors with fast surface redox reactions [16]. Moreover the potential vs. time curves feature an IR drop when the current switches from I_{GC} to $-I_{GC}$ or vice versa. This drop

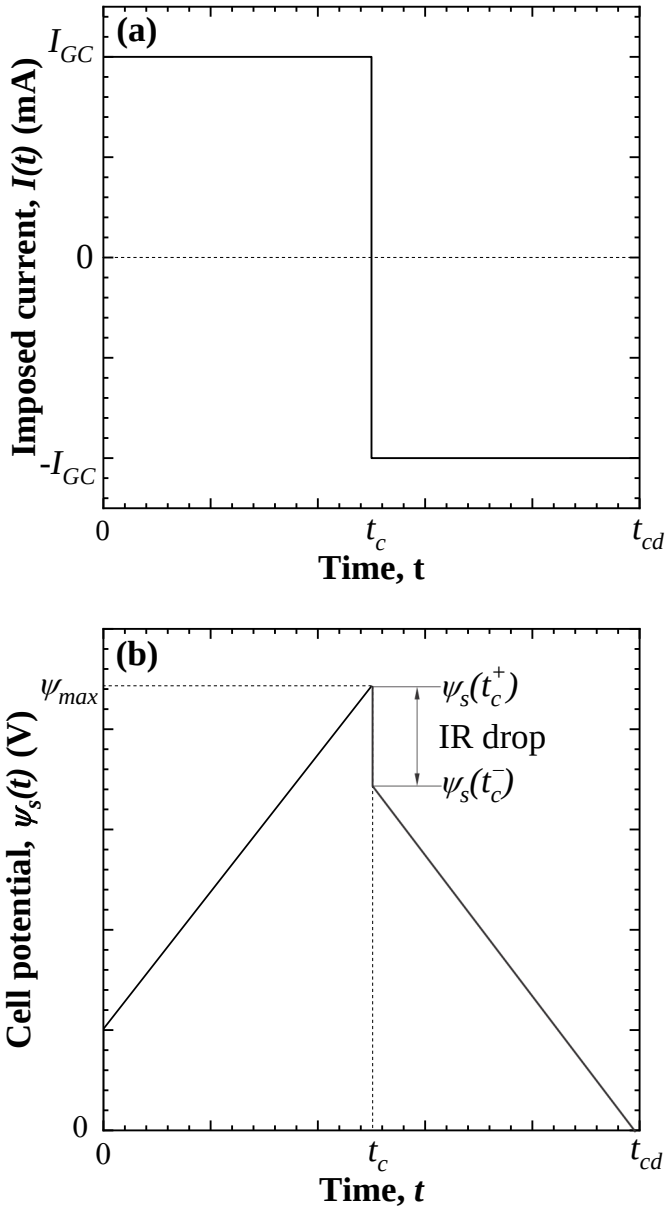

Figure 1.1: (a) The imposed current I and (b) the potential response $\psi_s(t)$ as functions of time under galvanostatic cycling.

can be used to calculate the internal resistance of the device according to [1, 61, 78–80]

$$R_s(I) = \frac{\psi_s(t_c^+) - \psi_s(t_c^-)}{2I_{GC}}. \tag{1.3}$$

Here, $\psi_s(t_c^+)$ and $\psi_s(t_c^-)$ are the cell potentials at the end of the charging step and 10 ms after the beginning of the discharging step, respectively (i.e., $t_c^+ - t_c^- = 10$ ms), as recommended in Ref. [79].

1.3.2 Cyclic voltammetry (CV)

Cyclic voltammetry (CV) is an electrochemical method consisting of imposing a triangular potential $\psi_s(t)$ while measuring the current response $I(\psi_s)$. The imposed potential $\psi_s(t)$ can be expressed as [81]

$$\psi_s(t) = \begin{cases} \psi_{max} - \nu[t - (n_c - 1)t_{CV}] & \text{for } (n_c - 1)t_{CV} \leq t < (n_c - 1/2)t_{CV} \\ \psi_{min} + \nu[t - (n_c - 1/2)t_{CV}] & \text{for } (n_c - 1/2)t_{CV} \leq t < n_c\, t_{CV}. \end{cases} \tag{1.4}$$

Here, ν is the scan rate, n_c is the cycle number, and t_{CV} is the cycle period. Moreover, ψ_{min} and ψ_{max} are the minimum and maximum values of the imposed potential $\psi_s(t)$, respectively. Figure 1.2 shows (a) the imposed potential $\psi_s(t)$, and (b) the resulting cyclic voltammogram plotting $I(t)$ vs. $\psi_s(t)$. For an ideal capacitor, the cyclic voltammogram is rectangular. In practice, cyclic voltammograms feature a leaf-like shape due to diffusion limitations of ions in the electrode and the electrolyte particularly at high scan rate. The differential capacitance $C_{diff}(\psi_s)$ can be plotted like a cyclic voltammogram and calculated as [82]

$$C_{diff}(\psi_s) = I(\psi_s)/\nu. \tag{1.5}$$

Moreover, the integral capacitance can be expressed as

$$C_{int} = \frac{1}{2(\psi_{max} - \psi_{min})} \oint \frac{I(\psi_s)}{\nu} \mathrm{d}\psi_s. \tag{1.6}$$

Please note that for an ideal capacitor C_{diff} and C_{int} are the same and cyclic voltammetry and galvanostatic cycling yield the same results.

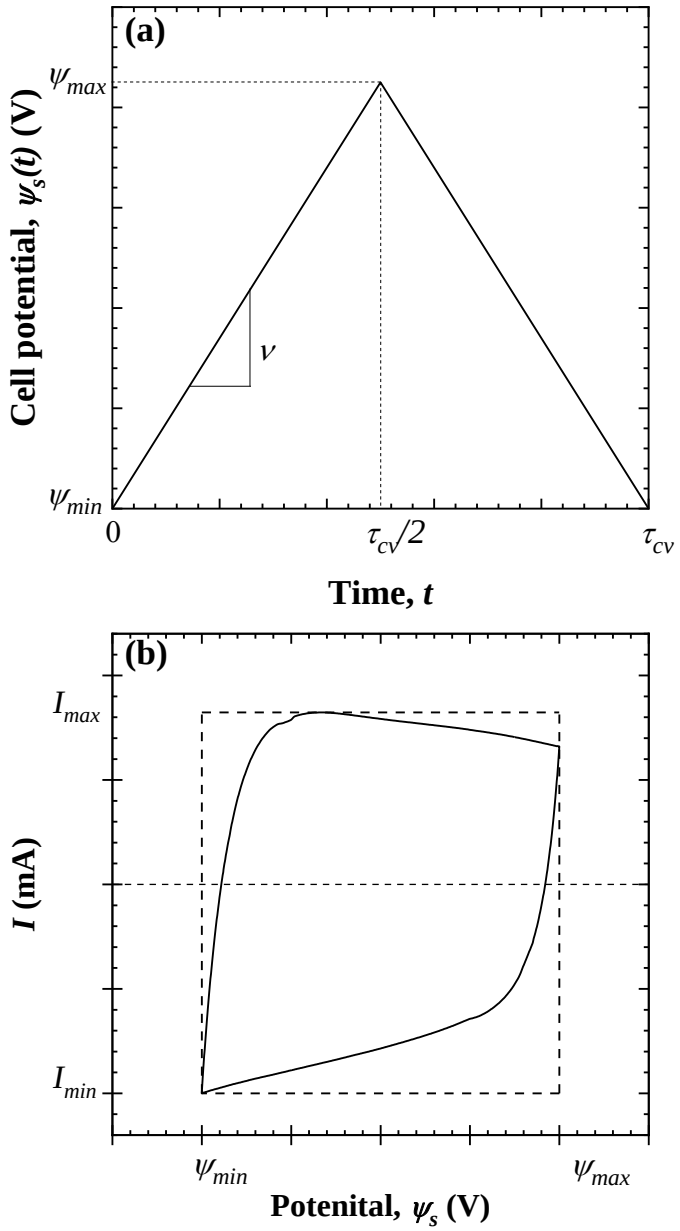

Figure 1.2: (a) The imposed triangular potential $\psi_s(t)$ as a function of time and (b) the cyclic voltammogram for an ideal case (dashed line) and a real case (solid line).

1.3.3 Electrochemical impedance spectroscopy

Electrochemical impedance spectroscopy (EIS) consists of imposing a sinusoidal electric potential with amplitude ψ_0 and frequency f. The sinusoidal potential is superimposed on a time-independent DC offset potential ψ_{dc}. Then, the current response $I(t)$ is mea-

sured [83–85]. The imposed potential $\psi_s(t)$ and the measured current response $I(t)$ can be expressed as [83, 86–88]

$$\psi_s(t) = \psi_{dc} + \psi_0 e^{i2\pi ft} \text{ and } I(t) = I_{dc} + I_0 e^{i[2\pi ft - \phi(f)]}. \tag{1.7}$$

Here, I_{dc} is the DC current, I_0 is the amplitude of the current oscillations, and $\phi(f)$ is the frequency-dependent phase angle between the imposed potential ψ_s(t) and the current response $I(t)$. Figure 1.3 shows (a) the imposed potential $\psi_s(t)$ and (b) the current response $I(t)$ as functions of time for typical EIS measurement. The complex electrochemical impedance $Z(f)$ is defined as [83, 86–88]

$$Z(f) = \frac{\psi_s(t) - \psi_{dc}}{I(t) - I_{dc}} = \frac{\psi_0}{I_0} e^{i\phi} = Z_{re}(f) + iZ_{im}(f), \tag{1.8}$$

where Z_{re} and Z_{im} (in Ωm^2) are the real and imaginary components of the impedance, respectively. Figure 1.4 shows (a) the typical Nyquist plot for an EDLC electrode and (b) the plot of $-Z_{im}$ vs. the inverse of frequency (time) reproduced from Ref. [1]. Several regions in the Nyquist plot can be attributed to the electrical resistances associated with each part of an EC [Figure 1.4(a)] as identified by Mei et. al. [1], namely (i) the electrode resistance, (ii) the electrolyte resistance, and (iii) the diffuse layer resistance [1]. Moreover, the Nyquist plots for pseudocapacitive electrodes can feature another semi-circle at lower frequencies which was attributed to the sum of the charge and mass transfer resistances [89]. Finally, the low frequency data [Figure 1.4(b)] can be used to retrieve the equilibrium differential capacitance C_{eq} [1].

1.3.4 Galvanostatic intermittent titration technique (GITT)

Galvanostatic intermittent titration technique (GITT) consists of imposing a series of current pulses each followed by a relaxation period during which the measured cell potential relaxes towards the open circuit voltage $U_{ocv}(x, T)$ of the cell [90,91]. It can be used to retrieve both the thermodynamic and kinetic parameters of batteries [90, 91]. In particular, the apparent

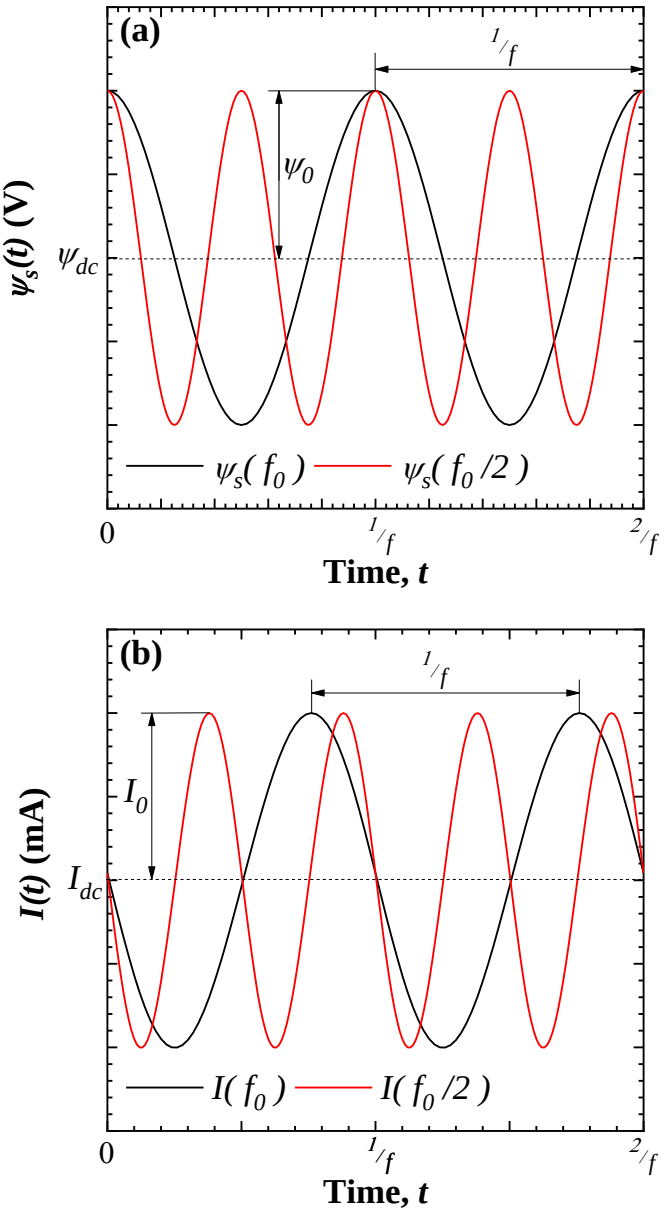

Figure 1.3: (a) The imposed potential $\psi_s(t)$ and (b) the current response $I(t)$ as functions of time under EIS conditions.

diffusion coefficient D_{Li^+} can be calculated from the GITT measurements through Fick's law as [4, 31, 90]

$$D_{Li^+}(x,T) = \frac{4}{\pi\tau}\left(\frac{V}{A}\right)^2\left(\frac{\Delta U_{ocv}(x,T)}{\Delta V_i(x)}\right)^2. \tag{1.9}$$

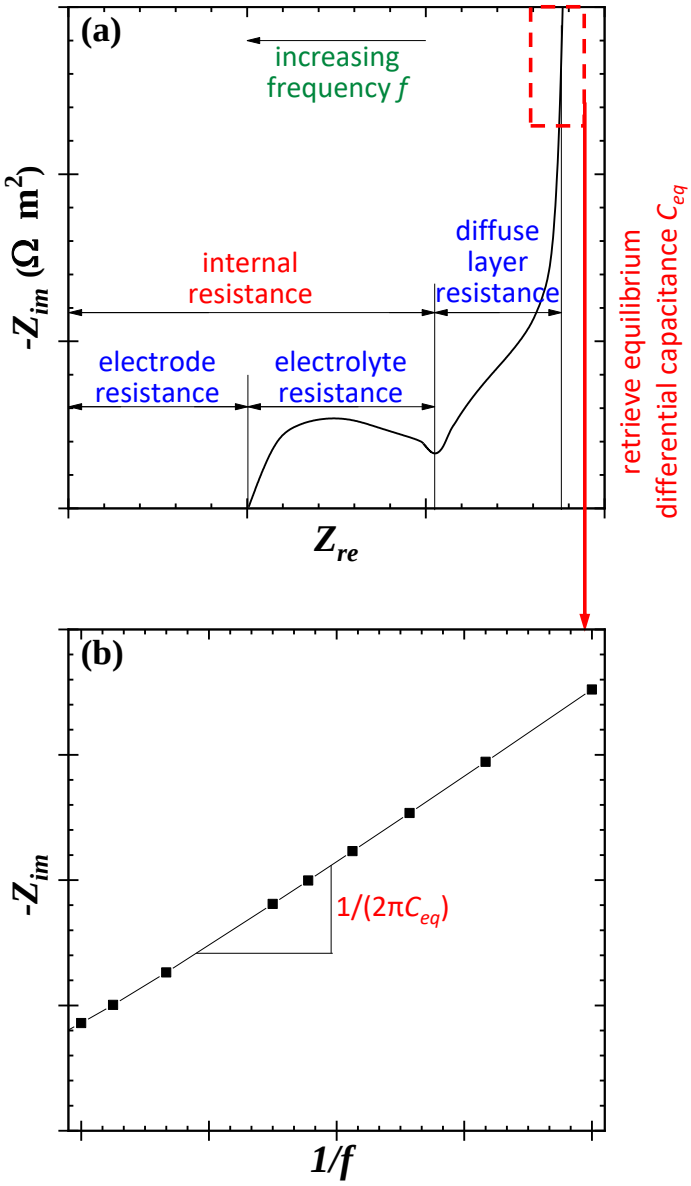

Figure 1.4: (a) The Nyquist plot for an EDLC electrode, and (b) the low frequency data for $-Z_{im}$ vs. $1/f$ used to retrieve the equilibrium differential capacitance C_{eq} reproduced from [1].

Here, τ is the duration of the current pulse in GITT measurement and V and A are the volume and the surface area of the electrode, respectively. Moreover, $\Delta V_i(x)$ is the change of the cell potential during one current pulse, and $\Delta U_{ocv}(x,T)$ is the change of the open circuit voltage between consecutive current pulses. Please note that Equation (1.9) is only valid for small current pulses when V vs. $\sqrt{t}$ behaves linearly [90]. It does not apply when

the material is undergoing phase transition as Li^+ ion transport is not Fickian [92].

1.3.5 Potentiometric entropic potential measurements

Entropic potential offers unique *operando* insight into the physicochemical phenomena occurring in battery electrodes during cycling [31]. Its evolution vs. x can identify processes such as insulator/metal transition [93], phase transformation and two phase coexistence [31, 94], phase transformation with a stable intermediate phase [31], and ion intercalation/deintercalation in solid solution with ion ordering [31, 93–97]. Entropic potential is defined as the change of open circuit voltage $U_{ocv}(x,T)$ with respect to the change in temperature T. The open circuit voltage $U_{ocv}(x,T)$ is a function of the molar Gibbs free energies $g_{Li_xMA}(x,T)$ of the Li_xMA and $g^o_{Li}(x,T)$ of the Li electrodes expressed as

$$U_{ocv}(x,T) = -\frac{1}{e}\left[\frac{\partial g_{Li_xMA}(x,T)}{\partial x} - g^o_{Li}(T)\right]. \tag{1.10}$$

Furthermore, taking the derivative of Equation (1.10) with respect to temperature T yields the entropic potential under isobaric conditions as [31]

$$\frac{\partial U_{ocv}(x,T)}{\partial T} = \frac{1}{e}\left[\frac{\partial}{\partial x}\left(\frac{\partial g_{Li_xMA}(x,T)}{\partial T}\right) - \frac{\partial g^o_{Li}(T)}{\partial T}\right] = \frac{1}{e}\left[\frac{\partial s_{MA}(x,T)}{\partial x} - s^\circ_{Li}(T)\right]. \tag{1.11}$$

Here, $s_{MA}(x,T)$ is the entropy of the intercalation compound working electrode dependent on the Li content x and the temperature T, and $s^0_{Li}(T)$ is the entropy of the Li metal counter electrode and is only dependent on the temperature T. It should be noted that $\partial U_{ocv}(x,T)/\partial T$ is linearly proportional to partial molar entropy $\partial s_{MA}(x,T)/\partial x$ at fixed temperature T as indicated by Eq. (1.11). Although the equation governing $\partial U_{ocv}(x,T)/\partial T$ [Eq. (1.11)] is very complex, it can be measured by slightly modifying the galvanostatic intermittent titration technique (GITT) by imposing temperature variations at the end of the relaxation step [31, 93, 94].

1.4 Isothermal *operando* calorimetry

Dandeville et al. [98] developed an *operando* calorimeter equipped with thermocouples for measuring the instantaneous temperature profile of (i) an EDLC cell consisting of two identical AC electrodes and of (ii) a hybrid supercapacitor cell consisting of a positive amorphous MnO_2 electrode and a negative AC electrode [98]. The two cells were assembled in 0.5 M K_2SO_4 aqueous electrolyte and tested under constant current cycling [98]. The total instantaneous heat generation rate in each device was deconvoluted from the measured temperature changes [98]. In the EDLC cell, the instantaneous heat generation rates at the AC electrode half-cells were assumed to be identical [98]. In addition, the instantaneous heat generation rate at the MnO_2 half-cell was estimated by subtracting that measured in the AC electrode half-cell of the EDLC device from the total heat generation rate measured in the hybrid supercapacitor device [98].

More recently, Munteshari et al. [24, 99] developed an isothermal *operando* calorimeter capable of measuring the instantaneous heat generation rates at each electrode of a hybrid supercapacitor using two thermoelectric heat flux sensors attached to the back of each electrode. In subsequent studies, the isothermal *operando* calorimetry measuring the time-dependent heat generation rates, at each electrode separately, during galvanostatic cycling has been successfully used to identify the thermal signature of different charging mechanisms in EDLCs with aqueous [99], organic [61, 99–101], and ionic liquid [100–102] electrolytes. These mechanisms included (i) ion desolvation and adsorption [61, 100–102], (ii) overscreening effect [61, 100], (iii) organic solvent decomposition [102], and (iv) irreversible ion intercalation in AC electrode under different temperatures and potential windows [102]. Moreover, a new in situ cell was developed for simultaneous thermal analysis (STA) to measure simultaneously heat dissipation and weight changes as well as resistance and capacitance in an EDLC device during cycling or float tests [103]. However, few *operando* calorimetry studies have used calorimetry to investigate hybrid supercapacitors [24, 98].

Finally, a hybrid supercapacitor device consisting of a MnO_2 birnessite nanoparticles synthesized using microwave synthesis and a suspension of graphene (MnO_2-G) as a posi-

tive electrode and a negative AC electrode in 0.5 M Na_2SO_4 aqueous electrolyte has been investigated [24]. Moreover, two hybrid supercapacitor devices consisting of a positive AC electrode and a MoO_2-nanoparticles deposited on reduced graphene oxide (MoO_2-rGO) as a negative electrode in EC:DMC (1:1 vol ratio) solvent with 1 M $LiClO_4$ and in EC:DMC (1:1 wt ratio) solvent with 1 M $TBABF_4$ were also investigated [24]. The devices were subjected to galvanostatic cycling with imposed current I ranging from 2 to 6 mA and potential window $\Delta\psi_s$ between $\psi_{s,min} = 0.4$ V and $\psi_{s,max} = 1.4$ V for the device with a MnO_2-G electrode and $\psi_{s,min} = 0.5$ V and $\psi_{s,max} = 2.5$ V for the device with a MoO_2-rGO electrode. The time-averaged heat generation rate at the AC electrodes was proportional to I^2 and dominated by Joule heating. Similar results were found experimentally for AC electrodes in EDLCs with various electrolytes [61, 98, 99, 104, 105]. Moreover, the time-averaged heat generation rate at the pseudocapacitive electrodes exceeded Joule heating due to irreversible heating associated with faradaic reactions and EDL formation hysteresis at the pseudocapacitive electrode [24]. The reversible heat generation rate at the AC electrodes was exothermic during charging and attributed EDL formation and endothermic during discharging due to EDL dissolution. Indeed, heat is released during the EDL formation and consumed during its dissolution as corroborated by numerical simulations [75]. By contrast, the reversible heat generation rate at the pseudocapacitive MnO_2-G electrode was endothermic during charging and attributed to redox reactions and desorption of cations while it was exothermic during discharging due to the spontaneous fast surface redox reactions accompanied by cations adsorption [24]. Indeed, spontaneous processes are typically exothermic while non-spontaneous processes are endothermic [24]. On the other hand, the reversible heat generation rate at the pseudocapacitive MoO_2-rGO electrode in $LiClO_4$ in EC:DMC was endothermic during charging and attributed to the fast intercalation of small Li^+ cations and exothermic during discharging due to fast deintercalation of cations [24]. Finally, the reversible heat generation rate at the MoO_2-rGO electrode in $TBABF_4$ in EC:DMC was exothermic during charging due to the exothermic EDL formation resulting from the large TBA^+ cations being unable to intercalate into the electrode and endothermic during discharging due to the endothermic EDL dissolution [24]. These results provide a guideline for the interpretation of measured

thermal signatures associated with physical and electrochemical phenomena occurring in hybrid supercapacitors during operation.

1.5 Motivations for the present study

While electrochemical measurements have been widely used to characterize ECs, their interpretation can sometimes be speculative. To complement them, an isothermal *operando* calorimeter was recently developed and has been used to identify the thermal signature of (i) ion desolvation and adsorption [61, 100–102], (ii) the overscreening effect [61, 100], (iii) organic solvent decomposition [102], and (iv) irreversible ion intercalation in AC electrode under different temperatures and potential windows [102]. This calorimeter could be used to identify the onset of hydrolysis in hybrid supercapacitors with aqueous electrolytes, thus determining the maximum operating potential window of the cell for different salts. The heat generation rate at the AC or pseudocapacitive electrode consists of the superposition of heat generation rate due to EDL formation or redox reactions and ion desolvation. It is challenging to distinguish ion desolvation from the other two contributions which tend to dominate the heat generation rate. However, calorimetry may be able to measure the thermal signature of solvation during cycling for salts with sufficiently high enthalpy of solvation. In fact, solvent molecules surrounding the salt must first be partially or fully removed in order for ions to effectively participate in charge storage [106]. Additionally, ion species can affect the charging mechanisms as ions with lower electronegativity do not participate in redox reactions at the electrode surface [24]. By contrast, ions with higher electronegativity could possibly participate in surface redox reactions at the otherwise inert AC electrodes. Such redox reactions are non-spontaneous and the associated thermal signature would be dissimilar to that arising from EDL formation.

Additionally, α-MnO_2 cryptomelane is a naturally abundant good pseudocapacitive material that features fast surface redox reactions. It has been commonly used in combination with AC counter electrodes and aqueous electrolytes. In fact, aqueous electrolytes present the advantage of being inexpensive, environmentally friendly, and can be designed to be

non-corrosive with pH close to 7. However, the operating potential window of such hybrid supercapacitors is limited by the electrochemical stability window of water of 1.23 V at neutral pH and 20 °C.

Previous studies observed that the irreversible heat generation exceeded Joule heating at the pseudocapacitive electrode while it matched Joule heating at the AC electrode [24, 77]. The additional irreversible heat generation was attributed to so-called polarization heating and to concentration profile hysteresis in the pseudocapacitive electrode [24,77]. The polarization heating was attributed to the charge transfer resistance while the mass transfer resistance caused the concentration profile hysteresis [1, 89]. However, models describing the instantaneous heat generation rates caused by charge and mass transfer resistances have not yet been formulated. Indeed, accurately predicting the irreversible heat generation by accounting for all of the irreversible contributions is crucial for the appropriate design of thermal management systems of hybrid supercapacitors.

Conversely, potentiometric entropic potential measurements offer unique *operando* insight into changes occurring in lithium ion battery electrodes under quasiequilibrium lithiation and delithiation [93]. This unique non-invasive and non-destructive technique can be used to identify changes including insulator to semiconductor transition, two phase coexistence region, and solid solution with ion ordering [31,93–97]. In addition to having excellent capacity, LNVOPF can accommodate high currents and at 20C retains 90 % of the capacity at C/2 [33]. In fact, the rate performance of LNVOPF could rival that of hybrid supercapacitors and could establish LNVOPF as the ideal cathode material for applications where high power and energy density is required. The entropic potential evolution could clarify the origin of this excellent capacity retention by elucidating the structural evolution of LNVOPF cathodes.

1.6 Objectives of the present study

This thesis aims to investigate the effect of ion species on the performance and maximum operating potential window of hybrid supercapacitors consisting of a positive α-MnO_2 elec-

trode and a negative AC electrode in various aqueous electrolytes via the use of isothermal *operando* calorimetry. The latter was used to identify the thermal signatures of the onset of hydrolysis and of ion solvation and desolvation during cycling. It was also used to quantify the effect of monovalent cation species on the charging mechanisms as this could affect the capacity of hybrid supercapacitors. By doing so, it expanded the use of calorimetry for determining the maximum operating potential window of hybrid supercapacitors. It also provided scientific insight into the solvation/desolvation processes and charging mechanisms of hybrid supercapacitors.

Furthermore, this thesis aims to formulate and compute, for the first time, the irreversible heat generation rates associated with charge and mass transfer resistances and responsible for previous experimental observations that the total irreversible heat generation exceeds Joule heating at the pseudocapacitive electrodes. Thus, a more accurate understanding of irreversible heat generation and thermal management needs in hybrid supercapacitors was established.

Finally, this thesis aims to use the potentiometric entropic potential measurements to investigate the structural evolution of LNVOPF based cathodes during delithiation and lithiation responsible for their excellent rate performance. It also aim to corroborate the experimental results with a theoretical model of solid solution accounting for ion ordering. By doing so, a more comprehensive insight into the cause of the excellent rate performance of LNVOPF cathodes which could rival the rate performance of hybrid supercapacitors was obtained.

1.7 Organization of the document

Chapter 2 presents experimental *operando* calorimetric measurements of the thermal signature of the onset of hydrolysis in hybrid supercapacitors with α-MnO_2 cryptomelane electrodes in K_2SO_4 and Cs_2SO_4 aqueous electrolytes. Similarly, Chapter 3 investigates the effect of concentration and hydration enthalpy of $MgSO_4$ aqueous electrolytes on the heat generation in hybrid supercapacitors with α-MnO_2 cryptomelane electrodes. Chapter 4 in-

vestigates the effect of ion size on the charging mechanisms of hybrid supercapacitors with α-MnO_2 electrodes using 0.5 M Li_2SO_4, Na_2SO_4, and Cs_2SO_4 aqueous electrolytes. Chapter 5 investigates numerically the causes of irreversible heat generation exceeding Joule heating observed experimentally at the pseudocapacitive electrodes of hybrid supercapacitors. Particular attention was paid to the energy dissipation caused by charge and mass transfer resistances. Chapter 6 elucidates the charging mechanism and the cause of excellent rate performance of LNVOPF by measuring its entropic potential evolution during delithiation and lithiation. Finally, Chapter 7 summarizes the results of individual chapters included in this doctoral thesis and proposes directions and possibilities for future work.

CHAPTER 2

Calorimetry can detect the early onset of hydrolysis in hybrid supercapacitors with aqueous electrolytes

This chapter investigates the effect of cation species on the onset of electrolyte hydrolysis in hybrid supercapacitors with aqueous electrolytes using isothermal *operando* calorimetry. The cells consisted of a positive α-MnO_2 cryptomelane electrode and a negative activated carbon (AC) electrode with either 0.5 M K_2SO_4 or 0.5 M Cs_2SO_4 aqueous electrolytes. They were characterized using cyclic voltammetry and galvanostatic cycling. In addition, the instantaneous heat generation rate at each electrode was measured using a custom isothermal *operando* calorimeter. Heat generation associated with resistive losses (Joule heating) and reversible ion adsorption/desorption was clearly identified. For larger potential windows, an endothermic dip, attributed to the onset of hydrolysis, was observed at the positive α-MnO_2 electrode where K^+ and Cs^+ ions engaged in fast surface redox reactions. Interestingly, this endothermic dip appeared at 1.8 V and 2.0 V for K_2SO_4 and Cs_2SO_4 aqueous electrolytes, respectively. The difference in the stable operating potential window was attributed to thinner solvation shell around Cs^+ cation than for K^+ thus reducing the amount of water present near the electrodes as ions partially shed their solvation shells during adsorption. The early onset of hydrolysis could be observed by isothermal *operando* calorimetry before it could be observed with conventional electrochemical methods.

2.1 Background

2.1.1 Thermal signature of electrolyte decomposition

During cyclic voltammetry of hybrid supercapacitors, water electrolysis is endothermic and may be accompanied by a significant increase in electrical current [107]. Munteshari et al. [102] investigated two EDLC devices under a large potential window $\Delta\psi_s$ up to 4 V. The devices consisted of two AC electrodes in neat ionic liquid $Pyr_{14}TFSI$ (Device 1) or 1 M $Pyr_{14}TFSI$ diluted in PC (Device 2) [102]. Here, a rapid increase in current was observed near the end of the charging step in CV measurements for Device 2 and for the cell potential windows above 3.0 V. It was associated with PC decomposition. In fact, an endothermic dip was observed in the instantaneous heat generation rates measured at the negative electrode and was associated with PC decomposition [102]. Device 1 did not exhibit such behavior due to the absence of PC solvent in the neat ionic liquid [102]. Moreover, the electrochemical stability window of solvents decreased with increasing temperature as the contribution of thermal potential became non-negligible [108]. This has been widely used in hydrogen production where the required power input significantly decreases due to the contribution of heat to the overall energy required for electrolysis [108].

Moreover, previous calorimetric studies investigated the instantaneous heat generation rates in hybrid supercapacitor devices consisting of a positive MnO_2-based amorphous or birnessite electrode and a negative AC electrode with either 0.5 M K_2SO_4 [98] or 0.5 M Na_2SO_4 [24] aqueous electrolyte under galvanostatic cycling. However, the operating potential window of 1.0 V was too small to observe electrolysis.

2.1.2 Onset of hydrolysis

Hong et al. [107] investigated the influence of pH on the potential window limitations of aqueous electrolyte for amorphous MnO_2/AC electrodes in 1 M HCl (acidic), 1 M KOH (basic), and 1 M KCl (neutral) aqueous electrolytes. In a three-electrode setup with a Pt metal plate as the reference electrode, the authors observed that in acidic pH, the following

H_2 evolution reaction began at the AC electrode at -0.2 V when the potential at the MnO_2 electrode was 1.0 V both vs. the Pt reference electrode,

$$2\,H_3O^+ + 2\,e^- \longrightarrow H_2(g) + 2\,H_2O. \tag{2.1}$$

This reaction limited the operating potential window to 1.2 V (< 1.23 V) in 1 M HCl aqueous electrolyte [107]. Similarly in basic pH, the following O_2 evolution reaction started at the MnO_2 electrode at 0.7 V when the potential at the AC electrode was -1.1 V both vs. the Pt reference electrode,

$$4\,OH^- \longrightarrow O_2(g) + 2\,H_2O + 4\,e^- \tag{2.2}$$

Here, the potential window was limited to 1.8 V in 1 M KOH aqueous electrolyte [107]. Moreover, in neutral pH, the H_2 and O_2 evolution reactions were negligible and the following H_2O decomposition reactions were observed for potential window of 2.0 V such that the MnO_2 electrode was at 1.1 V and the AC electrode at -0.9 V both vs. the Pt reference electrode [107],

$$2\,H_2O \longrightarrow O_2(g) + 4\,H^+ + 4\,e^-, \tag{2.3}$$

$$2\,H_2O + 2\,e^- \longrightarrow H_2(g) + 2\,OH^-. \tag{2.4}$$

Overall, in amorphous MnO_2/AC systems with aqueous electrolytes, hydrolysis was delayed in basic and neutral electrolytes with cell potential window exceeding 1.23 V while acidic environment acted as a catalyst for hydrolysis and reduced the maximum cell potential window [107].

2.2 Materials and methods

2.2.1 Electrode fabrication and device assembly

In order to fabricate the α-MnO_2 pseudocapacitive electrodes and the AC electrodes necessary for our study, two different slurries were prepared by mixing the active materials with carbon black (Superior Graphite, > 99%) into polyvinylidene fluoride (PVDF, Solef® 5130) binder solution in a 70:15:15 weight ratio. The active materials were cryptomelane α-MnO_2 (Prince Erachem) and activated carbon (YP-50F, Kuraray Chemical). The PVDF solution was prepared by dissolving PVDF powder in liquid dimethylacetamide (DMA) in an 8.5:91.5 weight ratio. Dry matter contents of the active materials were respectively adjusted at 25.3 wt.% and 18.7 wt.% for α-MnO_2 and AC slurries by adding DMA in order to obtain homogeneous mixtures after vigorous stirring overnight with a magnetic stirrer.

The slurries were drop cast onto titanium (Ti) mesh current collector sheets (Dexmet Corp.) with a 1 × 1 cm^2 footprint area and spread evenly with a spatula. The Ti mesh had been previously treated in a boiling aqueous solution containing 10 wt.% of oxalic acid for at least 30 minutes and rinsed off with DI water in order to enhance the adhesion between the slurry and the mesh current collector. The electrodes were dried in an oven at 60 °C for 12 h. Then, all the electrodes were hot-roll calendared to ensure that the thickness was uniform over the entire electrode and ranged between 36 and 51 μm for α-MnO_2 electrodes and between 82 and 96 μm for AC electrodes [109]. This resulted in a mass loading of 5 - 7 mg/cm^2 for both types of electrodes.

Finally, the devices were assembled with a positive α-MnO_2 electrode and a negative AC electrode separated by a 1 mm-thick, chemically inert, polypropylene mesh separator. The separator was impregnated with either 0.5 M K_2SO_4 (Device 1) or 0.5 M Cs_2SO_4 (Device 2) aqueous electrolytes. These electrolytes were chosen for their significantly different solvation shell thickness [110, 111], relatively small ion hydration molar enthalpy to ensure that ion hydration does not dominate heat generation, and sufficiently large solubility in water (> 0.5 M) to achieve good capacity. Table 2.1 summarizes the electrode and electrolyte properties including parameters used in the interpretation of the results including the active mass load-

ing of the electrodes m_{MnO_2} and m_{AC}, the unsolvated $a_{+/-}$ and solvated $a_{+/-,s}$ ion diameters, their diffusion coefficients $D_{+/-}$, and the ion hydration molar enthalpies $\Delta H_{sol,+/-}$.

2.2.2 Electrochemical characterization

First, the positive α-MnO_2 and the negative AC working electrodes were tested separately in a three electrode setup using elemental Ni as the counter electrode and Ag^+/AgCl as the reference electrode (Fisherbrand^{TM} accumet^{TM}). Each working electrode was subjected to cyclic voltammetry (CV) at scan rate ν = 10 mV/s for 95 cycles and then at scan rate ν = 5 mV/s for the last 5 cycles, with potential window ranging between ψ_{min} = − 0.8 V and ψ_{max} = 0 V for the AC electrode and ψ_{min} = 0 V and ψ_{max} = 0.8 V for the α-MnO_2 electrode. The measured cyclic voltammograms were then used to determine the capacity of each electrode in K_2SO_4 and Cs_2SO_4 aqueous electrolytes so as to pair the α-MnO_2 and AC electrodes with matched capacity in a hybrid device. Here, as argued in Ref. [112], the capacity (in mAh) was chosen in favor of capacitance (in F) as surface redox reactions are the predominant charge storage mechanism [39]. The capacity $C(\nu)$ (in C) as a function of scan rate ν was defined as [82],

$$C(\nu) = \oint \frac{I(\psi_s)}{2\nu} \mathrm{d}\psi_s. \tag{2.5}$$

Here, $I(\psi_s)$ is the measured current response at the triangular cell potential $\psi_s(t)$. The capacity $C(\nu)$ in mAh can be converted to Coulomb (C) by multiplying it by a factor 3.6.

Second, CV measurements were performed on the assembled devices inside the calorimetric cell for 30 cycles at five different scan rates ν ranging from 5 to 50 mV/s at 20 °C. Here, the potential window $\Delta\psi_s$ ranged between $\psi_{s,min}$ = 0 V, and $\psi_{s,max}$ = 1.6 V. The gravimetric capacity $C_g(\nu)$ (in mAh/g) of the devices was also computed according to

$$C_g(\nu) = \frac{C(\nu)}{m} \tag{2.6}$$

where m (in g) is the mass loading of active material in both α-MnO_2 and AC electrodes

reported in Table 2.1.

Furthermore, galvanostatic cycling combined with isothermal calorimetric measurements were performed on the devices at constant current I equal to 5 mA and 6 mA. Here, the cell potential window $\Delta\psi_s$ was first set to 1.2 V to ensure that no hydrolysis occurred. It was then gradually increased to 1.6 V, 1.8 V, and up to 2.0 V until hydrolysis was observed. For each imposed current I, thirty consecutive cycles were performed to ensure that an oscillatory steady-state in the measured heat generation rates had been reached.

Finally, the internal resistance of the device R_s was computed from the IR drop observed at the transition between the charging and discharging steps during galvanostatic cycling according to [1, 78–80],

$$R_s(I) = \frac{\psi_s(t_c^+) - \psi_s(t_c^-)}{2I}. \tag{2.7}$$

Here, $\psi_s(t_c^+)$ and $\psi_s(t_c^-)$ were the cell potentials at the end of the charging step and 10 ms after the beginning of the discharging step, respectively (i.e., $t_c^+ - t_c^- = 10$ ms), as recommended in Ref. [79].

2.2.3 Isothermal *operando* calorimeter

The instantaneous heat generation rate at each electrode in Devices 1 and 2 was measured during galvanostatic cycling for current $I = 5$ and 6 mA and potential window $\Delta\psi_s = 1.2$, 1.6, 1.8 V, and up to 2.0 V. The instantaneous heat generation rate $\dot{Q}_i(t)$ (in mW) at electrode i ($i = \alpha$-MnO_2 or AC) was obtained from the heat flux $q_i''(t)$ measured by the thermoelectric heat flux sensor in thermal contact with the electrode according to [99],

$$\dot{Q}_i = q_i''(t) A_i = \frac{\Delta V_i(t)}{S_i} A_i. \tag{2.8}$$

Here, A_i denotes the footprint area of the electrode ($A_i = 1$ cm^2), ΔV_i is the instantaneous voltage difference measured at each heat flux sensor in thermal contact with electrode i while S_i is the temperature-dependent sensitivity (in μV/(W/m^2)) provided by the manufacturer.

Finally, in an effort to reduce the noise in the measurements, the instantaneous heat

Table 2.1: Electrode and electrolyte properties of the hybrid supercapacitors investigated.

Property/parameter	**Device 1**	**Device 2**
Electrolyte (0.5 M in DI water)	K_2SO_4	Cs_2SO_4
Active mass loading of α-MnO_2, m_{MnO_2} (mg)	6.09	5.53
Active mass loading of AC, m_{AC} (mg)	5.99	5.33
Electrolyte pH	6.69	6.55
Cation diameter, a_+ (nm) [110]	0.276	0.334
Solvated cation diameter, $a_{+,s}$ (nm) [111]	0.315	0.346
Anion diameter, a_- (nm) [113]	0.484	0.484
Solvated anion diameter, $a_{-,s}$ (nm) [113]	1.173	1.173
Cation diffusion coefficient, D_+ (m^2/s) [114]	2.135×10^{-9}	2.076×10^{-9}
Anion diffusion coefficient, D_- (m^2/s) [115]	0.809×10^{-9}	0.809×10^{-9}
Cation hydration molar enthalpy, $\Delta H_{sol,+}$ (kJ/mol) [116]	-322	-264
Anion hydration molar enthalpy, $\Delta H_{sol,-}$ (kJ/mol) [116]	-1059	-1059
Device internal resistance, R_s (Ω)	10.89 $\pm$ 0.02	9.96 $\pm$ 0.65

generation rate at electrode i was averaged over the last five cycles of the 30 cycles as

$$\dot{Q}_i(t) = \frac{1}{5}\sum_{j=26}^{30} \dot{Q}_i(t + (j-1)t_{cd}), \tag{2.9}$$

where t_{cd} is the period of one cycle and j is the cycle number (j = 26 to 30).

2.3 Results and discussion

2.3.1 Cyclic voltametry

2.3.1.1 Three-electrode setup

Figure 2.1 shows the measured cyclic voltammograms for the positive α-MnO_2 and the negative AC electrodes vs. Ag^+/AgCl reference electrode in (a) 0.5 M K_2SO_4 and (b) 0.5 M Cs_2SO_4 aqueous electrolytes at scan rate $\nu = 10$ mV/s. These CV curves were used to compute the capacity $C(\nu)$ of each electrode according to Equation (2.5). The AC electrodes had similar mass loading (Table 2.1) and exhibited similar behavior in the two different electrolytes. Their capacity was about 0.11 mAh. Moreover, the α-MnO_2 electrodes exhibited an oxidation peak at the end of the positive sweep at $\psi_s \simeq 0.8$ V vs. Ag^+/AgCl in all electrolytes. A reduction dip at the start of the negative sweep was also observed at $\psi_s \simeq 0.6$ V vs. Ag^+/AgCl. The positive and negative electrodes were paired so that their capacity was similar in each device. Note that no gas (H_2 or O_2) evolution or bubble formation was visible at either electrode during cycling.

2.3.1.2 Full device setup

Figure 2.2 shows the measured cyclic voltammograms for (a) Device 1 with 0.5 M K_2SO_4 and (b) Device 2 with 0.5 M Cs_2SO_4 aqueous electrolytes for scan rate ν varying from 5 to 50 mV/s. The cell potential $\psi_s(t)$ was measured at the positive α-MnO_2 electrode with respect to the negative AC electrode. The CV curves for both devices changed from a rectangular shape at low scan rates to a leaf-like shape at higher scan rates, indicative of resistive behavior. Moreover, although the cell potential window of $\Delta\psi_s = 1.6$ V exceeded the theoretical electrochemical stability window of 1.23 V for water in both devices, no evidence of hydrolysis could be observed in the CV curves [117, 118].

Moreover, Figure 2.3 shows (a) the capacity $C(\nu)$ and (b) the gravimetric capacity $C_g(\nu)$ per unit mass of both electrodes as functions of scan rate ν for Devices 1 and 2. For both devices, the capacity $C(\nu)$ and the gravimetric capacity $C_g(\nu)$ decreased with increasing

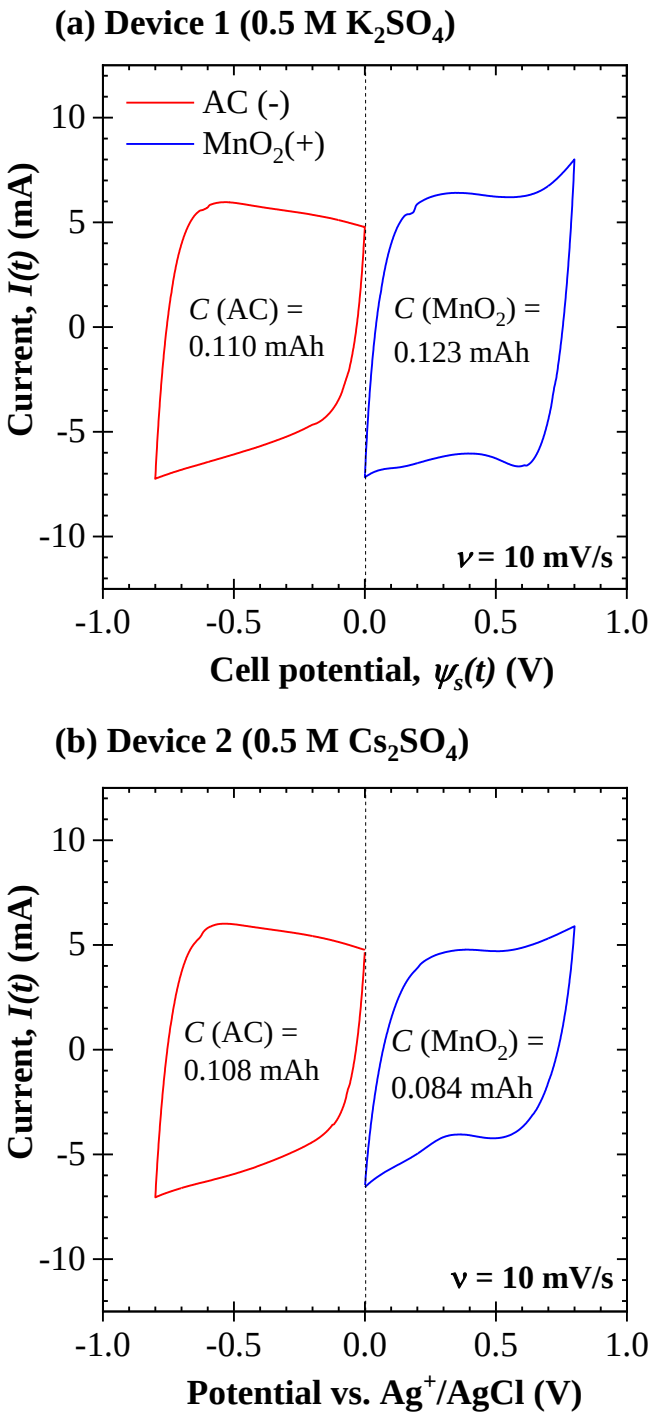

Figure 2.1: Cyclic voltammograms for individual AC and cryptomelane α-MnO_2 electrodes vs. Ag^+/AgCl reference electrode in (a) 0.5 M K_2SO_4 and (b) 0.5 M Cs_2SO_4 aqueous electrolytes at scan rate $\nu = 10$ mV/s.

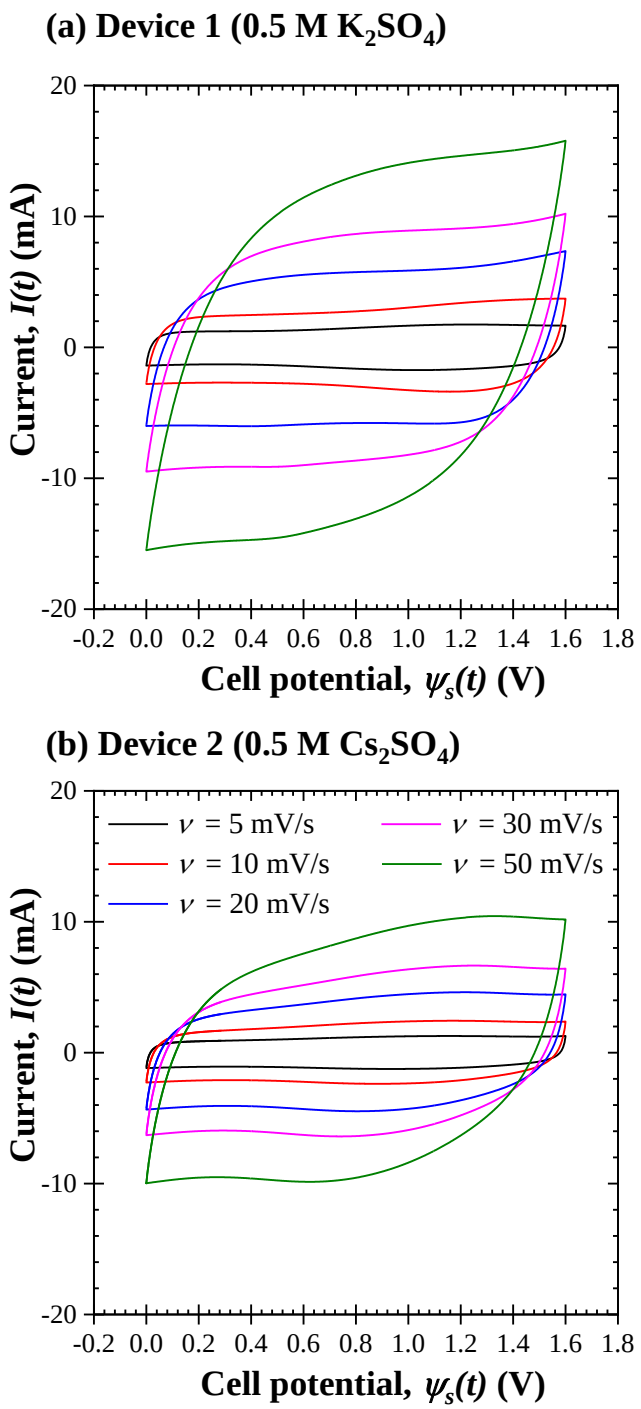

Figure 2.2: Cyclic voltammograms as functions of scan rate $\nu = 5$ to 50 mV/s for (a) Device 1 with 0.5 M K_2SO_4 and (b) Device 2 with 0.5 M Cs_2SO_4 aqueous electrolytes.

scan rate. This can be attributed to ion diffusion limitations and the slow surface redox reactions, as observed in previous experimental studies [24, 119–121]. Similar trends and

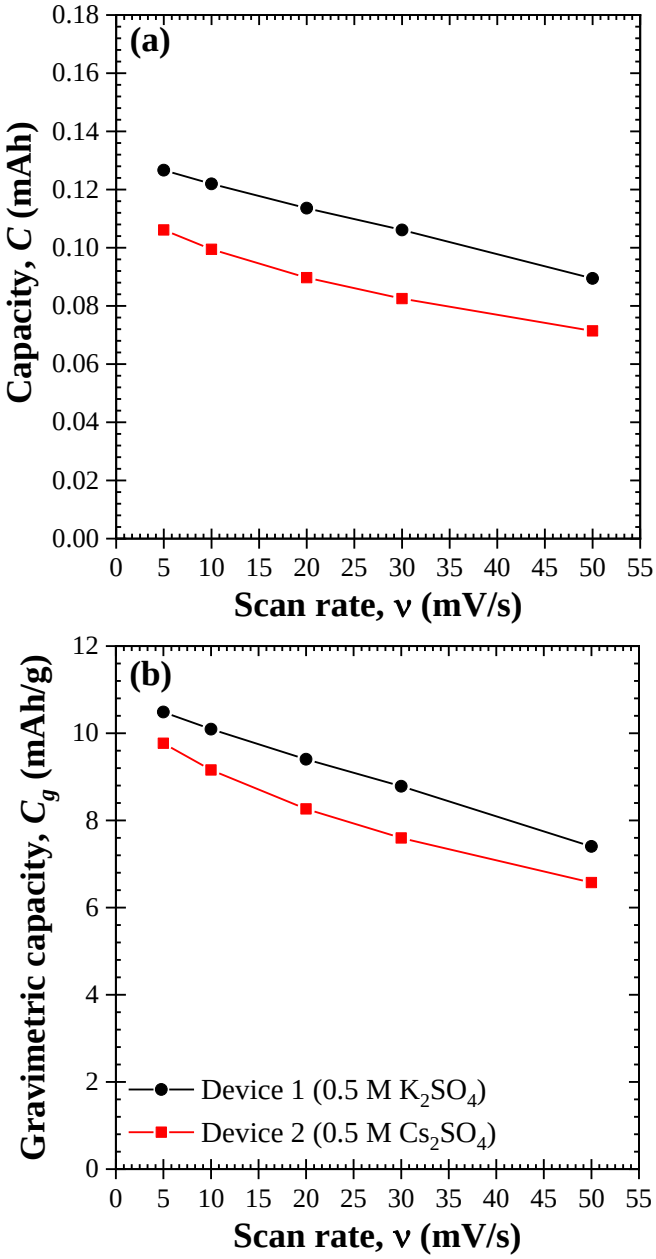

Figure 2.3: (a) Capacity $C(\nu)$ and (b) gravimetric capacity $C_g(\nu)$ per unit mass of both electrodes as functions of scan rate ν for Device 1 with 0.5 M K_2SO_4 and Device 2 with 0.5 M Cs_2SO_4 aqueous electrolytes.

values of gravimetric capacity $C_g(\nu)$ as a function of scan rate ν were also reported by Boisset et al. [70]. Rate capability and capacity retention of electrodes made of MnO_2 nanoparticles were reported in Ref. [119]. Furthermore, the gravimetric capacity $C_g(\nu)$ was larger for Device 1 (0.5 M K_2SO_4) than for Device 2 (0.5 M Cs_2SO_4). This can be attributed

to the larger mass loading of both electrodes in Device 1 (0.5 M K_2SO_4) than in Device 2 (0.5 M Cs_2SO_4). This resulted in more active material (i.e., α-MnO_2 or AC) in the electrode and larger surface area available for surface redox or EDL formation.

2.3.2 Galvanostatic cycling

Figure 2.4 shows the temporal evolution of the cell potential $\psi_s(t)$ under galvanostatic cycling for two different currents $I = 5$ or 6 mA and different potential windows varying (a, b) from $\Delta\psi_s = 1.2$ to 1.8 V for Device 1 and (c, d) from $\Delta\psi_s = 1.2$ to 2.0 V for Device 2. For both devices, the cell potential $\psi_s(t)$ varied almost linearly with time t except at the beginning of the charging or discharging steps featuring an IR drop. A similar behavior can be observed in many EDLCs and hybrid supercapacitors with surface redox reactions [16, 76, 101, 102]. Here also, no electrolyte decomposition was evident in the measured cell potential $\psi_s(t)$ as the cycle period t_{cd} monotonically decreased with increasing current I. Interestingly, the galvanostatic cycle period t_{cd} was shorter for Device 2 than for Device 1, as corroborated by its smaller capacity (Figure 2.3). In addition, the internal resistance R_s of each device, computed according to Equation (2.7), was independent of the imposed current I and equal to $R_s = 10.89 \pm 0.02\ \Omega$ for Device 1 and $R_s = 9.96 \pm 0.65\ \Omega$ for Device 2 (see Table 2.1). Note that the slightly larger resistance of Device 1 compared to Device 2 was due to the slightly larger mass loading of both its electrodes whereas the diffusion coefficients of K^+ and Cs^+ cations in water were similar (Table 2.1).

2.3.3 Instantaneous heat generation rate measurements

2.3.3.1 Negative AC electrode

Figure 2.5 shows the instantaneous heat generation rate $\dot{Q}_{AC}(t)$ averaged over 5 consecutive cycles [Equation (2.9)] at the negative AC electrode in (a, b) Device 1 in 0.5 M K_2SO_4 aqueous electrolyte for potential window $\Delta\psi_s$ of 1.2 V, 1.6 V, and 1.8 V and in (c, d) Device 2 in 0.5 M Cs_2SO_4 aqueous electrolyte for potential window $\Delta\psi_s = 1.2$ V, 1.6 V, 1.8 V, and 2.0 V for imposed current I equal to (a, c) 5 mA and (b, d) 6 mA, respectively. First, the instantaneous

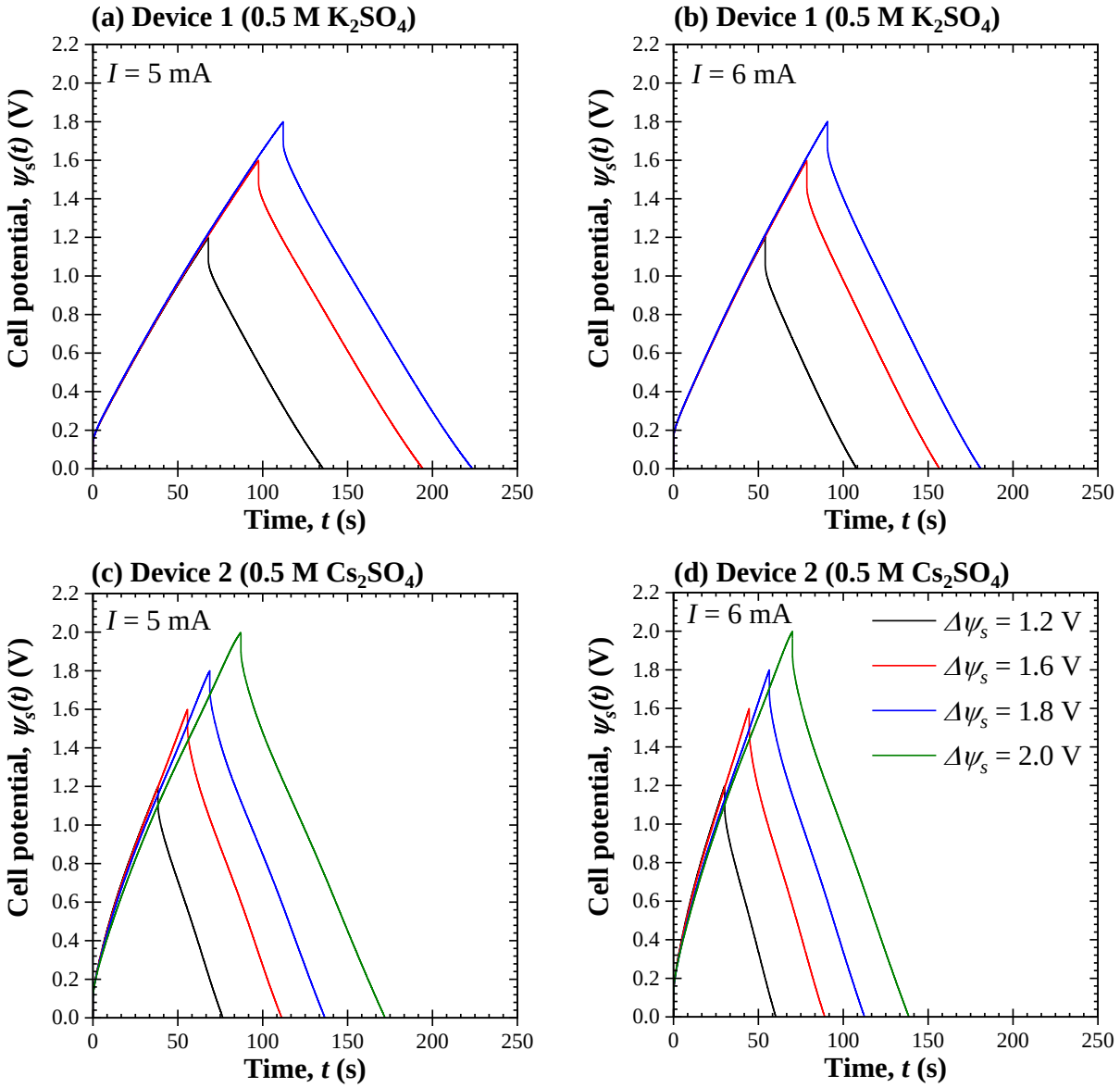

Figure 2.4: Temporal evolution of the cell potential $\psi_s(t)$ during galvanostatic cycling with constant current I of 5 mA and 6 mA (a, b) for Device 1 with 0.5 M K_2SO_4 and (c, d) for Device 2 with 0.5 M Cs_2SO_4 aqueous electrolytes and for potential windows $\Delta\psi_s$ ranging from 1.2 V to 2.0 V.

heat generation rate at each electrode and its thermal signatures were repeatable from cycle to cycle in both devices. Then, the heat generation rates exhibited the same features for both currents and both electrolytes. A slight increase in the heat generation rate $\dot{Q}_{AC}(t)$ was observed at the AC electrode with increasing current I due to increasing resistive losses accompanied by Joule heating. A slight endothermic dip was also observed at the AC

electrode at the beginning of the charging step. It can be attributed to the endothermic desorption and solvation of SO_4^{2-} anions, as previously observed [24, 104]. As the charging progressed, the heat generation rate increased due to desolvation and exothermic adsorption of K^+ (Device 1) and Cs^+ (Device 2) ions in the porous AC electrode [24,104]. Furthermore, an endothermic dip was observed at the beginning of the discharging step attributed this time to the endothermic desorption and solvation of K^+ and Cs^+ cations upon reversal of the current. As the discharging step progressed, desolvation and exothermic adsorption of SO_4^{2-} anions dominated for the remainder of the discharging step.

2.3.3.2 Positive α-MnO_2 electrode

Figures 2.6 shows the instantaneous heat generation rate $\dot{Q}_{MnO_2}(t)$ measured at the positive α-MnO_2 electrode in (a, b) Device 1 in 0.5 M K_2SO_4 aqueous electrolyte for $\Delta\psi_s$ equal to 1.2 V, 1.6 V, and 1.8 V and in (c, d) Device 2 in 0.5 M Cs_2SO_4 aqueous electrolyte for $\Delta\psi_s$ equal to 1.2 V, 1.6 V, 1.8 V, and 2.0 V and imposed current I equal to (a, c) 5 mA and (b, d) 6 mA, respectively. Here also, the instantaneous heat generation rate at each electrode and its thermal signatures were repeatable from cycle to cycle for both devices. Furthermore, the heat generation rate $\dot{Q}_{MnO_2}(t)$ exhibited the same behavior in for both currents and both electrolytes. First, $\dot{Q}_{MnO_2}(t)$ increased in magnitude with increasing current I due to the associated increase in Joule heating. In addition, at the beginning of the charging step, an endothermic dip was observed and attributed to endothermic desorption and solvation of K^+ (Device 1) or Cs^+ (Device 2), based on similar findings by Munteshari et al. [24]. As the charging progressed, exothermic SO_4^{2-} adsorption and desolvation began to dominate resulting in the slow rise observed in $\dot{Q}_{MnO_2}(t)$ [24].

Interestingly, in Device 1 for potential window $\Delta\psi_s$ of 1.6 V and 1.8 V and in Device 2 for $\Delta\psi_s$ of 2.0 V a distinct endothermic dip began to appear at the end of charging for both currents considered. This dip observed at the positive electrode could be attributed to hydrolysis reaction for several reasons, namely (i) hydrolysis is an endothermic process [122,123], (ii) it appeared only at large potentials, (iii) it appeared at the positive electrode as

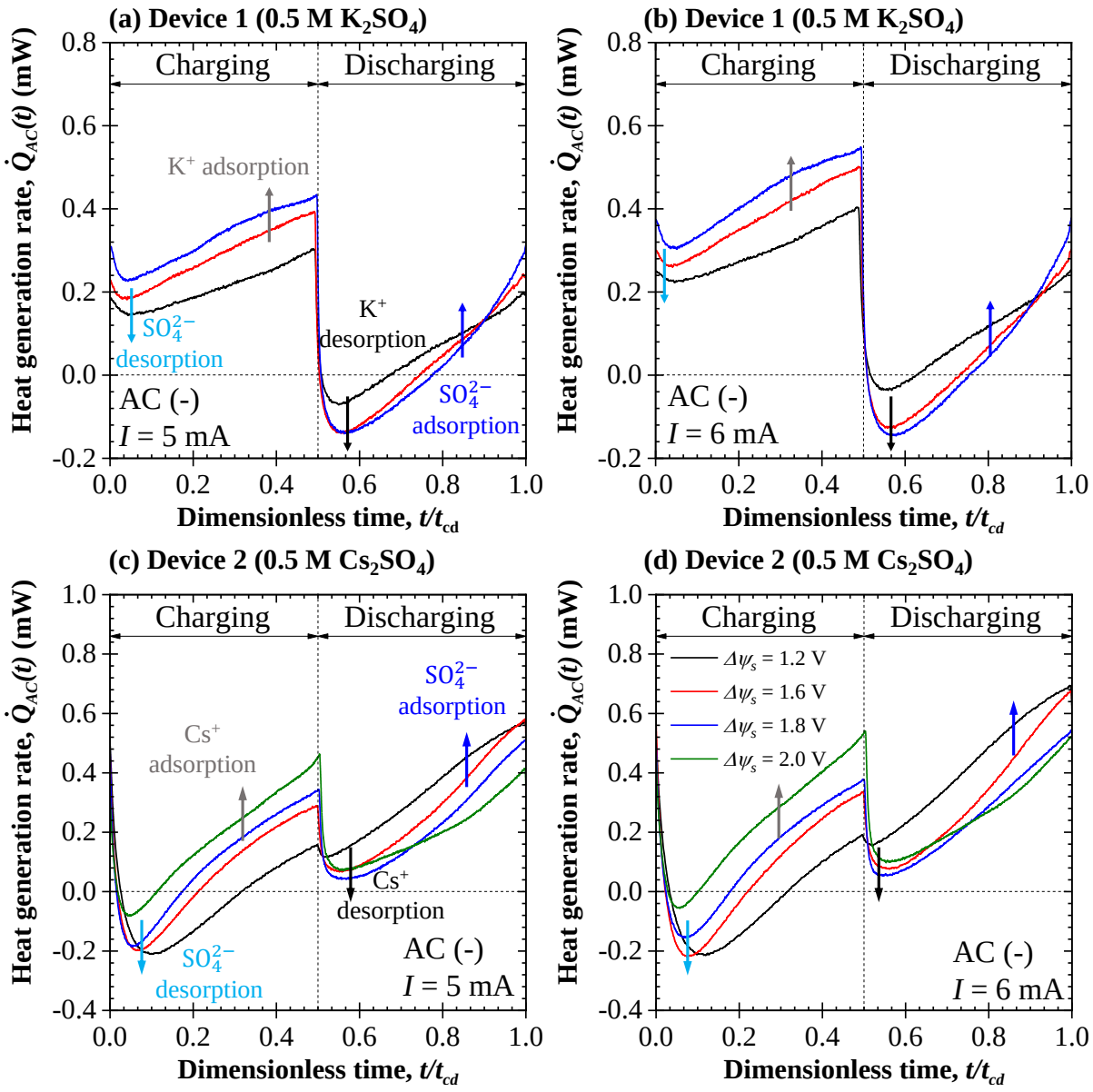

Figure 2.5: Instantaneous heat generation rate at the AC electrodes (a, b) for Device 1 in 0.5 M K_2SO_4 aqueous electrolyte for potential windows $\Delta\psi_s$ = 1.2, 1.6, and 1.8 V and (c, d) for Device 2 in 0.5 M Cs_2SO_4 aqueous electrolyte for potential windows $\Delta\psi_s$ = 1.2, 1.6, 1.8, and 2.0 V as a function of dimensionless time t/t_{cd} with decreased white noise for AC electrode subjected to imposed current of (a, c) I = 5 mA and (b, d) I = 6 mA.

the electrolyte pH was slightly basic (Table 2.1), and (iv) a similar dip was observed in EDLCs and attributed to PC decomposition at potential windows above 3 V. Interestingly, the thermal signature of the onset of hydrolysis could only be observed via *operando* calorimetric measurements at the positive electrode while it was not apparent in any electrochemical

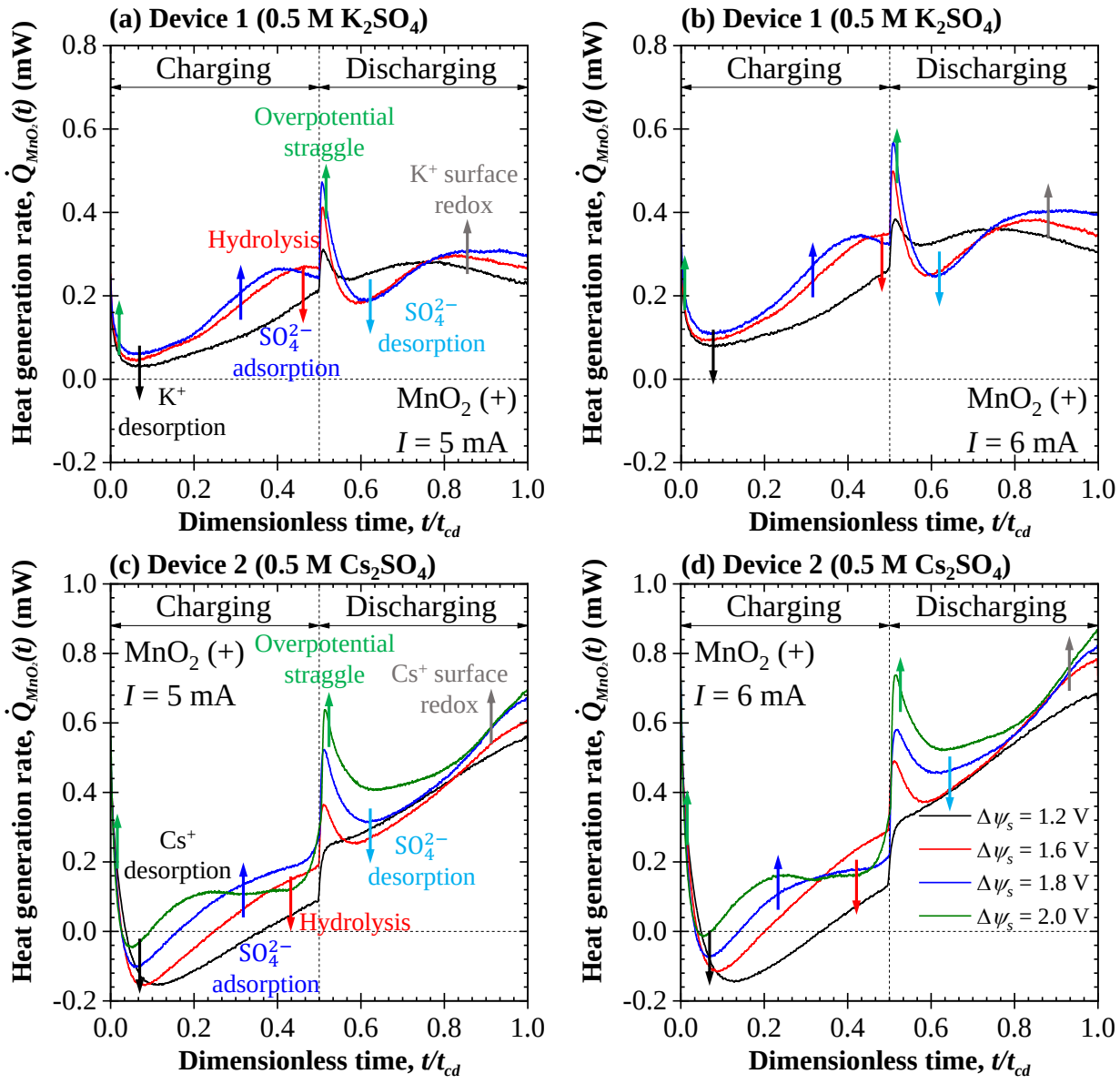

Figure 2.6: Instantaneous heat generation rate at the α-MnO_2 electrodes (a, b) for Device 1 in 0.5 M K_2SO_4 aqueous electrolyte for potential windows $\Delta\psi_s$ = 1.2, 1.6, and 1.8 V and (c, d) for Device 2 in 0.5 M Cs_2SO_4 aqueous electrolyte for potential windows $\Delta\psi_s$ = 1.2, 1.6, 1.8, and 2.0 V as a function of dimensionless time t/t_{cd} with decreased white noise for AC electrode subjected to imposed current of (a, c) I = 5 mA and (b, d) I = 6 mA.

measurements (Figures 2.2 and 2.4).

Moreover, the onset of hydrolysis occurred at a higher cell potential window $\Delta\psi_s$ for Cs_2SO_4 than for K_2SO_4 aqueous electrolyte. This may be attributed to the thinner solvation shell forming around Cs^+ cations [111]. The thin solvation shell combined with desolvation

of Cs^+ cations undergoing surface redox led to a lack of water molecules near the electrode surface where the potential was the largest. Although the electric potential may exceed the theoretical water electrochemical stability window of 1.23 V close to the electrode, hydrolysis cannot occur in the absence of water molecules. Similar delay in the onset of hydrolysis was observed by Suo et al. [124] using WISE systems in Li ion batteries with $LiMn_2O_4$-based cathode and Mo_6S_8-based anode.

Furthermore, in both devices at the beginning of the discharging step, a short spike in $\dot{Q}_{MnO_2}(t)$ appeared immediately after the current I switched from positive to negative. It was attributed to a straggle in the surface overpotential responsible for resistive losses and Joule heating as the current switched from positive to negative [77]. This behavior was more pronounced for larger potential windows when the straggle in overpotential was larger [77]. Such behavior was previously observed in numerical simulations [77] as well as experimentally [98]. Interestingly, this behavior could also be observed in the beginning of charging as the initially exothermic heat generation at $t/t_{cd} \simeq 0$. After the initial spike in heat generation rate, an endothermic dip caused by the endothermic desorption and solvation of the SO_4^{2-} ions accumulated during charging. Finally, $\dot{Q}_{MnO_2}(t)$ increased in the second part of the discharging step due to desolvation and exothermic surface redox involving K^+ (Device 1) or Cs^+ (Device 2) ions. This contribution started intensely and later decreased in intensity as the conditions became less favorable for surface redox reactions. This too was in agreement with previously reported experimental studies [24, 98] and numerical predictions [77].

Additional cyclic voltammetry measurements were performed on Device 2, after 30 galvanostatic cycles performed during *operando* calorimetry. Figure 2.7 shows the measured cyclic voltammograms for scan rate (a) $\nu = 10$ and (b) $\nu = 30$ mV/s for potential window ranging from 1.2 V to 2.0 V. For both scan rates ν, no sharp rise in current at high cell potential voltage ψ_s, often associated with hydrolysis reaction, was observed [101, 102, 117]. This unequivocally establishes that the early onset of hydrolysis could be observed with isothermal *operando* calorimetry before it could be observed with electrochemical measurements.

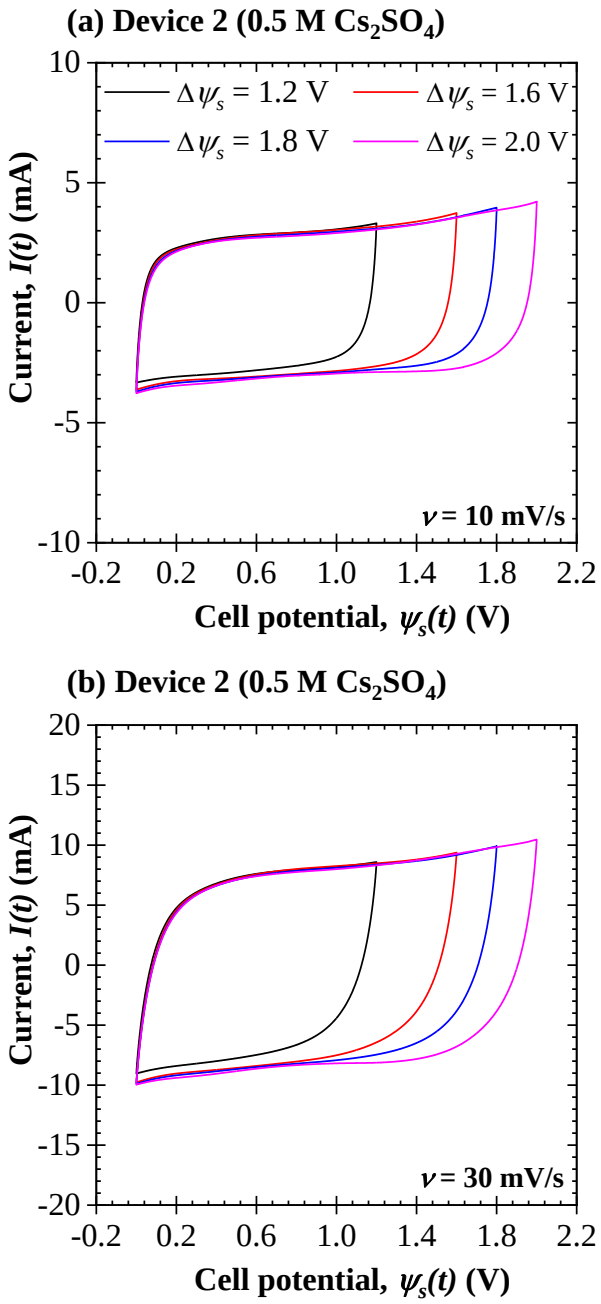

Figure 2.7: Cyclic voltammograms for Device 2 in 0.5 M Cs_2SO_4 aqueous electrolyte for potential windows $\Delta\psi_s$ = 1.2, 1.6, 1.8 V, and 2.0 V for scan rate (a) ν = 10 mV/s, and (b) ν = 30 mV/s after CV, GC, and calorimetric measurements.

2.4 Conclusion

This study reported measurements of the instantaneous heat generation rates at the positive α-MnO_2 cryptomelane and negative AC electrodes in hybrid supercapacitors with either 0.5

M K_2SO_4 or 0.5 M Cs_2SO_4 aqueous electrolytes with pH of 6.69 and 6.55, respectively. The measurements were performed in an *operando* isothermal calorimeter under galvanostatic cycling with potential window up to 1.8 V for the device with K_2SO_4 aqueous electrolyte and up to 2.0 V for the device with Cs_2SO_4 aqueous electrolyte. An endothermic dip observed at the AC electrodes in the beginning of the charging step was caused by anion desorption and solvation. Similar dips were observed at the α-MnO_2 electrodes also caused by cation and anion desorption and solvation. By contrast, exothermic peaks at the α-MnO_2 electrodes were attributed to cation surface redox, anion adsorption and desolvation, and overpotential straggle. Moreover, in both devices, an endothermic dip was observed at the positive electrode at the end of the charging step for the largest potential windows and was attributed to hydrolysis reaction. Interestingly, the onset of hydrolysis occurred at higher potentials significantly above 1.23 V in electrolytes with cations featuring a thinner solvation shell. Finally, the onset of hydrolysis could be detected by calorimetry before it could manifest itself in electrochemical measurements. Indeed, as the cell potential window was increased, the current remained small. However, hydrolysis is strongly endothermic and its thermal signature could be identified by the high sensitivity heat flux sensor in thermal contact with the positive $\alpha-MnO_2$ electrode.

CHAPTER 3

Contribution of ion solvation and desolvation to heat generation in hybrid supercapacitors

This chapter investigates the effect of ion solvation and desolvation on the heat generation in hybrid supercapacitors. In doing so, the thermal signature of ion desolvation and solvation was identified for the first time, as it was previously typically overshadowed by the thermal signature of adsorption and desorption. The investigated hybrid supercapacitors consisted of a positive α-MnO_2 cryptomelane pseudocapacitive electrode and an activated carbon counter electrode in (a) 0.25 M, (b) 0.75 M, or (c) 1.0 M $MgSO_4$ aqueous electrolytes with potential window of 1.6 V. $MgSO_4$ was chosen for its large enthalpy of solvation in water. The devices were characterized using cyclic voltammetry, electrochemical impedance spectroscopy, and galvanostatic cycling combined with isothermal *operando* calorimetry. The heat generation rates were measured at each electrode separately. The results indicated that the thermal signature of adsorption and desorption of Mg^{2+} and SO_4^{2-} ions dominated over that of partial desolvation and solvation of SO_4^{2-} ions at the AC electrode. However, at the α-MnO_2 electrodes the thermal signature of solvation and desolvation of Mg^{2+} ions dominated over that of desorption and adsorption or surface redox reaction. In fact, this phenomenon was not observed with K_2SO_4 and Cs_2SO_4 aqueous electrolytes featuring small enthalpy of solvation. This interpretation was confirmed by a simple thermal model for each electrode. Interestingly, the heat generation rate at each electrode scaled linearly with imposed current after correcting for Joule heating. The findings of this study could be used to shed light on the interfacial phenomena occurring during cycling of hybrid supercapacitors.

3.1 Background

In aqueous electrolytes, water molecules orient themselves in such a way that the oxygen atom faces the cations or one of the hydrogen atoms faces the anions [125]. As the salt crystals are surrounded by such oriented water molecules, repulsion between water molecules breaks the ionic bonds and the salt dissociates and dissolves [125]. The weaker bonds between the ions in the salt are broken due to the formation of new, stronger bonds between the ions and the solvent molecules. Such process is thermodynamically favorable under the conditions that the newly formed ion-solvent bonds are stronger than the solvent-solvent bonds and the ion-ion bonds [125]. The difference between the energy of the newly formed ion-solvent bonds and the energy of the broken ion-ion and solvent-solvent bonds is released as heat and is termed the enthalpy of solvation ΔH_{sol} [125]. The number of water molecules in the solvation shell surrounding an individual ion, also known as the hydration number h, depends on the charge and size of the ion [125, 126]. In practice, ions with larger charge and/or smaller diameter tend to form larger solvation shells and have larger enthalpy of solvation [113, 125, 126]. For example, the solvation shell of Mg^{2+} ions in water is larger than that of K^+ and Cs^+ [113, 125, 126]. Interestingly, salt concentration can also impact the solvation shell thickness and the hydration number of the dissociated ions [125, 126]. In fact, the hydration number h decreases with ion concentration as the interactions between ions become more significant [126].

3.2 Materials and methods

3.2.1 Electrode fabrication and device assembly

The fabrication method and device assembly was discussed in detail in Ref. [2] and need not be repeated. In brief, two different slurries were prepared by mixing either α-MnO_2 (Prince Erachem) or activated carbon (YP-50F, Kuraray Chemical) with carbon black (Superior Graphite, $> 99\%$) and polyvinylidene fluoride binder solution (PVDF, Kuraray Chemical) in a 70:15:15 weight ratio and stirring overnight. The binder solution was prepared by mixing

PVDF powder with dimethylacetamide (DMA) in an 8.5:91.5 weight ratio.

Each slurry was drop cast onto titanium mesh current collectors (Dexmet Corp.) and spread evenly with a spatula. The footprint area of all current collectors was 1 x 1 cm^2. The electrodes were then dried in an oven at 60 °C for 12 h. Finally, the electrodes were hot-roll calendered to a uniform thickness ranging between 46 and 48 μm for α-MnO_2 electrodes and between 65 and 86 μm for AC electrodes. The corresponding mass loading was between 5 and 8 mg for the α-MnO_2 electrodes and between 4.2 and 5.2 mg for the AC electrodes.

The assembled devices consisted of a positive α-MnO_2 electrode separated from the AC counter electrode by a 1 mm-thick, chemically inert, polypropylene mesh. The separator was impregnated with (i) 0.25 M $MgSO_4$ (Device 1), (ii) 0.75 M $MgSO_4$ (Device 2), or (iii) 1.0 M $MgSO_4$ (Device 3) aqueous electrolytes. These concentrations were chosen to be sufficiently high to ensure reasonable device capacity. Note that the electrolyte solution became sensibly warm to the touch when dissolving the $MgSO_4$ salt in water, indicative of the large enthalpy of solvation. Table 3.1 summarizes the mass loading of the individual negative AC and positive α-MnO_2 electrodes as well as the pH of the aqueous $MgSO_4$ electrolytes used in Devices 1, 2, and 3 with salt concentration of 0.25 M, 0.75 M, and 1.0 M. Table 3.2 summarizes the properties of $MgSO_4$ aqueous electrolyte.

Table 3.1: Characteristics of the investigated hybrid supercapacitors.

Property/parameter	**Device 1**	**Device 2**	**Device 3**
$MgSO_4$ concentration in DI water, c, (M)	0.25	0.75	1.0
Electrolyte pH	7.21	7.27	7.34
Active mass loading of AC, m_{AC} (mg)	4.27	4.27	5.17
AC electrode capacity at 10 mV/s, C_{AC} (mAh)	0.069	0.088	0.080
Active mass loading of α-MnO_2, m_{MnO_2} (mg)	5.04	5.04	8.12
α-MnO_2 electrode capacity at 10 mV/s, C_{MnO_2} (mAh)	0.052	0.064	0.116
Device internal resistance, R_s (Ω)	21.6 $\pm$ 0.6	12.2 $\pm$ 0.6	16.3 $\pm$ 0.5

Table 3.2: Properties of the aqueous $MgSO_4$ electrolyte used in the investigated hybrid supercapacitors.

Property/parameter	**Value**
Cation (Mg^{2+}) diameter, a_+ (nm) [110]	0.14
Solvated cation (Mg^{2+}) diameter, $a_{+,s}$ (nm) [113]	0.42
Anion (SO_4^{2-}) diameter, a_- (nm) [113]	0.48
Solvated anion (SO_4^{2-}) diameter, $a_{-,s}$ (nm) [113]	1.17
Diffusion coefficient of cations, $D_+ \times 10^{10}$ (m^2/s) [127]	7.090
Diffusion coefficient of anions, $D_- \times 10^{10}$ (m^2/s) [115]	8.090
Cation enthalpy of solvation, $\Delta H_{sol,+}$ (kJ/mol) [116]	-1921
Anion enthalpy of solvation, $\Delta H_{sol,-}$ (kJ/mol) [116]	-1059

3.2.2 Electrochemical characterization

Cyclic voltammetry was performed on each positive α-MnO_2 and negative AC electrode in a three electrode setup. The setup consisted of either the α-MnO_2 or AC working electrode, the elemental Ni foil (Sigma Aldrich) counter electrode, and an $Ag^+/AgCl$ reference electrode (Fisherbrand^{TM} accumet^{TM}) in (i) 0.25 M, (ii) 0.75 M, and (iii) 1.0 M $MgSO_4$ aqueous electrolyte. Each electrode was subjected to 95 cycles at scan rate $\nu = 10$ mV/s and an additional 5 cycles at scan rate $\nu = 5$ mV/s. The potential window was confined between $\psi_{s,min} = -0.8$ V and $\psi_{s,max} = 0.0$ V for the negative AC electrodes and $\psi_{s,min} = 0$ V and $\psi_{s,max} = 0.8$ V for the positive α-MnO_2 electrodes. The measurements were used to determine the capacity of each individual electrode according to [82]

$$C(\nu) = \oint \frac{I(\psi_s)}{2\nu} \mathrm{d}\psi_s. \tag{3.1}$$

Here, $I(\psi_s)$ was the current response corresponding to the time-dependent cell potential $\psi_s(t)$. The capacity $C(\nu)$ in C can be converted to mAh by dividing by 3.6.

Electrochemical impedance spectroscopy (EIS) was performed on the hybrid devices assembled inside the isothermal *operando* calorimeter at 20 °C to verify that they were properly assembled. The DC potential offset was $\psi_{DC} = 0.0$ V vs. ψ_{ocv} with a sinusoidal amplitude of $\psi_0 = 10$ mV while the frequency f ranged between 50 mHz and 200 kHz. Then, CV measurements were performed on the hybrid devices at scan rates ν ranging between 5 and 50 mV/s for 30 cycles at 20 °C. The cell potential window $\Delta\psi_s$ ranged between $\psi_{s,min} = 0.0$ V, and $\psi_{s,max} = 1.6$ V vs. the AC electrode. The gravimetric capacity $C_g(\nu) = C(\nu)/m$ of the assembled hybrid devices was also computed with $C(\nu)$ given by Equation (3.1) and m (in g) being the mass loading of active material in both the α-MnO_2 and AC electrodes.

3.2.3 Isothermal *operando* calorimetry

The instantaneous heat generation rates at each electrode were measured separately for all devices during galvanostatic cycling at current I ranging between 2 and 6 mA. The cell potential window $\Delta\psi_s$ was 1.6 V and the temperature T was 20 °C for all devices. Here, the cell potential window exceeded the electrochemical stability window of water of 1.23 V at 20 °C and pH of 7 [128]. However, our previous electrochemical measurements with K_2SO_4 and Cs_2SO_4 aqueous electrolytes and with α-MnO_2 and AC electrodes revealed that electrolysis did not occur at 1.6 V [2]. This was attributed to the nearly neutral pH of the electrolytes and the relatively thin hydration shell of K^+ and Cs^+ cations [2]. Here also, the pH of the electrolyte solution was nearly neutral and the hydration shell of Mg^{2+} was similar to that of K^+ and Cs^+.

The instantaneous heat generation rate $\dot{Q}_i(t)$ (in mW) at electrode "i" (i = AC or MnO_2) was computed from the heat flux q_i'' calculated from the voltage difference measured across the thermoelectric heat flux sensor (GreenTEG) in thermal contact with the back of the electrode according to [99]

$$\dot{Q}_i(t) = q_i''(t)A_i = \frac{\Delta V_i(t)}{S_i}A_i. \tag{3.2}$$

The surface area of the heat flux sensors A_i (in m^2) was the same as that of the electrodes while $\Delta V_i(t)$ was the measured instantaneous voltage drop across the heat flux sensor in thermal contact with the electrode and S_i was the sensitivity of the heat flux sensor (in $\mu V/(W/m^2)$) dependent on the temperature and provided by the manufacturer.

To ensure that an oscillatory steady-state operation had been reached, the devices were cycled for 30 consecutive cycles at each imposed current I ranging from 2 to 6 mA. The heat generation rate at electrode "i" was then averaged over the last 5 of the 30 consecutive cycles to eliminate the white noise in the measurements according to

$$\dot{Q}_i(t) = \frac{1}{5}\sum_{j=26}^{30} \dot{Q}_i(t + (j-1)t_{cd}). \tag{3.3}$$

Here, t_{cd} referred to a charge/discharge period of one cycle and index j denoted the cycle number between 26 and 30.

The time-averaged irreversible heat generation rate of the cycle can be defined as

$$\bar{\dot{Q}}_{irr,i} = \bar{\dot{Q}}_i = \frac{1}{t_{cd}} \int_{(n_c-1)t_{cd}}^{n_c t_{cd}} \dot{Q}_i(t)\,\mathrm{d}t, \tag{3.4}$$

where n_c was the cycle number and t_{cd} was the cycle period. Indeed, by definition, averaging the instantaneous reversible heat generation rate over an entire cycle yields zero, i.e., $\bar{\dot{Q}}_{rev} = 0$.

Finally, the IR drop observed in the measured potential vs. time curves after reversing the current was used to compute the internal resistance of the devices according to [1, 78–80]

$$R_s(I) = \frac{\psi_s(t_c^+) - \psi_s(t_c^-)}{2I}. \tag{3.5}$$

Here, $\psi_s(t_c^+)$ referred to the cell potential at the current switch and $\psi_s(t_c^-)$ referred to the cell potential 10 ms after the current switch, as recommended in Ref. [79].

3.3 Analysis

D'Entremont and Pilon derived, from first principles, two thermal models predicting the instantaneous heat generation rate in EDLCs [75] and hybrid supercapacitors [77]. The models accounted for irreversible heat generation associated with (i) Joule heating and (ii) redox reactions at the pseudocapacitive electrode, as well as reversible heat generation caused by (iii) ion adsorption/desorption and (iv) reversible redox reactions at the pseudocapacitive electrode. The irreversible contributions were strictly exothermic. The reversible heat generation rate was exothermic due to ion adsorption and spontaneous redox reactions and endothermic for ion desorption and non-spontaneous redox reactions [75, 77]. However, in these models the ion size was assumed to be constant for cations and anions and independent of concentration [75, 77]. In other words, ion solvation and desolvation were ignored.

The process of spontaneous ion solvation in water is exothermic. During galvanostatic cycling at constant current I, bare ions are transported from a porous electrode with mass loading of active material $m_{a,i}$ (in mg) and BET specific surface area a_i (in m^2/g) such that the molar flux $n''_{j,i}$ (in mol/m^2s) of ion species "j" satisfies $n''_{j,i} m_i a_i F z_j = I$ where F is the Faraday constant (F = 96485.33 C/mol). The heat generation rate associated with the solvation of bare ions released from the electrode surface can be expressed as

$$\dot{Q}^j_{sol,i}(t) = \eta n''_j A_i \Delta H^j_{sol} = \frac{\eta a_i m_{a,i}}{z_j F} \Delta H^j_{sol} I, \tag{3.6}$$

where η is the extent of solvation ($0 \leq \eta \leq 1$) and A_i is the surface area of the active material "i" ("i" = AC or MnO_2) such that $A_i = a_i m_{a,i}$.

Overall, the total instantaneous heat generation rate $\dot{Q}_{T,AC}(t)$ at the AC electrode during charging can be written as

$$\dot{Q}_{T,AC}(t) = \dot{Q}_{J,AC}(t) + \dot{Q}_{rev,EDL,AC}(t) + \sum_{j=1}^{2} \dot{Q}^j_{sol,AC}(t). \tag{3.7}$$

Here, the Joule heating term $\dot{Q}_{J,AC}(t)$ was proportional to I^2 while the reversible heat gen-

eration rate $\dot{Q}_{rev,EDL,AC}(t)$ due to SO_4^{2-} desorption and Mg^{2+} ion adsorption has been found to be linearly proportional to current I [75,77]. Please note, that during discharging the processes were reversed and the sign of the heat reversible heat generation terms was switched. Thus, Equation (3.7) can be written as

$$\dot{Q}_{T,AC}(t) = R_{AC}I^2 + \alpha_{AC}(t)I + \frac{\eta a_{AC} m_{AC}}{z_{SO_4^{2-}} F} \Delta H_{sol}^{SO_4^{2-}} I, \tag{3.8}$$

where $R_{AC} = 8\ \Omega$ was the electrical resistance of the AC half-cell while $\alpha_{AC}(t)$ was an empirical coefficient associated with ion adsorption at the AC electrode whose value varied linearly between -0.1 and 0.1 W/A based on experimental data reported in Ref. [24]. The bare and solvated ion diameters of SO_4^{2-} were 0.48 nm and 1.17 nm, respectively (Table 3.2). The peak pore size of YP-50F AC was 0.7 nm while ~50 % of the pores were larger than 1.17 nm [129]. Therefore, partial desolvation of SO_4^{2-} anions was expected upon their adsorption. Here, the extent of solvation of SO_4^{2-} anions η was assumed to be 0.1 based on DFT study of ion solvation in nanopores [130]. Moreover, the BET specific surface area a_{AC} of the AC electrode was taken as 1000 m^2/g [129]. However, in a typical AC electrode only ~20 % of the total surface area required some degree of ion desolvation upon adsorption [131] reducing a_{AC} to 200 m^2/g.

Similarly, the total instantaneous heat generation rate $\dot{Q}_{T,MnO_2}(t)$ at the α-MnO_2 electrode can be written as

$$\begin{aligned}\dot{Q}_{T,MnO_2}(t) =& \dot{Q}_{J,MnO_2}(t) + \dot{Q}_{rev,EDL,MnO_2}(t) + \sum_{j=1}^{2} \dot{Q}^{j}_{sol,MnO_2}(t) \\ &+ \dot{Q}_{rev,F,MnO_2}(t) + \dot{Q}_{irr,F,MnO_2}(t).\end{aligned} \tag{3.9}$$

Please note that during charging only SO_4^{2-} anions participated in EDL formation and contributed to $\dot{Q}_{rev,EDL,MnO_2}(t)$. Conversely, Mg^{2+} cations undergoing surface redox reaction contributed to $\dot{Q}_{rev,F,MnO_2}(t)$ and $\dot{Q}_{irr,F,MnO_2}(t)$, respectively. These processes were reversed during discharging. Moreover, the so-called faradaic current I_F emerged at the α-MnO_2 electrode due to redox reactions. Interestingly, the reversible and irreversible heat generation

rates $\dot{Q}_{rev,F,MnO_2}(t)$ and $\dot{Q}_{irr,F,MnO_2}(t)$ due to redox reactions were found to be linearly proportional to the faradaic current I_F [77]. As redox reactions typically dominate the charge storage in hybrid supercapacitors, faradaic current I_F is typically equal to the total current I [77, 112]. Then, Equation (3.9) can be written as

$$\dot{Q}_{T,MnO_2}(t) = R_{MnO_2} I^2 + \left(\alpha_{MnO_2}(t) + \frac{\eta a_{MnO_2} m_{MnO_2}}{zF} \Delta H_{sol}^{Mg^{2+}} + \beta_{MnO_2}(t) + \gamma_{MnO_2}(t) \right) I. \tag{3.10}$$

Here, $R_{MnO_2} = 8\ \Omega$ was the electrical resistance of the α-MnO_2 half-cell while $\alpha_{MnO_2}(t)$ was an empirical coefficient associated with ion adsorption at the α-MnO_2 electrode and varied linearly between 0 and 0.1 W/A based on experimental data reported in Ref. [24]. Furthermore, $\beta_{MnO_2}(t)$ and $\gamma_{MnO_2}(t)$ were coefficients related to the reversible and irreversible heat generation due to redox reactions at the α-MnO_2 electrode, respectively. Here, $\beta_{MnO_2}(t)$ was between -0.1 and 0.1 W/A based on experimental results reported in Ref. [24] and $\gamma_{MnO_2}(t)$ varied linearly between 0 and 0.025 W/A based on the reported values for highly reversible redox reactions [77]. Please note that SO_4^{2-} anions did not get desolvated upon adsorption at the mesoporous α-MnO_2 electrode as the pores in α-MnO_2 were larger than the solvated SO_4^{2-} anions [109]. However, Mg^{2+} cations were completely desolvated when participating in redox reactions at the α-MnO_2 electrode [132] and their enthalpy of solvation $\Delta H_{sol}^{Mg^{2+}}$ contributed to $\dot{Q}_{sol,MnO_2}^{Mg^{2+}}(t)$. Finally, the BET specific surface area a_{MnO_2} was 200 m^2/g [109].

3.4 Results and discussion

3.4.1 Cyclic voltammetry

3.4.1.1 Three-electrode measurements

The mass loading of the different AC electrodes was similar and resulted in similar capacity $C(\nu)$ ranging between 0.069 and 0.088 mAh for scan rate $\nu = 10$ mV/s (see Figure S1 in Supplementary Material). By contrast, the mass loading of the α-MnO_2 electrodes differed

leading to a broader range of capacity $C(\nu)$ between 0.064 mAh and 0.116 mAh. Nevertheless, the electrodes were paired so that the capacity of the α-MnO_2 electrodes matched well with the capacity of the AC electrodes. Table 3.1 reports the capacity of the individual AC and α-MnO_2 electrodes measured at scan rate $\nu = 10$ mV/s. Note that during the cycling, no bubbles formed on the surface of any electrodes indicating that the electrolyte was stable under $\pm$ 0.8 V vs. Ag^+/AgCl reference electrode.

3.4.1.2 Assembled device

Figure S2 in Supplementary Material shows cyclic voltammetry performed on the assembled devices for scan rate ν ranging between 5 and 50 mV/s and cell potential $\Delta\psi_s$ of 1.6 V. For all devices, the magnitude of the current response $I(t)$ increased with increasing scan rate ν and the CV curves changed from a rectangular to a leaf-like shape indicative of a resistive behavior. The latter was the most prominent in Device 3 due to the larger mass loading of both electrodes (Table 3.1). In addition, the resistive behavior was more pronounced in Device 1 than in Device 2 due to its lower electrolyte concentration and therefore larger resistance. Finally, although the cell potential $\psi_s(t)$ exceeded the electrochemical stability window of 1.23 V for water at 20 °C and neutral pH, no rapid raise in current, indicative of hydrolysis, was observed [117, 118].

Figure 3.1 shows the devices (a) capacity $C(\nu)$ and (b) the gravimetric capacity $C_g(\nu)$ as functions of scan rate ν, (c) the cell resistance R_s calculated from the IR drop based on Equation (3.5), and (d) the Nyquist plots obtained from the EIS measurements. Figures 3.1(a) and 3.1(b) reveal that the capacity $C(\nu)$ of the devices systematically increased with increasing electrolyte concentration. Figures 3.1(a) and 3.1(b) also indicate that both the capacity $C(\nu)$ and the gravimetric capacity $C_g(\nu)$ decreased with increasing scan rate ν. This was consistent with previous experimental studies and was attributed to ion diffusion limitations [24, 119–121]. Moreover, the faster fade in capacity $C(\nu)$ with increasing scan rate ν and the slightly lower gravimetric capacity $C_g(\nu)$ of Device 3 were due to its larger resistance. Figure 3.1(c) indicates that R_s was independent of current I for all devices.

These results were also consistent with those obtained from the Nyquist plots [Figure 3.1(d)] interpreted based on our previous studies [1, 89]. The internal resistance of Device 1 was the largest with $R_s = 21.58 \pm 0.63\ \Omega$, due to the lowest electrolyte concentration. Device 3 had the second largest internal resistance $R_s = 16.27 \pm 0.63\ \Omega$ due to its large mass loading (Table 3.1). Finally, Device 2 had the lowest internal resistance with $R_s = 12.23 \pm 0.45\ \Omega$ resulting from the combined effects of a smaller mass loading and a relatively large electrolyte concentration. This was consistent with the trends observed in the gravimetric capacity $C_g(\nu)$ [Figure 3.1(b)].

3.4.2 Galvanostatic cycling

Figure 3.2 shows the cell potential $\psi_s(t)$ as a function of time t during galvanostatic cycling for a cell potential window $\Delta\psi_s = 1.6$ V and electric current I between 2 and 6 mA for (a) Device 1, (b) Device 2, and (c) Device 3 (Table 3.1). The cell potential $\psi_s(t)$ varied almost linearly with time for all three devices for the majority of the cycle, except for the IR drop when the current switched signs. Such behavior is typical of EDLCs and hybrid supercapacitors with fast surface redox reactions and has been observed previously in similar systems [16, 76, 101, 102]. For any given current, the cycle period t_{cd} was the shortest for Device 1, followed by Device 2 while it was the longest for Device 3, as expected from their increasing capacity $C(\nu)$ [Figure 3.1(a)] and attributed to the larger amount of ions in the electrolyte available for charge storage.

3.4.3 Isothermal *operando* calorimetry

3.4.3.1 Instantaneous heat generation rates

Activated carbon electrodes

Figures 3.3(a)-3.3(c) show the instantaneous heat generation rate $\dot{Q}_{AC}(t)$ at the AC electrode for current I ranging between 2 and 6 mA and potential window $\Delta\psi_s = 1.6$ V as a function of dimensionless time t/t_{cd} for (a) Device 1, (b) Device 2, and (c) Device 3 (Table 3.1). At

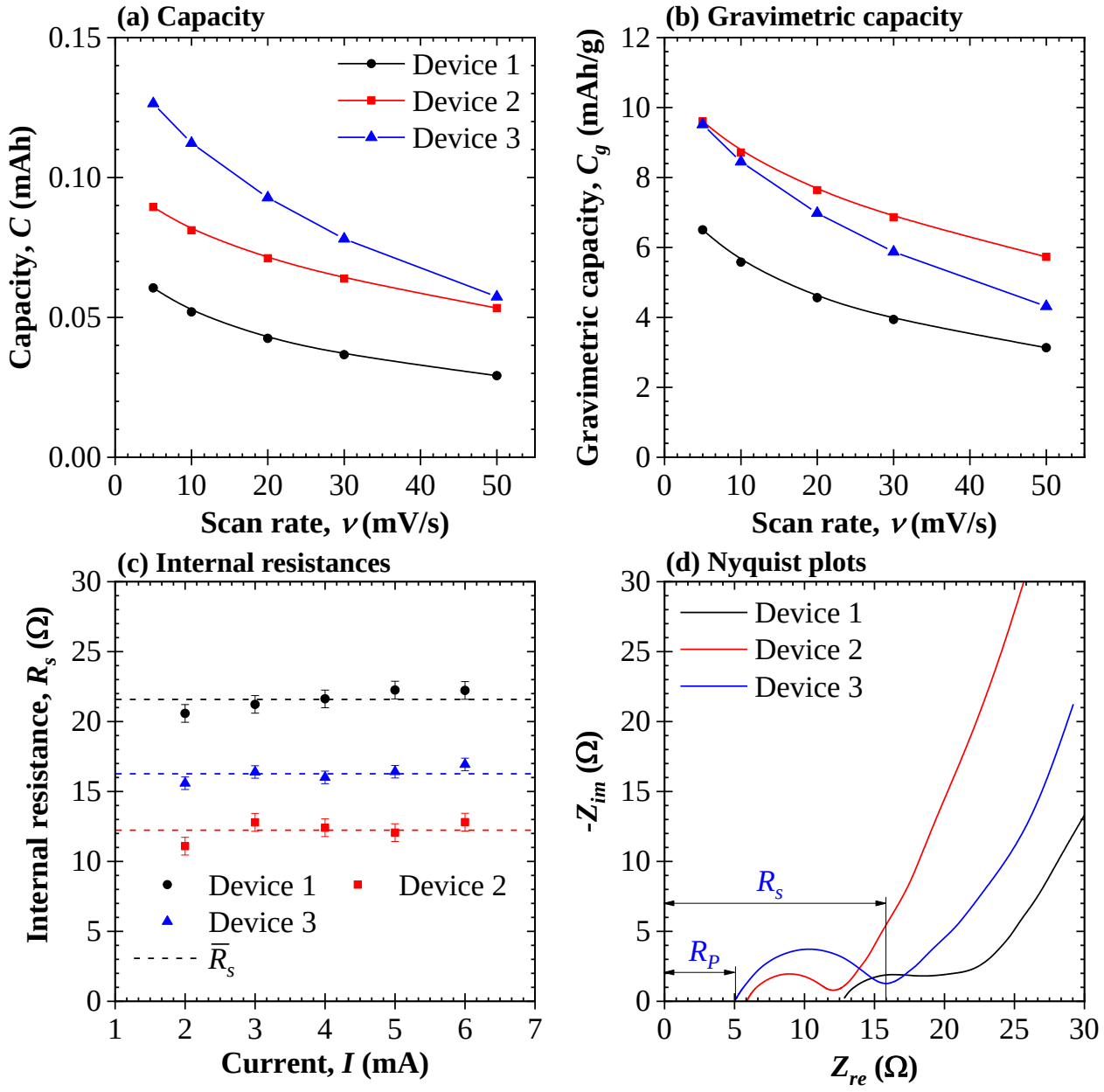

Figure 3.1: (a) Capacity $C(\nu)$, (b) gravimetric capacity $C_g(\nu)$ per unit mass of both electrodes as functions of scan rate ν, (c) internal resistance R_s as a function of the imposed current I, and (d) Nyquist plots of Device 1, Device 2, and Device 3 with 0.25 M, 0.75 M, and 1.0 M $MgSO_4$ aqueous electrolyte, respectively (Table 3.1).

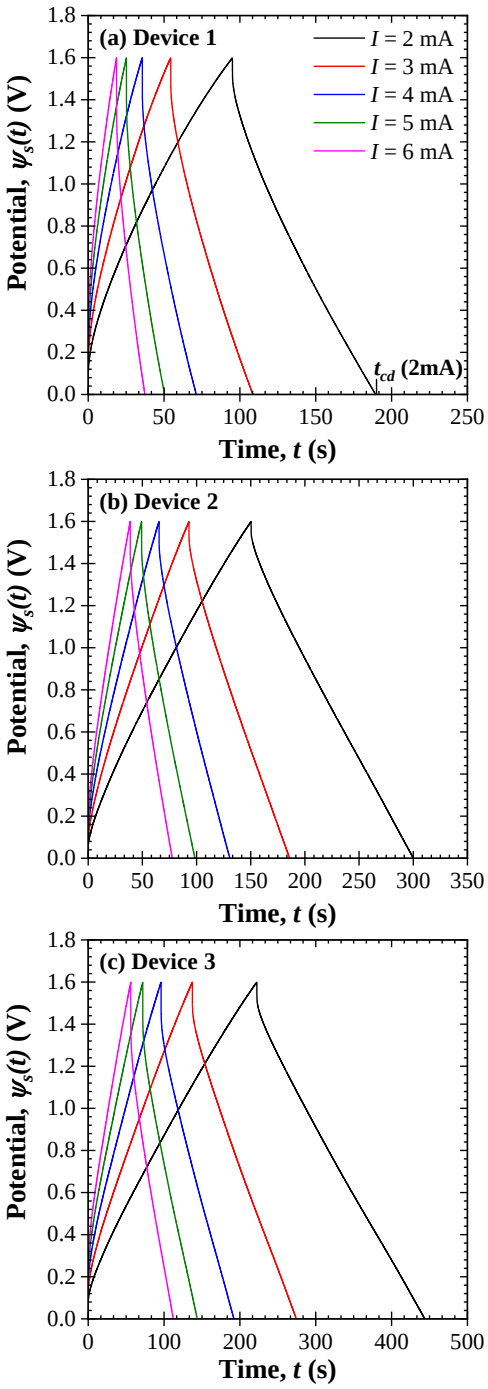

Figure 3.2: Cell potential $\psi_s(t)$ as a function of time under galvanostatic cycling with potential window $\Delta\psi_s = 1.6$ V and electric current I ranging between 2 and 6 mA for (a) Device 1, (b) Device 2, and (c) Device 3 with 0.25 M, 0.75 M, and 1.0 M $MgSO_4$ aqueous electrolyte, respectively.

the beginning of the charging step, an endothermic dip was observed for all AC electrodes. As the charging progressed the heat generation rate became positive and increased over time for all AC electrodes. Furthermore, at the beginning of the discharging step, the heat generation rate featured another dip. This dip was wider and persisted for a longer part of the discharging step at lower current I. Finally, for the second half of the discharging step, the heat generation rate increased. Similar behavior has been observed in EDLCs with AC electrodes [61, 99–101] and at the AC electrode of hybrid supercapacitors in numerous electrolytes including aqueous Na_2SO_4 [24], K_2SO_4 [2], and Cs_2SO_4 [2]. Interestingly, the heat generation rate $\dot{Q}_{AC}(t)$ decreased with increasing electrolyte concentration. This was due to the smaller electrolyte resistance as the ionic conductivity of the electrolyte increased with increasing $MgSO_4$ salt concentrations.

Cryptomelane electrodes

Figures 3.3(d)-3.3(f) show the instantaneous heat generation rate $\dot{Q}_{MnO_2}(t)$ at the α-MnO_2 electrode for current I ranging between 2 and 6 mA and a potential window $\Delta\psi_s = 1.6$ V as a function of dimensionless time t/t_{cd} for (d) Device 1, (e) Device 2, and (f) Device 3 (Table 3.1). The heat generation rate $\dot{Q}_{MnO_2}(t)$ was strictly positive for all devices and currents considered and exhibited the same behavior for all devices. Increasing the $MgSO_4$ salt concentration from 0.25 M (Device 1) to 0.75 M (Device 2) resulted in smaller heat generation rate $\dot{Q}_{MnO_2}(t)$ due to the decrease in the internal resistance R_s [Figure 3.1(c)]. Moreover, upon further increasing $MgSO_4$ salt concentration to 1.0 M (Device 3), the heat generation rate $\dot{Q}_{MnO_2}(t)$ increased due to the larger amount of ions contributing to charge storage as indicated by the larger capacity [Figure 3.1(a)]. At the beginning of the charging step, $\dot{Q}_{MnO_2}(t)$ sharply increased towards a plateau which persisted for the rest of the charging step. Then, at the beginning of the discharging step, it dropped sharply towards another plateau. For Devices 1 and 2, $\dot{Q}_{MnO_2}(t)$ increased slightly in the second part of the charging step possibly due to the ion starvation in the electrolytes of the lowest concentrations.

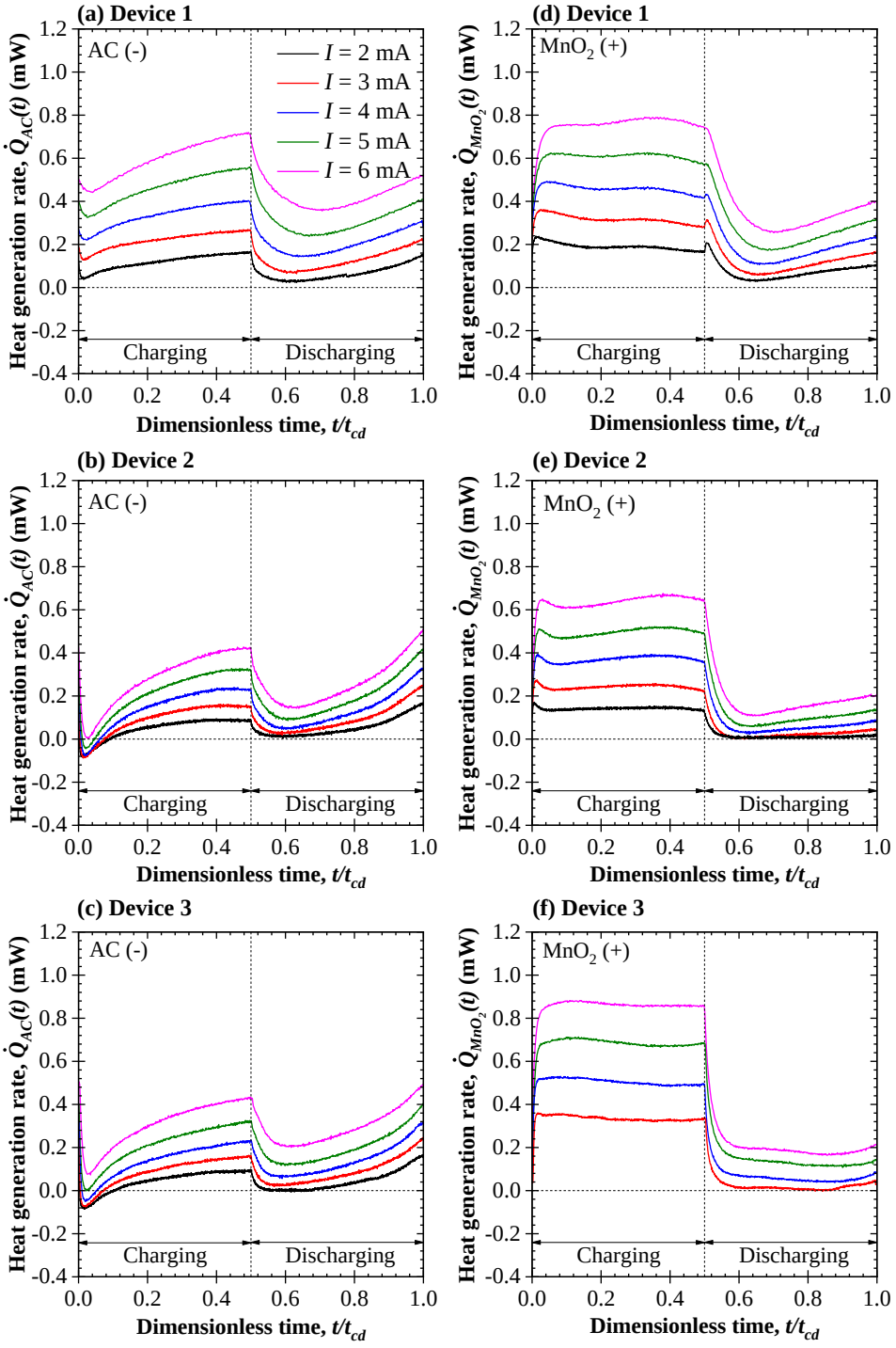

Figure 3.3: The instantaneous heat generation rate at the AC electrodes $\dot{Q}_{AC}(t)$ for (a) Device 1, (b) Device 2, and (c) Device 3 and the instantaneous heat generation rates at the α-MnO_2 electrodes $\dot{Q}_{MnO_2}(t)$ for (d) Device 1, (e) Device 2, and (f) Device 3 with 0.25 M, 0.75 M, and 1.0 M $MgSO_4$ aqueous electrolyte, respectively (Table 3.1), and for current I ranging between 2 and 6 mA as functions of dimensionless time t/t_{cd}.

Effect of ion species

Figure 3.4 compares the previously reported instantaneous heat generation rate at (a, b) the AC electrodes $\dot{Q}_{AC}(t)$ and (c, d) α-MnO_2 electrodes $\dot{Q}_{MnO_2}(t)$ of hybrid supercapacitors with 0.5 M K_2SO_4 [2], and 0.5 M Cs_2SO_4 [2] aqueous electrolytes, with the present measurements for 1.0 M $MgSO_4$ aqueous electrolyte, for the same potential window of 1.6 V and current (a, c) $I = 5$ mA and (b, d) $I = 6$ mA as functions of dimensionless time t/t_{cd}. Similar trends in the heat generation rate $\dot{Q}_{AC}(t)$ were observed at the AC electrode among all electrolytes. However, the heat generation rate at the α-MnO_2 electrodes was similar in 0.5 M K_2SO_4 and Cs_2SO_4 aqueous electrolytes and exhibited large fluctuations during cycling as it was dominated by ion adsorption and desorption, and surface redox reactions [2]. By contrast, the heat generation rate $\dot{Q}_{MnO_2}(t)$ at the α-MnO_2 electrode in 1.0 M $MgSO_4$ aqueous electrolyte was different from that observed in 0.5 M K_2SO_4 and 0.5 M Cs_2SO_4 despite maintaining the same number of moles of cations and anions. In fact, $\dot{Q}_{MnO_2}(t)$ was strictly positive and exhibited a plateau during the charging and discharging steps. This could be due to the significantly larger enthalpy of solvation of Mg^{2+} (-1921 kJ/mol [116]) compared to that of K^+ (-322 kJ/mol [116]) and Cs^+ (-264 kJ/mol [116]). This hypothesis will be elucidated in the following sections.

3.4.3.2 Time-averaged heat generation rate

Figure 3.5 shows the time-averaged irreversible heat generation rate $\bar{\dot{Q}}_{irr,i}$ at electrode "i" (i = AC or MnO_2) and the time-averaged total heat generation rate $\bar{\dot{Q}}_T$ as functions of I^2 for (a) Device 1, (b) Device 2, and (c) Device 3, computed according to Equation (3.4). Irreversible heat generation at the AC electrode $\bar{\dot{Q}}_{irr,AC}$ was linearly proportional to I^2 and attributed to Joule heating. This was consistent with previous experimental [24, 98, 99, 104] and numerical [75] studies. Then, the resistance R_{AC} of the AC half-cell can be estimated as $R_{AC} = \bar{\dot{Q}}_{J,AC}/I^2 = \bar{\dot{Q}}_{irr,AC}/I^2$. Although the AC electrode in Device 1 and Device 2 was the same, the resistance of the AC half-cell R_{AC} decreased from 14.0 Ω to 7.3 Ω as the electrolyte concentration increased from 0.25 M to 0.75 M. Moreover, the AC half-cell resistance R_{AC}

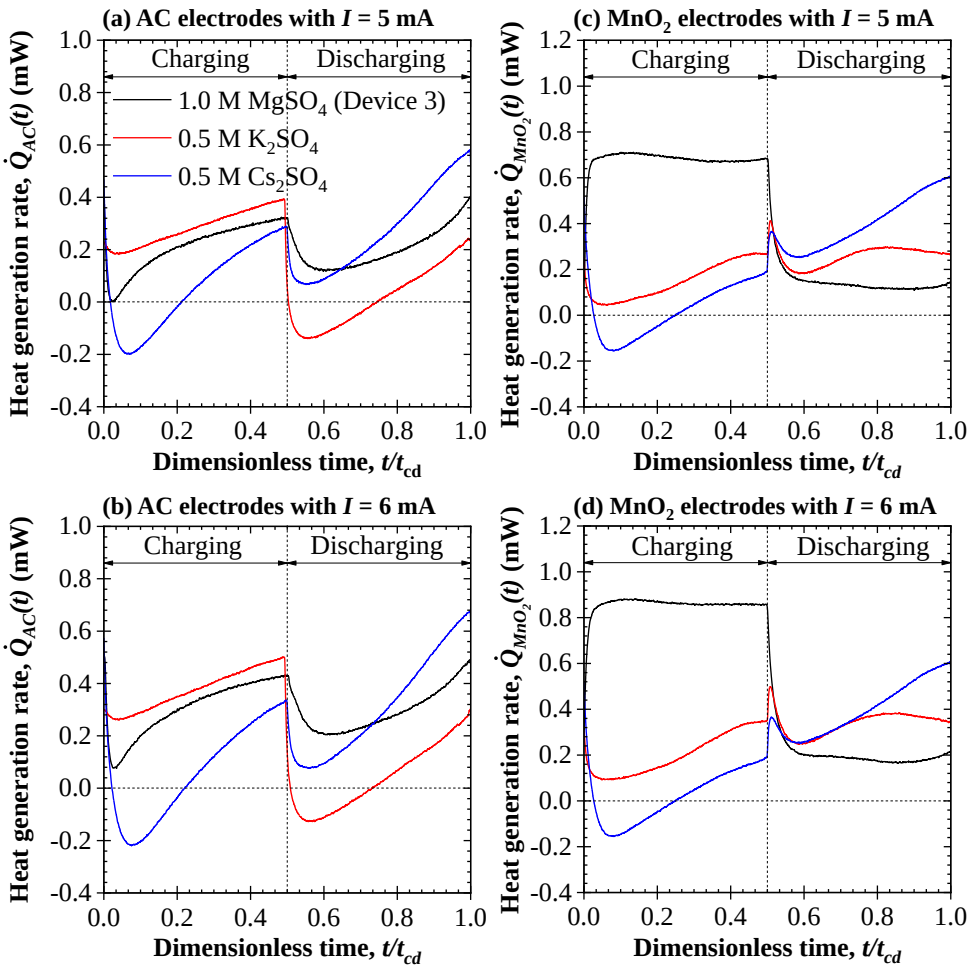

Figure 3.4: The instantaneous heat generation rate at (a, b) the AC electrodes $\dot{Q}_{AC}(t)$ and (c, d) the α-MnO_2 electrodes $\dot{Q}_{MnO_2}(t)$ for hybrid supercapacitors with 1.0 M $MgSO_4$ (Device 3), 0.5 M K_2SO_4 [2], and 0.5 M Cs_2SO_4 [2] aqueous electrolytes, with (a, c) $I = 5$ mA and (b, d) $I = 6$ mA as functions of dimensionless time t/t_{cd}.

$= 8.2\ \Omega$ of Device 3 was larger than that of Device 2 due to the larger mass loading of its AC electrode despite the larger electrolyte concentration (Table 3.1).

The electrical resistance of the α-MnO_2 half-cell could be computed as $R_{MnO_2} = R_s - R_{AC}$ where R_s is the total cell resistance measured from the IR drop [Figure 3.1(c)] and R_{AC} is the resistance of the AC half-cell. Note that the resistance of the pseudocapacitive electrode is expected to be constant throughout the cycling as ions do not intercalate significantly to

change the α-MnO_2 conductivity. Figure 3.5 also indicates that the total irreversible heat generation rate $\bar{\dot{Q}}_{irr,T}$ exceeded Joule heating predicted as $\bar{\dot{Q}}_J = R_s I^2$. This was due to the irreversible heat generation due to redox reactions and concentration hysteresis in the α-MnO_2 electrode as observed previously experimentally [24] and numerically [77].

3.4.3.3 Reversible heat generation rates

Activated carbon electrodes

As established previously, the irreversible heat generation at the AC electrodes was due to Joule heating only and thus was constant with time, i.e., $\dot{Q}_{J,AC}(t) = \bar{\dot{Q}}_{irr,AC} = R_{AC} I^2$ [61, 99, 101, 102, 104]. Therefore, the reversible heat generation at the AC electrodes can be expressed as $\dot{Q}_{rev,AC}(t) = \dot{Q}_{AC}(t) - \bar{\dot{Q}}_{irr,AC}$. Figures 3.6(a)-3.6(c) show the instantaneous reversible heat generation rate at the AC electrode $\dot{Q}_{rev,AC}(t)$ as a function of dimensionless time t/t_{cd} for (a) Device 1, (b) Device 2, and (c) Device 3 with 0.25 M, 0.75 M, and 1.0 M $MgSO_4$ aqueous electrolyte, respectively, for current I ranging between 2 and 6 mA and potential $\Delta\psi_s = 1.6$ V. Moreover, Figures 3.6(d)-3.6(f) show the same data plotted as $\dot{Q}_{rev,AC}(t)/I$ vs. t/t_{cd}. It is interesting to note that scaling the reversible heat generation rates $\dot{Q}_{rev,AC}(t)$ by the current I made the data nearly collapse on top of each other at all dimensionless time t/t_{cd}. These results confirm that, indeed, $\dot{Q}_{rev,AC}(t)$ scaled linearly with current I for the AC electrode, as previously observed numerically by d'Entremont and Pilon [75]. The slight deviation observed at higher currents I in Device 3 was attributed to diffusion limitations due the higher electrode mass loading (Table 3.1) and therefore larger resistance of the AC electrode [Figure 3.1(c)].

The endothermic dip observed at the beginning of the charging step was attributed to SO_4^{2-} desorption from the AC electrodes. Note that the previously adsorbed SO_4^{2-} anions were only partially desolvated as their solvated ion size of 1.17 nm (Table 3.2) was larger than the peak pore size of YP-50F AC reported to be 0.7 nm [129]. Similar partial desolvation of largely solvated ions was observed in electrode films consisting of titanium-carbide-derived carbon (TiC-CDC) and PTFE with 1.5 M tetraethylammonium tetrafluoroborate in ace-

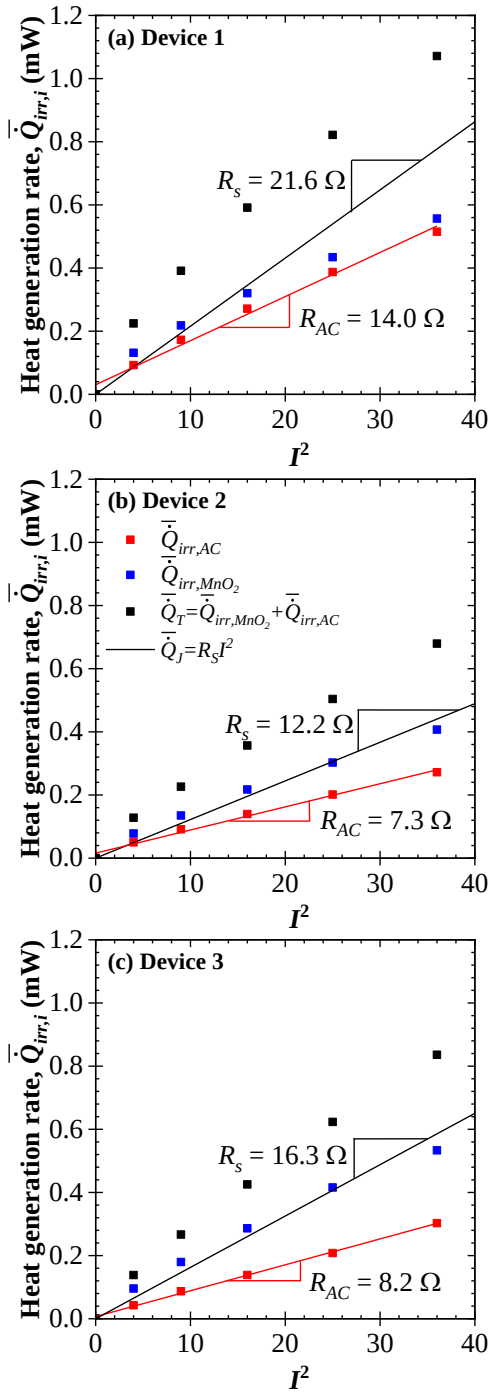

Figure 3.5: The average irreversible heat generation rates $\bar{\dot{Q}}_{irr,i}$ as functions of I^2 for (a) Device 1, (b) Device 2, and (c) Device 3 with 0.25 M, 0.75 M, and 1.0 M $MgSO_4$ aqueous electrolyte, respectively (Table 3.1).

tonitrile [133] and Ti-CDC and PVDF with either neat EMI-TFSI or 2 M EMI-TFSI in acetonitrile [134]. Therefore, the process of SO_4^{2-} desorption was accompanied by partial SO_4^{2-} solvation which is exothermic. However, the observed dip established that the process of SO_4^{2-} desorption dominated the thermal signature. After the initial dip, $\dot{Q}_{rev,AC}(t)$ became positive due to the exothermic Mg^{2+} adsorption. The process of Mg^{2+} adsorption was unlikely to trigger the endothermic partial desolvation of Mg^{2+} inside the pores as the solvated cation diameter of Mg^{2+} of 0.42 nm (Table 3.2) was smaller than the peak pore size of YP-50F AC [129]. Then, at the beginning of the discharging step $\dot{Q}_{rev,AC}(t)$ became negative due to Mg^{2+} desorption. Finally, $\dot{Q}_{rev,AC}(t)$ became positive again when exothermic SO_4^{2-} adsorption dominated over endothermic SO_4^{2-} partial desolvation.

Cryptomelane electrodes

The total heat generation in the cell associated with Joule heating can be expressed as $\bar{\dot{Q}}_{J,T} = R_s I^2$ so that Joule heating at the α-MnO_2 half-cell can be written as $\bar{\dot{Q}}_{J,MnO_2} = \bar{\dot{Q}}_{J,T} - \bar{\dot{Q}}_{irr,AC} = (R_s - R_{AC})I^2 = R_{MnO_2} I^2$. The instantaneous heat generation rate at the α-MnO_2 electrode $\dot{Q}_{MnO_2}(t)$ consisted not only of Joule heating $\dot{Q}_{J,MnO_2}(t)$ but also of (i) reversible heat generation due to EDL formation/dissolution $\dot{Q}_{rev,EDL,MnO_2}(t)$, (ii) reversible heat generation due to redox reactions $\dot{Q}_{rev,F,MnO_2}(t)$, (iii) reversible heat generation due to solvation/desolvation of ions $\dot{Q}_{rev,sol,MnO_2}(t)$, and (iv) irreversible heat generation due to redox reactions $\dot{Q}_{irr,F,MnO_2}(t)$ [77]. Then, the Joule heating contribution at the α-MnO_2 electrode $\dot{Q}_{J,MnO_2}(t) = R_{MnO_2} I^2$ can be subtracted from the instantaneous heat generation $\dot{Q}_{MnO_2}(t)$ as $\dot{Q}_{MnO_2}(t) - \dot{Q}_{J,MnO_2}(t) = \dot{Q}_{rev,MnO_2}(t) + \dot{Q}_{irr,F,MnO_2}(t)$ where the reversible heat generation rate $\dot{Q}_{rev,MnO_2}(t)$ can be expressed as $\dot{Q}_{rev,MnO_2}(t) = \dot{Q}_{rev,EDL,MnO_2}(t) + \dot{Q}_{rev,F,MnO_2}(t) + \dot{Q}_{rev,sol,MnO_2}(t)$. Figures 3.7(a)-3.7(c) show the instantaneous heat generation rate at the α-MnO_2 electrode with subtracted Joule heating $\dot{Q}_{MnO_2}(t) - \bar{\dot{Q}}_{J,MnO_2}$ as a function of dimensionless time t/t_{cd} for current I ranging between 2 and 6 mA and a potential window $\Delta\psi_s = 1.6$ V for (a) Device 1, (b) Device 2, and (c) Device 3 with 0.25 M, 0.75 M, and 1.0 M $MgSO_4$ aqueous electrolyte, respectively. They establish that $\dot{Q}_{MnO_2}(t) - \bar{\dot{Q}}_{J,MnO_2}$ remained entirely exothermic for Device 1 [Figure 3.7(a)] and became slightly endothermic during the

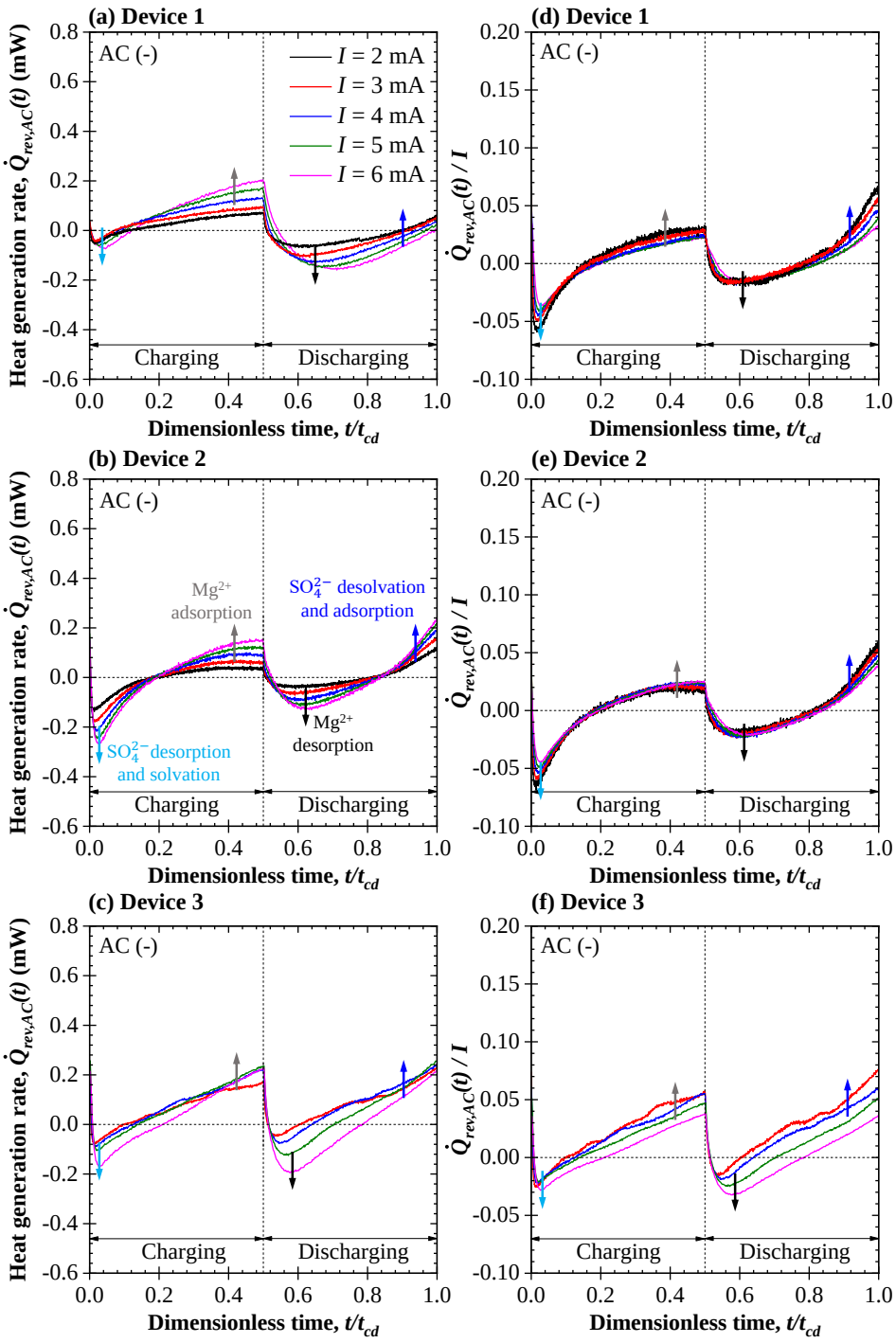

Figure 3.6: The instantaneous reversible heat generation rate at the AC electrode $\dot{Q}_{rev,AC}(t)$ for (a) Device 1, (b) Device 2, and (d) Device 3 and the same data plotted as $\dot{Q}_{rev,AC}(t)/I$ for (d) Device 1, (e) Device 2, and (f) Device 3 with 0.25 M, 0.75 M, and 1.0 M $MgSO_4$ aqueous electrolyte, respectively, for current I ranging between 2 and 6 mA and potential window $\Delta\psi_s = 1.6$ V as functions of dimensionless time t/t_{cd}.

discharging step for Device 2 [Figure 3.7(b)]. Furthermore, $\dot{Q}_{MnO_2}(t) - \bar{\dot{Q}}_{J,MnO_2}$ was strictly exothermic during the charging step and strictly endothermic during the discharging step for Device 3.

At the beginning of the charging step heat generation was attributed to the endothermic non-spontaneous Mg^{2+} desorption quickly dominated by the exothermic Mg^{2+} ion solvation. Indeed, Mg^{2+} cations get completely desolvated upon fast surface redox reaction of Mg^{2+} at the α-MnO_2 and solvation shell is then reformed upon their desorption. This was consistent with desolvation/solvation upon cation intercalation/deintercalation observed for $Na_{0.44}MnO_2$ electrodes in 1 M NaCl aqueous electrolyte under potential window of $\psi_{min} = -0.2$ V and $\psi_{max} = 0.6$ V vs. Ag^+/AgCl reference electrode [132]. As the charging progressed, the heat generation rate remained exothermic due to SO_4^{2-} adsorption. Here, no desolvation of SO_4^{2-} anions occurred as the solvated size of SO_4^{2-} anions of 1.17 nm was smaller than the size of mesopores (≤ 2 nm) in α-MnO_2 [109]. Then, at the beginning of the discharging step the heat generation rate decreased rapidly, however, it remained positive. This was attributed to the SO_4^{2-} desorption. Finally, towards the end of the discharging step the heat generation rate increased slightly due to the exothermic spontaneous Mg^{2+} surface redox reaction. However, as Mg^{2+} cations participated in surface redox reaction they first underwent endothermic desolvation [132].

In addition, Figures 3.7(d)-3.7(f) show the instantaneous heat generation rate at the α-MnO_2 electrode with subtracted Joule heating scaled with current $(\dot{Q}_{MnO_2}(t) - \bar{\dot{Q}}_{J,MnO_2})/I$ vs t/t_{cd} for the same range of current I and potential window $\Delta\psi_s$ for (d) Device 1, (e) Device 2, and (f) Device 3. Here also, the curves practically collapsed on top of each other for all devices. At the beginning of the charging step the diffusion limitations caused the curves to deviate slightly from each other. Indeed, the diffusion limitations were more pronounced for lower $MgSO_4$ concentrations and decreased as the $MgSO_4$ concentration increased. As the charging progressed the diffusion limitations were less pronounced and the curves approached each other. Finally, throughout the entire discharging step the curves collapsed on top of each other. This established that $\dot{Q}_{MnO_2}(t) - \bar{\dot{Q}}_{J,MnO_2}$ also scaled linearly with current I.

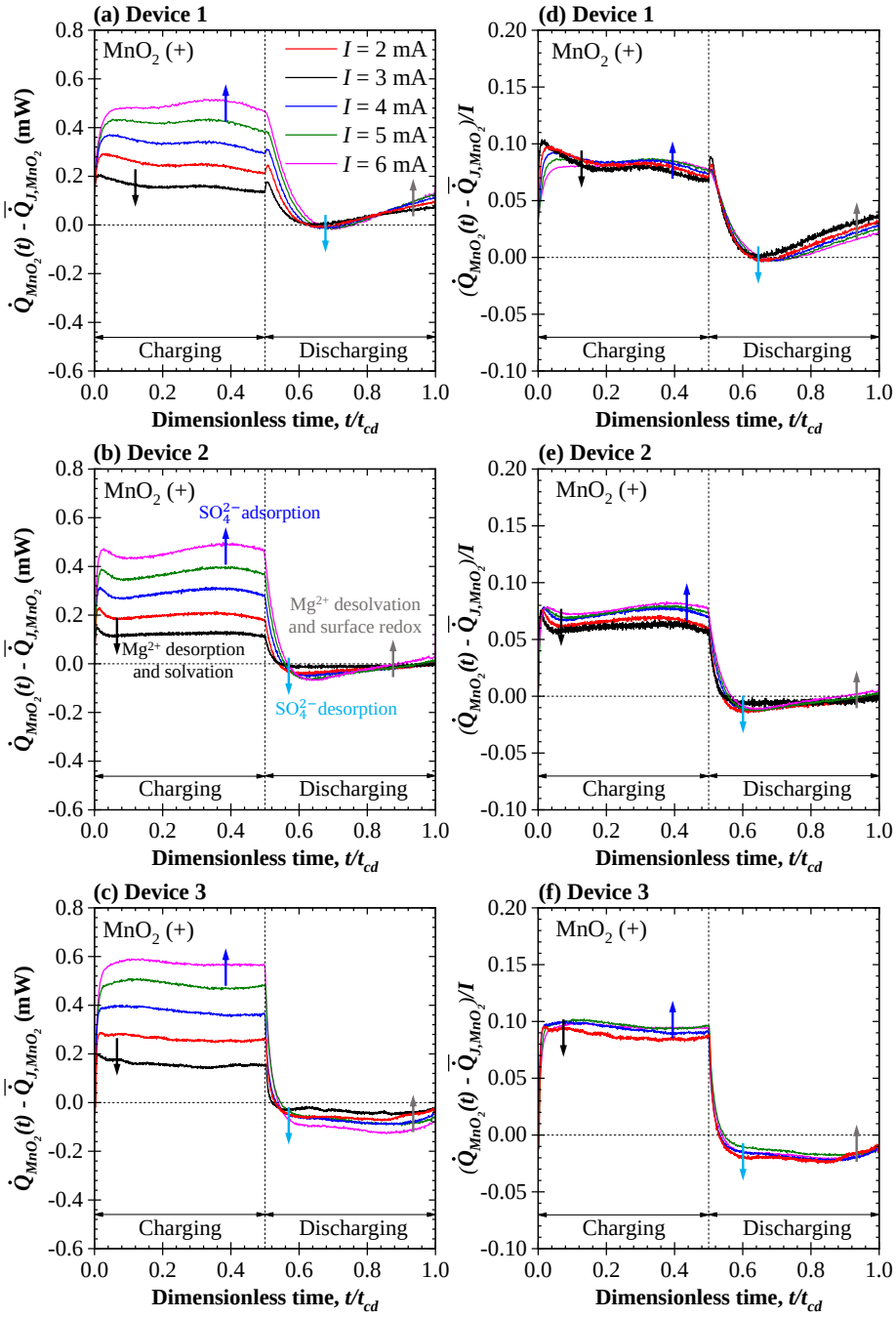

Figure 3.7: The instantaneous heat generation rate at the α-MnO_2 electrode with subtracted Joule heating $\dot{Q}_{MnO_2}(t) - \bar{\dot{Q}}_{J,MnO_2}$ for (a) Device 1, (b) Device 2, and (c) Device 3 and the instantaneous heat generation rate with subtracted Joule heating at the α-MnO_2 electrode scaled with current $(\dot{Q}_{MnO_2}(t) - \bar{\dot{Q}}_{J,MnO_2})/I$ for (d) Device 1, (e) Device 2, and (f) Device 3 with 0.25 M, 0.75 M, and 1.0 M $MgSO_4$ aqueous electrolyte, respectively, for current I ranging between 2 and 6 mA as functions of dimensionless time t/t_{cd}.

3.4.4 Thermal modeling

The instantaneous heat generation rate $\dot{Q}_{T,i}(t)$ at electrode "i" (i = AC or MnO_2) and its individual contributions were estimated from Equations (3.8) and (3.10) (see Figure S3 in Supplementary Material for contributions of individual terms individual). Figure 3.8(a)-3.8(c) shows the estimated (a) $\dot{Q}_{T,AC}(t)$, (b) $\dot{Q}_{rev,AC}(t) = \dot{Q}_{T,AC}(t) - \dot{Q}_{J,AC}(t)$, and (c) $\dot{Q}_{rev,AC}(t)/I$ at the AC electrode as functions of dimensionless time t/t_{cd} for current I ranging between 2 and 6 mA in aqueous $MgSO_4$ electrolyte. Moreover, Figure 3.8(d)-3.8(f) shows the estimated (d) $\dot{Q}_{T,MnO_2}(t)$, (e) $\dot{Q}_{T,MnO_2}(t) - \dot{Q}_{J,MnO_2}(t)$, and (f) $\dot{Q}_{T,MnO_2}(t) - \dot{Q}_{J,MnO_2}(t)/I$ at the α-MnO_2 electrode vs. t/t_{cd} for the same range of current I. The trends observed in $\dot{Q}_{T,AC}(t)$, $\dot{Q}_{rev,AC}(t)$, $\dot{Q}_{T,MnO_2}(t)$, and $\dot{Q}_{T,MnO_2}(t) - \dot{Q}_{J,MnO_2}(t)$ qualitatively matched those measured in the investigated devices. Moreover, $\dot{Q}_{rev,AC}(t)/I$ and $\dot{Q}_{T,MnO_2}(t) - \dot{Q}_{J,MnO_2}(t)/I$ were independent of current which was consistent with previous studies [75, 77, 93]. Finally, $\dot{Q}_{T,AC}(t)$ and $\dot{Q}_{T,MnO_2}(t)$ were also estimated for aqueous Cs_2SO_4 electrolyte with smaller solvation enthalpy $\Delta H_{sol}^{Cs} = -264$ kJ/mol (see Figure S3 in Supplementary Material). Here, only the magnitude of $\dot{Q}_{sol,MnO_2}(t)$ decreased while the other heat generation rate contributions remained the same as for aqueous $MgSO_4$ electrolyte. Predictions of the instantaneous heat generation rate $\dot{Q}_{T,MnO_2}(t)$ at the α-MnO_2 electrode featured large oscillation in heat generation rate indicating that the thermal signature of redox reactions and EDL formation dominated over that of solvation/desolvation.

3.5 Conclusion

The present study measured the instantaneous heat generation rates in hybrid supercapacitors with (i) 0.25 M, (ii) 0.75 M, and (iii) 1.0 M aqueous $MgSO_4$ electrolytes with pH of 7.21, 7.27, and 7.34, respectively. Moreover, this study identified, for the first time, the thermal signature of ion desolvation and solvation during cycling which is otherwise often dominated by that of ion adsorption and desorption. The investigated devices consisted of a positive α-MnO_2 cryptomelane electrode and an AC counter electrode separated by a polypropylene mesh impregnated with the electrolyte. The instantaneous heat generation rates were

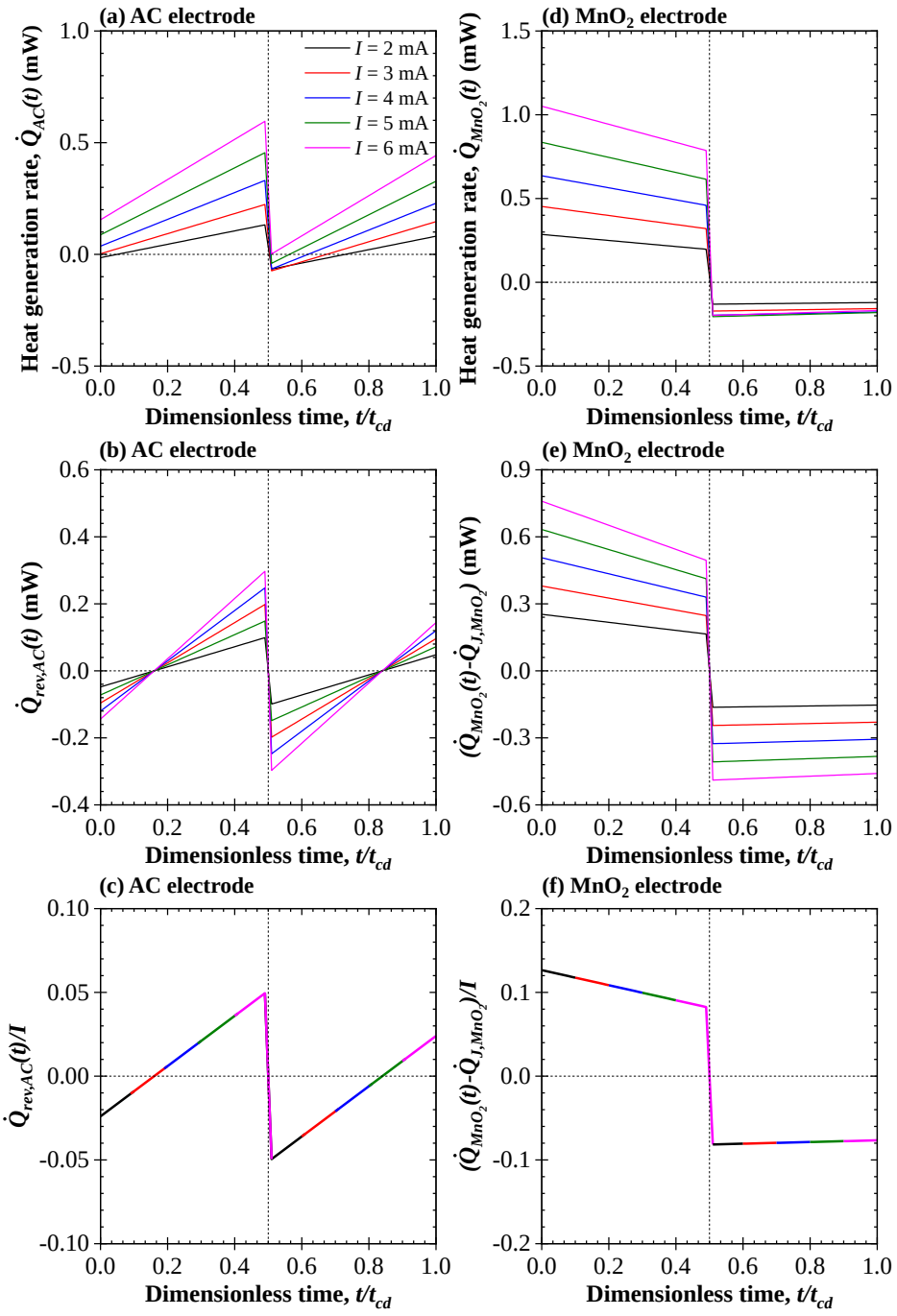

Figure 3.8: The estimated (a) $\dot{Q}_{T,AC}(t)$, (b) $\dot{Q}_{rev,AC}(t) = \dot{Q}_{T,AC}(t) - \dot{Q}_{J,AC}(t)$, and (c) $\dot{Q}_{rev,AC}(t)/I$ at the AC electrode and (d)$\dot{Q}_{T,MnO_2}(t)$, (e) $\dot{Q}_{T,MnO_2}(t) - \dot{Q}_{J,MnO_2}(t)$, and (f) $\dot{Q}_{T,MnO_2}(t) - \dot{Q}_{J,MnO_2}(t)/I$ at the α-MnO_2 electrode for current I ranging between 2 and 6 mA in aqueous $MgSO_4$ electrolyte.

measured at each electrode separately in a custom made isothermal *operando* calorimeter under galvanostatic conditions, potential window of 1.6 V, and temperature of 20 °C. The heat generation rate at the AC electrodes featured large oscillations which were attributed to EDL formation and dissolution of SO_4^{2-} anions and Mg^{2+} cations. Interestingly, SO_4^{2-} adsorption was accompanied by their partial desolvation in the small pores of the AC electrode due to the large solvated ion size. Conversely, the partially desolvated SO_4^{2-} anions became fully solvated upon desorption. By contrast, Mg^{2+} cations were not desolvated upon adsorption due to their small solvated ion size. On the other hand, the heat generation rate at the α-MnO_2 electrodes was strictly positive during galvanostatic cycling. When the previously intercalated Mg^{2+} ions were desorbed at the α-MnO_2 electrode they quickly became solvated. It was found that the thermal signature of their large solvation enthalpy dominated over the thermal signature of desorption during charging step. Conversely, Mg^{2+} were fully stripped of their solvation shell during fast surface redox reaction resulting in a rapid decrease in heat generation during discharging step. Moreover, it was found that after subtracting Joule heating the remaining heat generation rate scaled linearly with imposed current at both electrodes. Finally, the heat generation rate was predicted using a thermal model which accounted for reversible heat generation due to EDL formation, redox reactions, and ion solvation/desolvation. In addition, it also accounted for Joule heating and irreversible heat generation due to redox reactions. The results qualitatively matched the measured heat generation rates in the investigated devices. Moreover, the heat generation rates scaled linearly with current after Joule heating was subtracted.

CHAPTER 4

Calorimetric characterization of the effect of ions on α-MnO_2 charging mechanisms

This chapter investigates the thermal signature of the charging mechanisms of three hybrid supercapacitors with aqueous electrolytes using isothermal *operando* calorimetry. They consisted of a positive $\alpha-MnO_2$ cryptomelane electrode and a negative activated carbon (AC) electrode. They were assembled in (i) 0.5 M Li_2SO_4, (ii) 0.5 M Na_2SO_4, or (iii) 0.5 M Cs_2SO_4 aqueous electrolytes. The devices were characterized under cyclic voltammetry, galvanostatic cycling, and electrochemical impedance spectroscopy (EIS). Furthermore, during galvanostatic cycling, the instantaneous heat generation rates were measured at each electrode separately. The thermal signatures measured at the negative AC electrodes were qualitatively similar except for the device with 0.5 M Li_2SO_4. During charging, the features were attributed to the initial endothermic anion desorption and solvation followed by the exothermic electric double layer (EDL) formation of cations, except for Li^+ which possibly participated in surface redox reactions at the AC electrode due to its smaller size and high electronegativity. Similarly, the thermal signature measured at the positive $\alpha-MnO_2$ electrode was attributed to cations participating in fast surface redox reaction and desolvation/solvation or anions undergoing adsorption/desorption. Moreover, for Li^+ cations with a larger solvated ion size, an endothermic dip attributed to hydrolysis was observed at the positive $\alpha-MnO_2$ electrode towards the end of the charging step already at 1.6 V. Finally, the study demonstrated the importance of complementing the electrochemical measurements with calorimetric measurements in characterizing electrode materials to provide unique insight into the physical and chemical processes occurring in hybrid supercapacitors.

4.1 Materials and methods

4.1.1 Electrode fabrication and device assembly

The fabrication method and device assembly was discussed in detail in Chapter 6 and need not be repeated. In brief, slurries were prepared by mixing together the active material, carbon black (Superior Graphite), and polyvinylidene fluoride (PVDF, Solef® 5130) binder in a 70:15:15 weight ratio. The PVDF solution was prepared by dissolving PVDF powder in liquid dimethylacetamide (DMA) in an 8.5:91.5 weight ratio. The active materials were $\alpha-MnO_2$ (Prince Erachem) or activated carbon (YP-50F, Kuraray Chemical). To ensure homogeneously mixed slurries, the dry matter content was adjusted to 25.3 wt.% and 18.7 wt.% for the $\alpha-MnO_2$ and AC slurries, respectively, by adding dimethylacetamide (DMA). Then the mixtures were vigorously stirred in a beaker with a magnetic stirrer overnight.

Second, the slurries were drop cast onto titanium (Ti) mesh current collector sheets (Dexmet Corp.) with a 1 × 1 cm^2 footprint area and spread evenly with a spatula. The current collectors had been previously treated in a boiling aqueous solution containing 10 wt.% of oxalic acid and then rinsed off with DI water. This enhanced the adhesion between the slurries and current collectors. The electrodes were then dried in an oven at 60 °C for 12 h. Immediately after, each electrode was hot-roll calendered to ensure the uniform thickness of each electrode. This resulted in a mass loading varying between 6.5 and 7.5 mg/cm^2 for the $\alpha-MnO_2$ electrodes and between 4 and 8 mg for the AC electrodes.

Finally, the devices were assembled with a positive $\alpha-MnO_2$ electrode and a negative AC electrode separated by a 1 mm-thick, chemically inert polypropylene mesh. The mesh prevented the electrodes from coming into contact with one another while allowing the ions to pass through it freely. The separator was impregnated with, (a) 0.5 M Li_2SO_4 (Device 1), (b) 0.5 M Na_2SO_4 (Device 2), or (c) 0.5 M Cs_2SO_4 (Device 3) aqueous electrolytes. Table 4.1 summarizes the mass loading of active material in each electrode and the electrolyte properties used to interpret the results.

Table 4.1: Electrode mass loading and electrolyte properties of hybrid supercapacitor Devices 1 to 3.

Property/parameter	**Device 1**	**Device 2**	**Device 3**
Aqueous electrolyte - 0.5 M concentration	Li_2SO_4	Na_2SO_4	Cs_2SO_4
Active mass loading of MnO_2, m_{MnO_2} (mg)	6.72	6.65	7.28
Active mass loading of AC, m_{AC} (mg)	6.92	6.67	4.17
Cation diameter, a_+ (nm) [110]	0.136	0.190	0.334
Solvated cation diameter, $a_{+,s}$ (nm) [111]	0.410	0.360	0.346
Anion diameter, a_- (nm) [113]	0.484	0.484	0.484
Solvated anion diameter, $a_{-,s}$ (nm) [113]	1.173	1.173	1.173
Diffusion coefficient of cations, $D_+ \times 10^9$ (m^2/s) [114]	1.232	1.341	2.076
Diffusion coefficient of anions, $D_- \times 10^9$ (m^2/s) [115]	0.809	0.809	0.809
Cation hydration enthalpy, $\Delta H_{sol,+}$ (kJ/mol) [116]	-519	-409	-264
Anion hydration enthalpy, $\Delta H_{sol,-}$ (kJ/mol) [116]	-1059	-1059	-1059

4.1.2 Device characterization

First, either the positive $\alpha-MnO_2$ or the negative AC working electrodes were cycled in a three-electrode setup with 0.5 M Li_2SO_4, 0.5 M Na_2SO_4, or 0.5 M Cs_2SO_4 aqueous electrolytes. Here, elemental Ni plate was used as a counter electrode and $Ag^+/AgCl_{(s)}$ was the reference electrode (Fisherbrand^{TM} accumet^{TM}). Cyclic voltammetry was used at scan rate ν of 10 mV/s for 95 cycles and then at scan rate ν of 5 mV/s for the last 5 cycles. The potential window was between $\psi_{min} = 0$ V and $\psi_{max} = 0.8$ V for the $\alpha-MnO_2$ electrodes and between $\psi_{min} = -0.8$ V and $\psi_{max} = 0$ V for the AC electrodes. The measured cyclic voltammograms were used to compute the capacity of each electrode thus ensuring that the capacity of the paired $\alpha-MnO_2$ and AC electrodes matched.

Then, CV measurements were performed on the three assembled devices (Table 4.1) in the isothermal *operando* calorimeter at a temperature of 20 °C and at five different scan rates ν ranging between 5 and 50 mV/s and 20 cycles each. Here, the cell potential window $\Delta\psi_s$ ranged between $\psi_{s,min} = 0$ V and $\psi_{s,max} = 1.6$ V. The integral capacity $C(\nu)$ (in C) was computed as a function of scan rate ν according to [82]

$$C(\nu) = \oint \frac{I(\psi_s)}{2\nu} \mathrm{d}\psi_s, \tag{4.1}$$

where $I(\psi_s)$ was the measured current response at the time-dependent cell potential ψ_s. Moreover, the gravimetric capacity $C_g(\nu)$ (in mAh/g) was defined as

$$C_g(\nu) = \frac{C(\nu)}{m}, \tag{4.2}$$

where m was the total mass loading (in g) of active materials in both $\alpha-\mathrm{MnO_2}$ and AC electrodes.

Lastly, galvanostatic cycling with isothermal *operando* calorimetry was performed on the devices for five currents I ranging between 2 and 6 mA and cell potential window $\Delta\psi_s$ of 1.6 V versus AC electrode, consecutively. For each current I, 30 consecutive cycles were performed ensuring that oscillatory steady state has been reached.

Potential vs. time curves were then used to compute the internal resistance of the device R_s via the IR drop observed at the transition between the charging and discharging steps as [1, 78–80],

$$R_s(I) = \frac{\psi_s(t_c^+) - \psi_s(t_c^-)}{2I}. \tag{4.3}$$

Here, the potential $\psi_s(t_c^+)$ was taken immediately at the current switch while the potential $\psi_s(t_c^-)$ was the potential 10 ms after the current switch, for all devices, (i.e., $t_c^+ - t_c^- = 10$ ms), as recommended by Ref. [79].

4.1.3 Isothermal *operando* calorimeter

The instantaneous heat generation rate $\dot{Q}_i(t)$ (in mW) at each electrode i (i = MnO_2 or AC) in Devices 1 to 3 was obtained by measuring the electric potential $\Delta V_i(t)$ across a thermoelectric heat flux sensor in thermal contact with the electrode during galvanostatic cycling based on [99],

$$\dot{Q}_i = q_i''(t) A_i = \frac{\Delta V_i(t)}{S_i} A_i, \tag{4.4}$$

Here, S_i was the temperature dependent sensitivity (in μV/(W/m^2)) of the heat flux sensor in thermal contact with electrode i and was provided by the manufacturer while A_i denoted the footprint area of the electrode (1 cm^2). Then the heat flux $q_i''(t)$ was computed according to Equation (4.4). Furthermore, in an effort to reduce the noise in the measurements, the measured heat generation rates were averaged at the same temporal point in each of the last five cycles at current I as

$$\dot{Q}_i(t/t_{cd}) = \frac{1}{5} \sum_{j=26}^{30} \dot{Q}_i(t/t_{cd} + (j-1)), \tag{4.5}$$

where t/t_{cd} was the dimensionless time within one cycle (i.e., t/t_{cd} was confined between 0 and 1) and j was the cycle number (j = 26 to 30).

Finally, the measured instantaneous heat generation rate $\dot{Q}_i(t)$ can be decomposed as a sum of its reversible and irreversible contributions such that $\dot{Q}_i(t) = \dot{Q}_{rev,i}(t) + \dot{Q}_{irr,i}(t)$ [61,99,101]. In addition, the time average of the reversible heat generation rate $\dot{Q}_{rev,i}(t)$ over the entire charging/discharging cycle is, by definition, zero. Therefore, the irreversible heat generation rate $\bar{\dot{Q}}_{irr,i}$ over the entire cycle can be written as [61, 99, 101],

$$\bar{\dot{Q}}_{irr,i} = \frac{1}{t_{cd}} \int_{(n_c-1)t_{cd}}^{n_c t_{cd}} \dot{Q}_i(t)\, \mathrm{d}t. \tag{4.6}$$

Here, n_c referred to the cycle number large enough to ensure that the oscillatory steady state in heat generation rate was reached and t_{cd} was the time of a charge/discharge cycle independent of the cycle number at oscillatory steady state.

4.2 Results and discussion

4.2.1 Cyclic voltametry

4.2.1.1 Three-electrode cyclic voltammograms

Figure 4.1 shows the measured cyclic voltammograms at scan rate ν of 10 mV/s for the individual positive $\alpha-MnO_2$ and negative AC electrodes vs. $Ag^+/AgCl$ reference electrode paired in Devices 1, 2, and 3 with (a) 0.5 M Li_2SO_4, (b) 0.5 M Na_2SO_4, and (c) 0.5 M Cs_2SO_4 aqueous electrolytes, respectively. The capacity of each electrode was calculated from the cyclic voltammograms [Equation (4.1)]. In all devices, the paired positive and negative electrodes had similar capacities. The active mass loading of the AC electrodes in Devices 1 and 2 was more similar than that of Device 3 (Table 4.1) resulting in almost identical capacity. Moreover, the $\alpha-MnO_2$ electrodes exhibited an oxidation peak at the end of the positive sweep (i.e., Potential vs. $Ag^+/AgCl = 0.8$ V), and a reduction dip at the end of the negative sweep (i.e., Potential vs. $Ag^+/AgCl = 0$ V) in all electrolytes.

4.2.1.2 Full device cyclic voltammograms

Figure 4.2 shows the measured cyclic voltammograms of Devices 1 to 3 with (a) 0.5 M Li_2SO_4, (b) 0.5 M Na_2SO_4, and (c) 0.5 M Cs_2SO_4 aqueous electrolytes and scan rate ν ranging between 5 and 50 mV/s. The cell potential $\psi_s(t)$ was measured at the positive $\alpha-MnO_2$ electrode in reference to the negative AC electrode. The cell potential window $\Delta\psi_s = 1.6$ V exceeded the theoretical electrochemical stability window of water of 1.23 V at 20 °C. However, no rapid increase in the current nor bubble formation was observed in any of the devices which indicated the absence of hydrolysis [117, 118]. The cyclic voltammograms of Devices 1 and 2 changed from a rectangular shape at lower scan rates to a leaf-like shape at higher scan rates indicating diffusion limitations and resistive behavior. In Device 3, the resistive behavior was less pronounced than in Device 1 and 2 as scan rate ν increased. This can be attributed to a larger diffusion coefficient of Cs^+ cations than that of Li^+ and Na^+ cations resulting in a smaller electrical resistance of Device 3 compared to Devices 1 and 2.

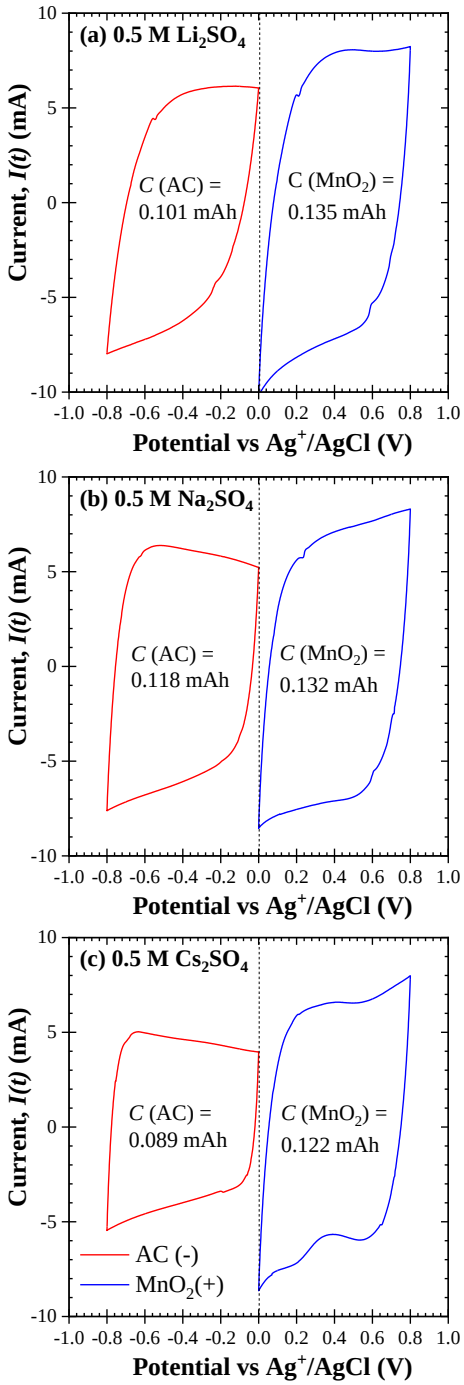

Figure 4.1: Cyclic voltammograms for AC and $\alpha-MnO_2$ cryptomelane electrodes including their capacity in (a) 0.5 M Li_2SO_4, (b) 0.5 M Na_2SO_4, and (c) 0.5 M Cs_2SO_4 aqueous electrolytes for scan rate $\nu = 10$ mV/s.

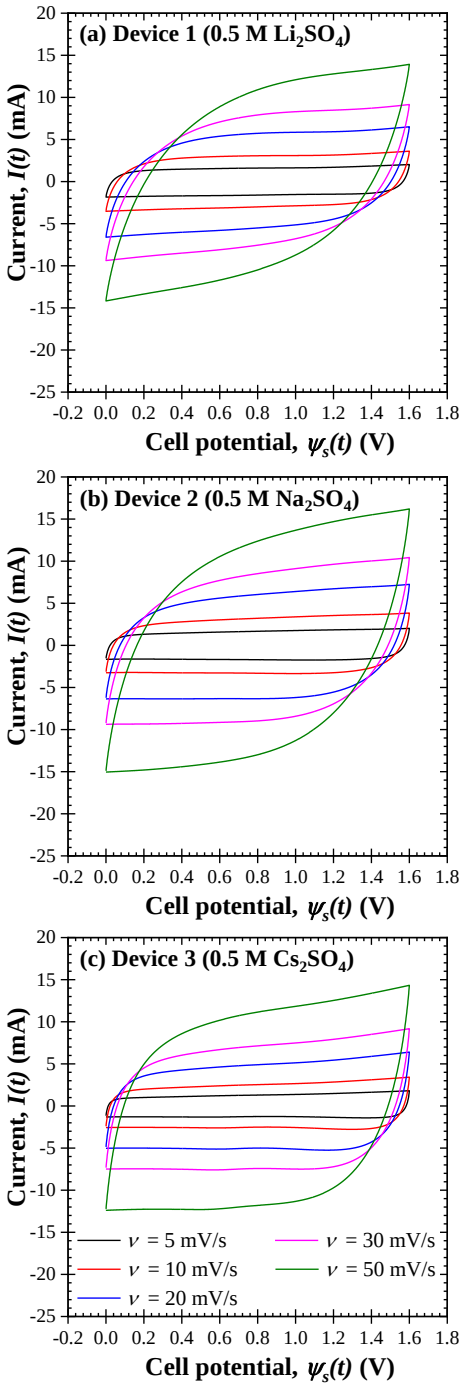

Figure 4.2: Cyclic voltammograms for (a) Device 1 with 0.5 M Li_2SO_4, (b) Device 2 with 0.5 M Na_2SO_4, and (c) Device 3 with 0.5 M Cs_2SO_4 aqueous electrolyte.

This was also the cause of a smaller current response of Devices 1 and 2 compared to Device 3.

4.2.2 Galvanostatic cycling

Figure 4.3 shows the temporal evolution of the cell potential $\psi_s(t)$ as a function of time under galvanostatic cycling for current I ranging between 2 and 6 mA and the potential window $\Delta\psi_s$ of 1.6 V for Devices 1 to 3 in (a) 0.5 M Li_2SO_4, (b) 0.5 M Na_2SO_4, and (c) 0.5 M Cs_2SO_4 aqueous electrolytes. The cell potential $\psi_s(t)$ practically varied linearly with time t excluding the IR drop at the beginning of the charging and discharging steps. Such behavior was also observed in EDLCs and hybrid supercapacitors featuring fast surface redox reactions [16, 76, 101, 102].

4.2.3 Capacity and resistance

Figures 4.4(a) and 4.4(b) show the capacity C and gravimetric capacity C_g per unit mass of both electrodes of the investigated devices as a function of the scan rate ν. Both C and C_g decreased with increasing scan rate ν, indicating diffusion limitations. Here, the capacity of devices decreased with decreasing cation diffusion coefficient for devices with similar mass loading (i.e., $D_{Na^+} > D_{Li^+}$). Interestingly, the capacity C of Device 3 (0.5 M Cs_2SO_4) was the lowest at lower scan rates ν, but it decreased slower than the capacity C of the other two devices as the scan rate ν increased. This was attributed to the lower mass loading of the electrodes used in Device 3, causing its resistance to be lower and delayed the diffusion limitations.

Moreover, Figure 4.4(c) shows the internal resistances R_s of each device computed according to Equation (4.3) for I ranging between 2 and 6 mA and such that the average internal resistances were $\bar{R}_s = 13.19 \pm 0.44\ \Omega$ for Device 1, $\bar{R}_s = 7.85 \pm 0.61\ \Omega$ for Device 2, and $\bar{R}_s = 6.82 \pm 0.91\ \Omega$ for Device 3. The internal resistance R_s was independent of current I for all devices. Finally, Figure 4.4(d) shows the Nyquist plots of the devices interpreted according to Ref. [89]. Here, the difference between the electrode resistance R_P and the internal resistance R_s was attributed to the electrolyte resistance. The internal resistance R_s obtained from the Nyquist plots was in good agreement with the internal resistance $\bar{R}_s$ obtained from the IR drop (i.e., $R_s \approx \bar{R}_s$ for all devices).

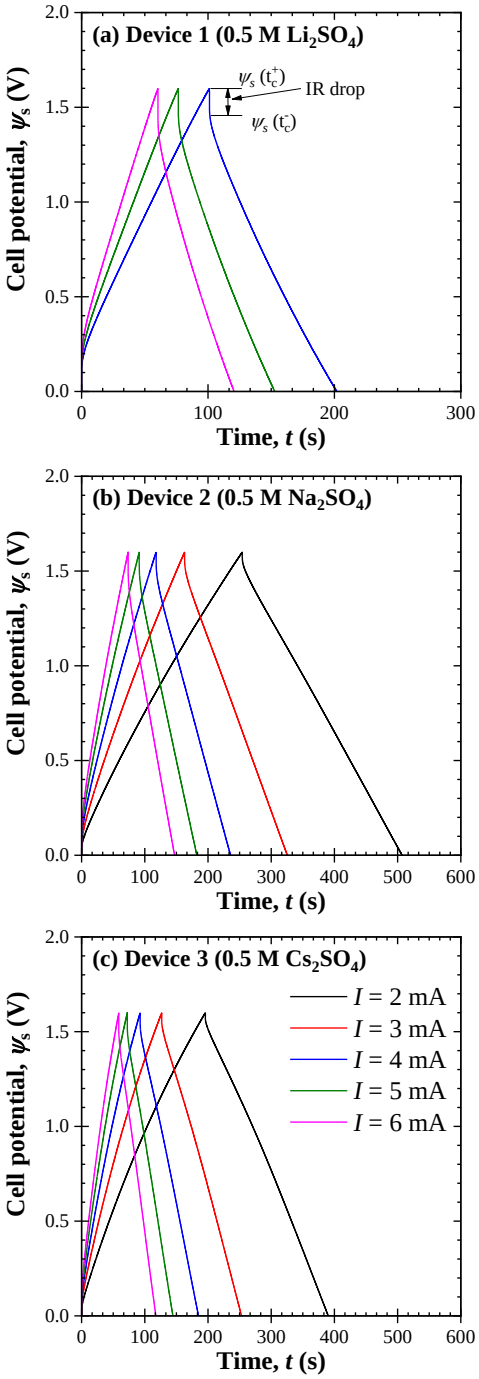

Figure 4.3: Temporal evolution of cell potential ψ_s during galvanostatic cycling for (a) Device 1 with 0.5 M Li_2SO_4, (b) Device 2 with 0.5 M Na_2SO_4, and (c) Device 3 with 0.5 M Cs_2SO_4 aqueous electrolyte for current I ranging between 2 and 6 mA and potential window $\Delta\psi_s$ of 1.6 V.

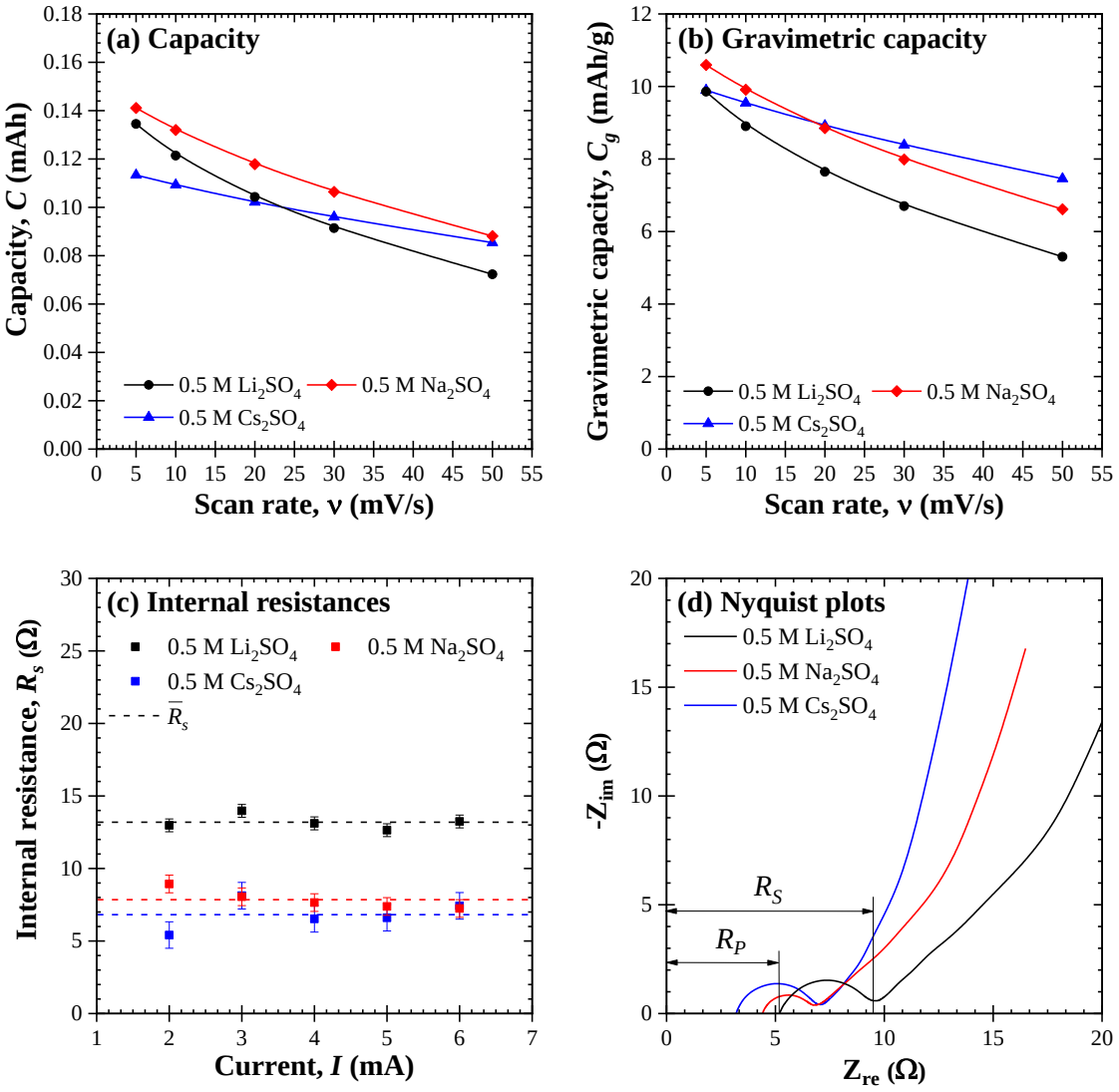

Figure 4.4: (a) Capacity $C(\nu)$ and (b) gravimetric capacity $C_g(\nu)$ per unit mass of both electrodes as a function of scan rate ν for full devices, (c) internal resistance computed from the IR drop as a function of current, and (d) Nyquist plots of the devices.

4.2.4 Instantaneous heat generation rate measurements

Figure 4.5 shows the instantaneous heat generation rate $\dot{Q}_i(t)$ as a function of dimensionless time t/t_{cd} for both the positive $\alpha-MnO_2$ electrode and the negative AC electrode for the

last five consecutive cycles under galvanostatic cycling subjected to the imposed current I of 5 mA and the potential window $\Delta\psi_s$ of 1.6 V for Devices 1 to 3 with (a) 0.5 M Li_2SO_4, (b) 0.5 M Na_2SO_4, and (c) 0.5 M Cs_2SO_4 aqueous electrolytes. The instantaneous heat generation rates $\dot{Q}_{MnO_2}(t)$ and $\dot{Q}_{AC}(t)$ were repeatable from cycle to cycle for all devices and all currents I. To clarify the origin of the thermal signatures, $\dot{Q}_i(t)$ was averaged over the last five consecutive cycles according to Equation (4.5). Moreover, the time-average of the instantaneous heat generation rate $\dot{Q}_i$ over the entire cycle computed at each electrode according to Equation (4.6) yields the irreversible heat generation rate $\bar{\dot{Q}}_{irr,i}$ shown as dashed line in Figures 4.5(a) − 4.5(c).

Figure 4.6 shows the irreversible heat generation rate $\bar{\dot{Q}}_{irr,i}$ as a function of the square of the current I^2 for all investigated devices. The irreversible heat generation rate at the AC electrode $\bar{\dot{Q}}_{irr,AC}$ was found to be linearly proportional to I^2. This indicates that the irreversible heat generation rate at the AC electrode was due to Joule heating only. These findings were in agreement with previous calorimetric studies of EDLC devices [24, 61, 98, 100, 105, 135] as well as with numerical predictions for AC electrodes in EDLCs [75] and hybrid supercapacitors [77]. Moreover, Figure 4.6 establishes that the total irreversible heat generation over the entire charge/discharge cycle, $\bar{\dot{Q}}_{irr,T} = \bar{\dot{Q}}_{irr,MnO_2} + \bar{\dot{Q}}_{irr,AC}$, exceeded Joule heating, $\bar{\dot{Q}}_J = \bar{R}_s I^2$ predicted from the internal resistance $\bar{R}_s$ of the entire device. Finally, the slope of the linear fit can be interpreted as the resistance, through which the current passes. Subtracting the resistance of the AC half-cell from the total internal resistance $\bar{R}_s$ of the device obtained from the IR drop yields the resistance of the $\alpha-MnO_2$ half-cell as

$$R_{MnO_2} = \bar{R}_s - R_{AC}. \tag{4.7}$$

These resistances were used to compute the Joule heating associated with each half-cell as $\bar{\dot{Q}}_J = R_i I^2$.

Figure 4.7 shows the instantaneous heat generation rate at the negative AC electrodes $\dot{Q}_{AC}(t)$ for (a) Device 1 with 0.5 M Li_2SO_4, (b) Device 2 with 0.5 M Na_2SO_4, and (c) Device 3 with 0.5 M Cs_2SO_4 aqueous electrolytes and the instantaneous heat generation rate at the

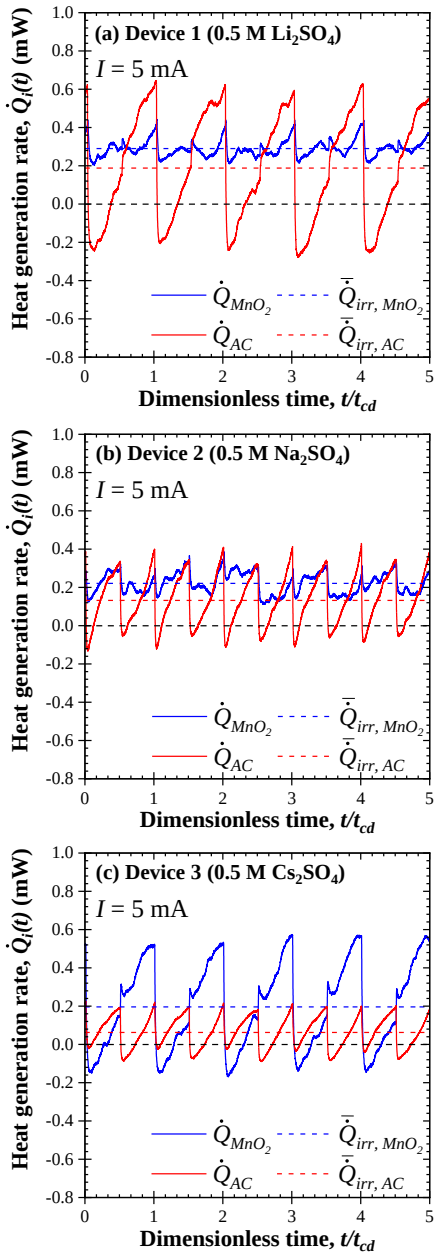

Figure 4.5: Instantaneous heat generation rate $\dot{Q}_i(t)$ as a function of dimensionless time t/t_{cd} measured at both the positive $\alpha-MnO_2$ electrode and the negative AC electrode for the last five consecutive cycles and the imposed current I of 5 mA and potential window of $\Delta\psi_s$ of 1.6 V for (a) Device 1 with 0.5 M Li_2SO_4, (b) Device 2 with 0.5 M Na_2SO_4, and (c) Device 3 with 0.5 M Cs_2SO_4 aqueous electrolyte.

AC electrode $\dot{Q}_{AC}(t)$ with subtracted Joule heating $\bar{\dot{Q}}_{J,AC}$ for (d) Device 1 with 0.5 M Li_2SO_4, (e) Device 2 with 0.5 M Na_2SO_4, and (f) Device 3 with 0.5 M Cs_2SO_4 aqueous electrolytes

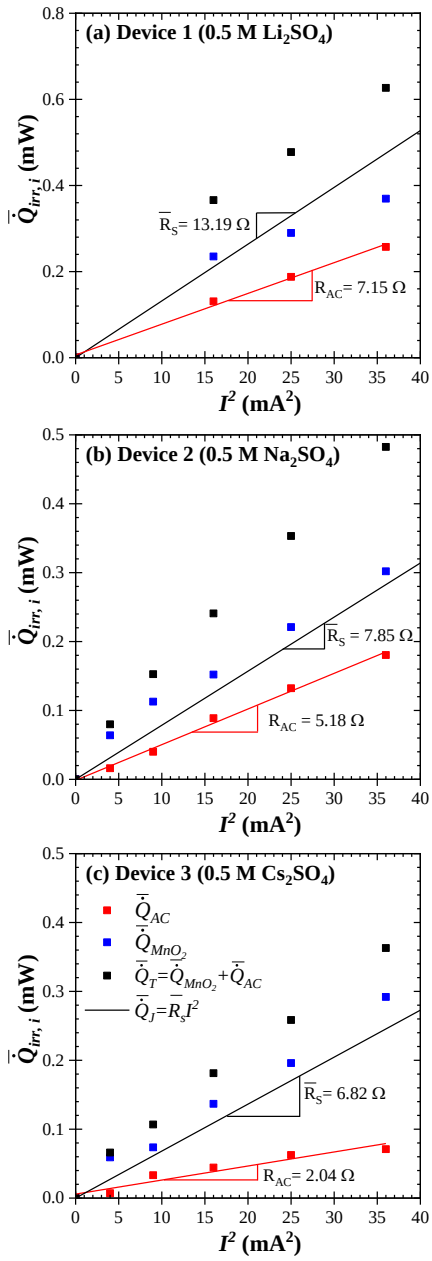

Figure 4.6: Average irreversible heat generation rate $\bar{\dot{Q}}_{irr,i}$ as a function of current squared for both the AC and $\alpha-MnO_2$ electrodes for (a) Device 1 with 0.5 M Li_2SO_4, (b) Device 2 with 0.5 M Na_2SO_4, and (c) Device 3 with 0.5 M Cs_2SO_4 aqueous electrolytes.

as functions of dimensionless time t/t_{cd} and potential window $\Delta\psi_s = 1.6$ V, and current I ranging between 2 and 6 mA. For all devices, at the beginning of the charging step, there was an endothermic dip dominated by the initial SO_4^{2-} anion desorption [24,135]. After the

initial endothermic dip, the SO_4^{2-} anion desorption grew weaker and the exothermic cation (Na^+, Cs^+) adsorption or possibly surface redox reactions (Li^+) dominated for the rest of the charging step [24, 135]. Moreover, at the beginning of the discharging step, an endothermic dip was observed for Devices 2 and 3, as well as for lower currents in Device 2 (i.e., $I = 2$ and 3 mA). This endothermic dip was attributed to the endothermic desorption of cations. In Device 3 the endothermic dip was less visible due to the slower nature of possible Li^+ redox desorption compared to SO_2^{2-} adsorption. This behavior was only present in Device 1, as Li^+ cations were the only cations that could participate in surface redox reactions at the AC electrode. As the discharging progressed, instantaneous heat generation rate became dominated by the exothermic SO_4^{2-} adsorption. Similar results have been reported for calorimetric measurements at the AC electrodes in EDLC [61, 98, 100, 105, 135] and in hybrid supercapacitor [24] devices.

Figure 4.8 shows the instantaneous heat generation rate at the positive MnO_2 electrodes $\dot{Q}_{MnO_2}(t)$ for (a) Device 1 with 0.5 M Li_2SO_4, (b) Device 2 with 0.5 M Na_2SO_4, and (c) Device 3 with 0.5 M Cs_2SO_4 aqueous electrolytes and the instantaneous heat generation rate at the AC electrode $\dot{Q}_{MnO_2}(t)$ with subtracted Joule heating $\bar{\dot{Q}}_J$ for (d) Device 1 with 0.5 M Li_2SO_4, (e) Device 2 with 0.5 M Na_2SO_4, and (f) Device 3 with 0.5 M Cs_2SO_4 aqueous electrolytes as functions of dimensionless time t/t_{cd} and potential window $\Delta\psi_s = 1.6$ V, and current I ranging between 2 and 6 mA. An endothermic dip appeared at the beginning of the charging and was associated with the endothermic cation (Li^+, Na^+, Cs^+) redox desorption based on similar findings for MnO_2-birnnesite pseudocapacitive electrodes in 1 M $LiClO_4$ in 1:1 EC:DMC and MoO_2-rGO in 0.5 M Na_2SO_4 [24]. As the charging progressed, the cation desorption decreased and the exothermic SO_4^{2-} adsorption and EDL formation dominated for the rest of the step. This manifested as a slow increase in the measured heat generation rate for all devices. Device 1 [Figures 4.8(a) and 4.8(d)] exhibited a second endothermic dip towards the end of the charging step attributed to the hydrolysis reaction. It was attributed to hydrolysis as (i) the dip was endothermic as is hydrolysis reaction [122, 123], (ii) the dip appeared towards the end of charging when the cell potential exceeded the electrochemical stability window of water of 1.23 V at 20 °C, and (iii) it was independent

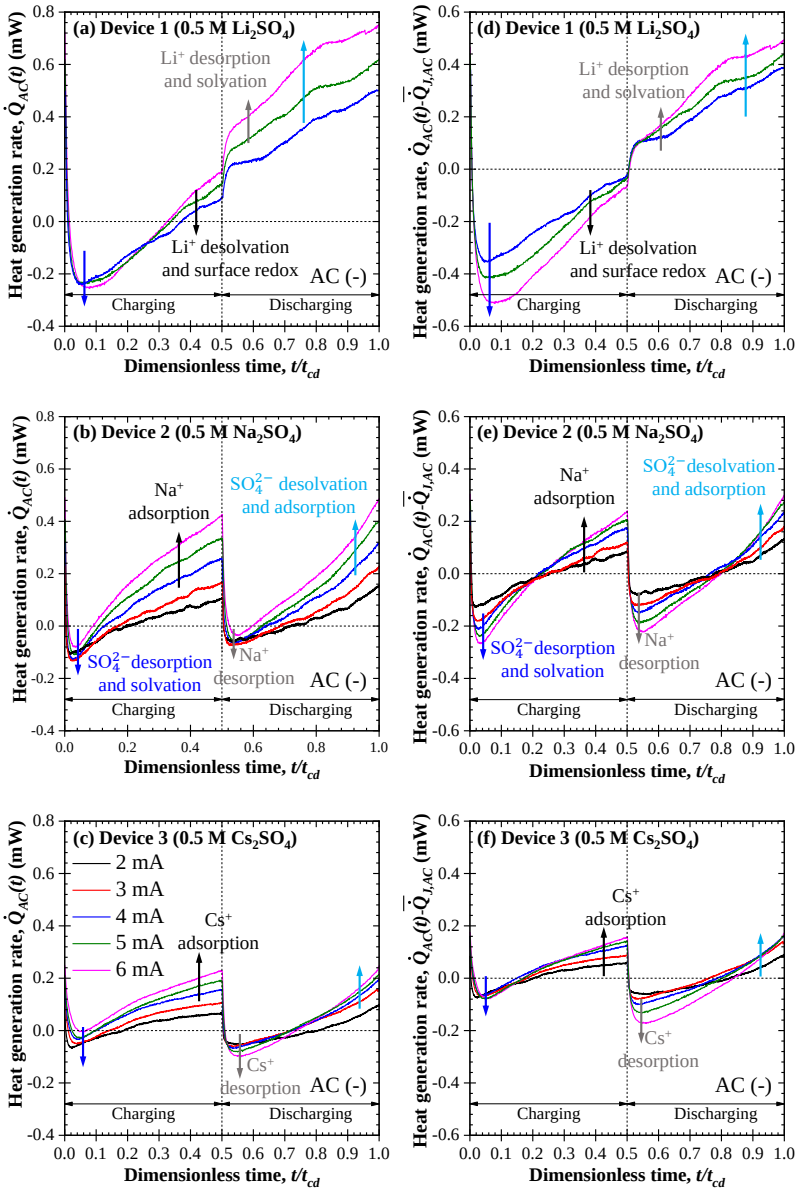

Figure 4.7: Instantaneous heat generation rate at the negative AC electrodes $\dot{Q}_{AC}(t)$ for (a) Device 1 with 0.5 M Li_2SO_4, (b) Device 2 with 0.5 M Na_2SO_4, and (c) Device 3 with 0.5 M Cs_2SO_4 aqueous electrolytes and the instantaneous heat generation rate at the AC electrode $\dot{Q}_{AC}(t)$ with subtracted Joule heating $\bar{\dot{Q}}_J$ for (d) Device 1 with 0.5 M Li_2SO_4, (e) Device 2 with 0.5 M Na_2SO_4, and (f) Device 3 with 0.5 M Cs_2SO_4 aqueous electrolytes as functions of dimensionless time t/t_{cd} and potential window $\Delta\psi_s = 1.6$ V, and current I ranging between 2 and 6 mA.

of current. Interestingly, hydrolysis was not evident in Device 2 [Figures 4.8(b) and 4.8(e)] due to a thinner solvation shell surrounding the Na^+ cations compared to Li^+ cations [111]. Hydrolysis was not observed in Device 3 either for the same reasons.

Furthermore, in the beginning of the discharging step, a sharp exothermic peak was observed for all devices and was associated with an overpotential lag [76, 77]. Such behavior has been previously observed both numerically [77] as well as experimentally [98]. After the initial spike, an endothermic dip associated with the continued endothermic SO_4^{2-} anion desorption appeared. Finally, towards the end of the discharging step, the exothermic spontaneous cation (Li^+, Na^+, Cs^+) surface redox began to dominate the thermal signature. This resulted in a slow increase in the instantaneous heat generation rate.

4.3 Conclusion

The study reported the instantaneous heat generation rates measured at the positive $\alpha-MnO_2$ and the negative AC electrodes of hybrid supercapacitors. The electrodes were immersed in (a) 0.5 M Li_2SO_4, (b) 0.5 M Na_2SO_4, or (c) 0.5 M Cs_2SO_4 aqueous electrolytes. First, their capacity, gravimetric capacity and internal resistance were obtained from cyclic voltammetry, galvanostatic cycling, and electrochemical impedance spectroscopy. Capacity and gravimetric capacity decreased with increasing scan rate ν for all devices. Moreover, the gravimetric capacity increased with increasing diffusion coefficient of cations. The internal resistance computed from the IR drop was in good agreement with that obtained from EIS measurements and was independent of current. In addition, isothermal *operando* calorimetry was performed during galvanostatic cycling for the potential window $\Delta\psi_s$ of 1.6 V. The instantaneous heat generation rate measurements were repeatable from cycle to cycle at both electrodes for all investigated devices. Furthermore, the large variations in heat generation rates observed at both electrodes during cycling of the devices were caused by reversible processes such as ion adsorption/desorption at the AC electrode and surface redox at the $\alpha-MnO_2$ electrode. The observed endothermic features at AC or $\alpha-MnO_2$ electrodes were attributed either to anion or cation desorption during charging, respectively. The observed

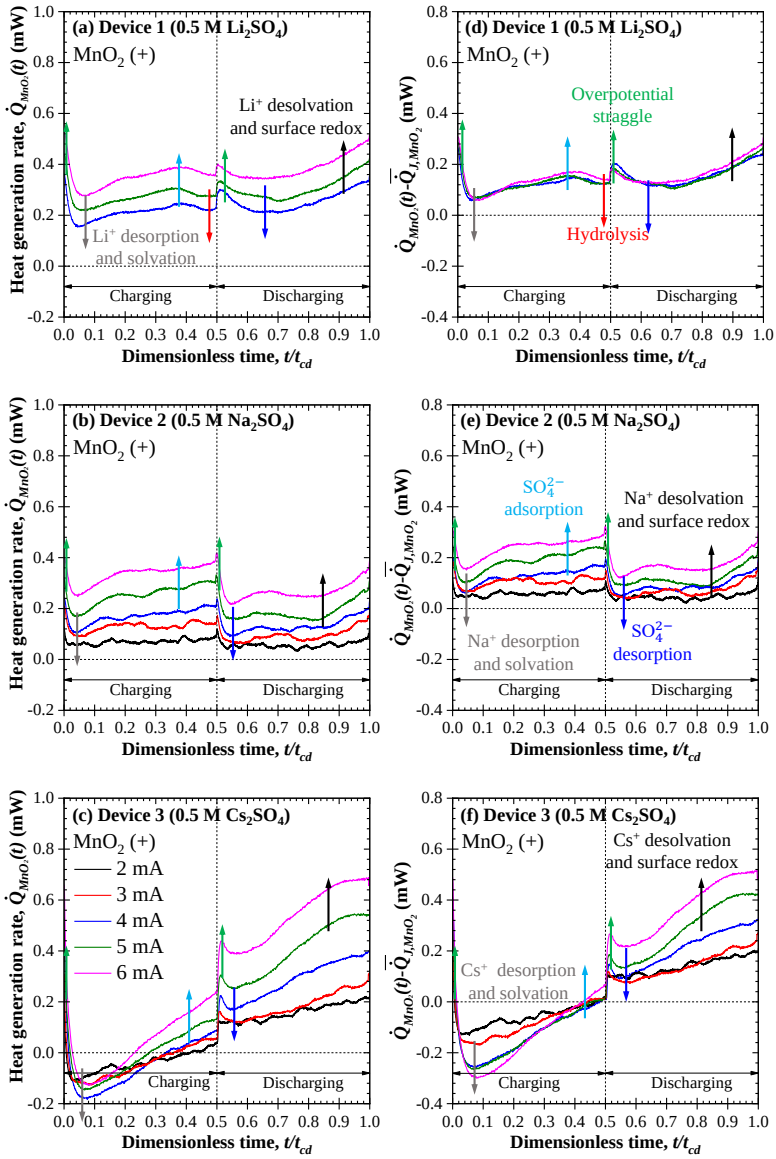

Figure 4.8: Instantaneous heat generation rate at the positive MnO_2 electrodes $\dot{Q}_{MnO_2}(t)$ for (a) Device 1 with 0.5 M Li_2SO_4, (b) Device 2 with 0.5 M Na_2SO_4, and (c) Device 3 with 0.5 M Cs_2SO_4 aqueous electrolytes and the instantaneous heat generation rate at the AC electrode $\dot{Q}_{MnO_2}(t)$ with subtracted Joule heating $\bar{\dot{Q}}_J$ for (d) Device 1 with 0.5 M Li_2SO_4, (e) Device 2 with 0.5 M Na_2SO_4, and (f) Device 3 with 0.5 M Cs_2SO_4 aqueous electrolytes as functions of dimensionless time t/t_{cd} and potential window $\Delta\psi_s = 1.6$ V, and current I ranging between 2 and 6 mA.

exothermic features at the AC electrode were attributed to cation adsorption (Na^+ and Cs^+) or possibly Li^+ surface redox during charging, and anion adsorption during discharging. Similarly, the observed exothermic features at the $\alpha-MnO_2$ electrode were attributed to anion adsorption during charging, and cation surface redox during discharging. For 0.5 M Li_2SO_4 aqueous electrolyte, an endothermic dip was observed towards the end of the charging step attributed to hydrolysis reaction. Overall, calorimetry offered a unique and detailed insight into the charging mechanisms.

CHAPTER 5

Charge and mass transfer resistances cause irreversible heat generation in pseudocapacitive electrodes

This chapter aims to theoretically elucidate the irreversible heat generation exceeding Joule heating observed experimentally in pseudocapacitive electrodes under galvanostatic cycling. The results establish that the additional irreversible heat generation is caused by the energy dissipation in charge and mass transfer resistances at the pseudocapacitive electrode. Simulations based on the modified Poisson-Nernst-Planck model coupled with the energy conservation equation were performed. The model accounted for (i) ion transport driven by the electric field in a binary and symmetric electrolyte, (ii) formation or dissolution of the electric double layer, (iii) redox reactions and ion intercalation/deintercalation at the electrode/electrolyte interface, and (iv) electron transport in the pseudocapacitive electrode. The reversible and irreversible heat generation rates, formulated from first principles, were also computed. Finally, the additional irreversible heat generation rate due to the charge transfer and mass transfer resistances was proportional to the square of the imposed current. Moreover, the charge and mass transfer resistances were found to be dependent on the state of charge of the electrode and the imposed current. Finally, the irreversible heat generation due to the charge and mass transfer resistances accounted for all of the additional irreversible heat generation that exceeded Joule heating.

5.1 Analysis

5.1.1 Schematic and assumptions

Figure 5.1 shows the schematic of the one-dimensional pseudocapacitive electrode simulated in a three-electrode setup along with the coordinate system used. The setup consisted of a planar pseudocapacitive electrode of thickness L_P composed of transition metal oxide M_pO_q and an organic electrolyte consisting of $LiClO_4$ salt dissolved in propylene carbonate (PC) of thickness L. The electrolyte domain was divided into two regions, namely, the Stern layer and the diffuse layer. Ions were immobile in the Stern layer and mobile under the effect of the electric field, ion concentration gradient, and steric repulsion in the diffuse layer. The electrode was subjected to constant current cycling imposed at the electrode/current collector interface (i.e., $x = -L - L_P$). The electrolyte center-line (i.e., $x = 0$) was kept at 0 V at all times, assuming the role of a reference electrode in a three-electrode experimental setup [3]. This simple geometry was chosen to assess the contributions of several physical phenomena contributing to heat generation rates based on the detailed model of d'Entremont and Pilon [75,77]. Several assumptions were made in the formulation of the model, previously discussed in detail in Refs. [75, 77, 89, 136]. In brief, (1) the electrolyte domain was binary and symmetric, and consisted of two ion species with identical valency $z = \pm 1$, ion size a, and diffusion coefficient D. (2) The salt was fully dissociated in the solvent and the bulk concentration for both species was c_∞. (3) No bulk fluid motion existed inside the cell. (4) The electrode and electrolyte transport properties were constant and independent of temperature. (5) The cell was thermally insulated from its surroundings. (6) The thickness H of the Stern layer was assumed to be half of the solvated ion diameter a (i.e., $H = a/2$) [81, 86, 137]. (7) The ion migration in the electrolyte as well as the Li^+ ion intercalation were treated as one-dimensional electrodiffusion. (8) No phase change occurred during the intercalation/deintercalation process [23, 138].

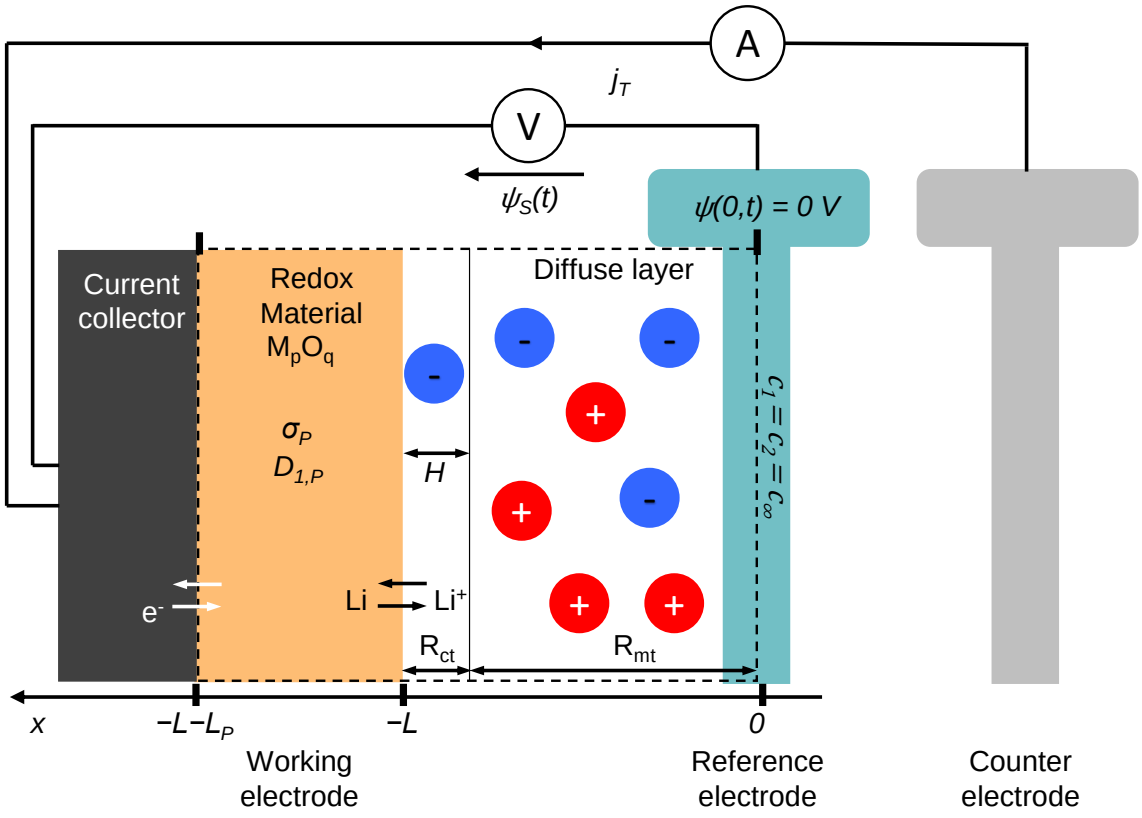

Figure 5.1: Schematic of the simulated one-dimensional M_pO_q electrode in a three-electrode setup (based on Ref. [3]).

5.1.2 Governing equations

The local potential $\psi(x,t)$ and concentration $c_i(x,t)$ in the electrode and electrolyte were governed by the modified Poisson-Nernst-Planck model [139–142]. The temperature $T(x,t)$ in the electrode and electrolyte was governed by the energy conservation equation [143, 144]. Moreover, the heat generation rates appearing in the energy conservation equation were derived from first principles [75, 77].

5.1.2.1 Poisson equation in the electrode and electrolyte

The Poisson equation governs the electric potential $\psi(x,t)$ in the electrode and electrolyte at location x and time t. In the electrode, it is expressed as [145–148]

$$\frac{\partial}{\partial x}\left(\sigma_P \frac{\partial \psi(x,t)}{\partial x}\right) = 0 \text{ for } -L - L_P \leq x < -L. \tag{5.1}$$

Here, σ_P is the electrical conductivity of the electrode (in S/m). In the electrolyte, it is given by [121, 140, 141]

$$\frac{\partial}{\partial x}\left(\varepsilon_0 \varepsilon_r \frac{\partial \psi(x,t)}{\partial x}\right) = \begin{cases} 0 & \text{in the Stern layer} \\ -F\sum_{i=1}^{2} z c_i(x,t) & \text{in the diffuse layer,} \end{cases} \tag{5.2}$$

where F is the Faraday constant (i.e., $F = 9.649 \times 10^4$ C/mol), $c_i(x,t)$ is the local concentration of ion species i ($i = 1$ or 2), and z is the valency of ions ($z = +1$ or -1). Furthermore, the vacuum permittivity and relative permittivity of the electrolyte are denoted by ε_0 and ε_r, respectively.

5.1.2.2 Mass conservation equation

In the diffuse layer, the mass conservation of the concentration c_i (in mol m^{-3}) of each ion species i is governed by [141]

$$\frac{\partial c_i}{\partial t} = -\frac{\partial N_i}{\partial x}, \tag{5.3}$$

where $N_i(x,t)$ is the molar flux (in mol/m^{2}s) of ion species i and can be expressed as [81]

$$N_i(x,t) = -\frac{DFzc_i}{R_u T}\frac{\partial \psi}{\partial x} - D\frac{\partial c_i}{\partial x} - \frac{DN_A c_i}{1 - \sum_{i=1}^{2}\left(\frac{c_i}{c_{max}}\right)} \sum_{j=1}^{2} a^3 \frac{\partial c_j}{\partial x}. \tag{5.4}$$

Here, D is the diffusion coefficient of ions in the solvent, R_u is the universal gas constant (i.e., $R_u = 8.314$ J/molK), T is the temperature (in K), N_A is the Avogadro constant (i.e., $N_A = 6.022 \times 10^{23}$ 1/mol), and a is the ion diameter. In addition, the first term on

the right hand side of Equation (5.4) accounts for migration of ions in an external electric field, the second term accounts for Fickian diffusion, and the last term accounts for steric repulsion due to finite ion size. This last term ensures that the local ion concentrations do not exceed their respective saturation concentrations estimated from simple cubic packing as $c_{max} = 1/(N_A a^3)$ [145, 147, 148]. Moreover, the mass conservation governing lithium concentration in the pseudocapacitive electrode $c_{1,P}(x,t)$ can be expressed as [76]

$$\frac{\partial c_{1,P}}{\partial t} = D_{1,P}\frac{\partial^2 c_{1,P}}{\partial x^2}. \tag{5.5}$$

Here, $D_{1,P}$ is the diffusion coefficient of the intercalated ions in the pseudocapacitive electrode.

5.1.2.3 Energy conservation equation

The 1D energy conservation equation in the electrode and electrolyte can be expressed as [143, 144]

$$\rho c_p \frac{\partial T}{\partial t} = \frac{\partial}{\partial x}\left(k\frac{\partial T}{\partial x}\right) + \dot{q} \qquad \text{for the electrolyte domain} \tag{5.6}$$

$$\text{and} \qquad \rho_P c_{p,P} \frac{\partial T_P}{\partial t} = \frac{\partial}{\partial x}\left(k_P\frac{\partial T_P}{\partial x}\right) + \frac{|j|^2}{\sigma_P} \qquad \text{for the electrode domain.} \tag{5.7}$$

Here ρ is the density (in kg/m^3), c_p is the specific heat (in J/kg·K), and k or k_P is the thermal conductivity (in W/m·K) of the electrolyte or the electrode, respectively. Furthermore, T is the temperature (in K) and $\dot{q}(x,t)$ is the local volumetric heat generation rate (in W/m^3) in the electrolyte, rigorously derived from first principles and expressed as [75, 77]

$$\dot{q}(x,t) = \dot{q}_E(x,t) + \dot{q}_S(x,t) + \dot{q}_F(x,t). \tag{5.8}$$

Here, $\dot{q}_{E(x,t)}$ is the heat generation rate arising from electric charge carriers (i.e., ions) decreasing their potential energy, $\dot{q}_S(x,t)$ termed as "heat of mixing" is the heat generation rate arising from ionic and electronic fluxes along the chemical potential, temperature, and

partial molar entropy gradients [75,149], and $\dot{q}_F(x,t)$ is the heat generation rate arising from redox reactions at the pseudocapacitive electrode/electrolyte interface [77]. Moreover, the heat generation rate $\dot{q}_E(x,t)$ can be expanded as [75]

$$\dot{q}_E(x,t) = \dot{q}_{E,J}(x,t) + \dot{q}_{E,d}(x,t) + \dot{q}_{E,s}(x,t). \tag{5.9}$$

Here, $\dot{q}_{E,J}(x,t)$ is the Joule heating expressed as [75],

$$\dot{q}_{E,J}(x,t) = \frac{j(x,t)^2}{\sigma(x,t)}, \tag{5.10}$$

where $j(x,t)$ is the local ionic current and $\sigma(x,t)$ is the electrical conductivity of the electrolyte (in S/m). They can be expressed as [141, 150, 151]

$$j(x,t) = F\sum_{i=1}^{2} zN_i(x,t) \tag{5.11}$$

$$\text{and } \sigma(x,t) = \frac{F^2}{R_u T}\sum_{i=1}^{2} z^2 D c_i(x,t). \tag{5.12}$$

Furthermore, $\dot{q}_{E,d}(x,t)$ is the heat generation rate due to ion diffusion given by [75]

$$\dot{q}_{E,d}(x,t) = \frac{DzF}{\sigma} j \frac{\partial(c_1 - c_2)}{\partial x}. \tag{5.13}$$

Moreover, $\dot{q}_{E,s}(x,t)$ is the heat generation rate due to steric effects arising from finite ion size and expressed as [75]

$$\dot{q}_{E,s}(x,t) = \frac{DzFa^3N_A(c_1 - c_2)}{\sigma[1 - a^3N_A(c_1 + c_2)]} j \frac{\partial(c_1 + c_2)}{\partial x}. \tag{5.14}$$

As ion concentration gradients become small, both $\dot{q}_{E,d}(x,t)$ and $\dot{q}_{E,s}(x,t)$ vanish, and heat generation reduces to Joule heating.

On the other hand, the heat of mixing contribution $\dot{q}_S(x,t)$ [Equation (5.8)] can be expanded as [75]

$$\dot{q}_S(x,t) = \dot{q}_{S,c}(x,t) + \dot{q}_{S,T}(x,t), \tag{5.15}$$

where the heat generation rate $\dot{q}_{S,c}$ arises from the thermodynamic activity and partial molar entropy gradients and $\dot{q}_{S,T}$ arises from the temperature gradient. They are given by [75]

$$\dot{q}_{S,c}(x,t) = \frac{3}{32\pi}\frac{eF^2}{(\epsilon_0\epsilon_r)^{3/2}(R_uT\sum_{i=1}^{2}z^2c_i)^{1/2}}\left(\sum_{i=1}^{2}z^2N_i\right)\left(\sum_{i=1}^{2}z^2\frac{\partial c_i}{\partial x}\right) \tag{5.16}$$

and

$$\dot{q}_{S,T}(x,t) = -\frac{3}{32\pi}\frac{eF^2(\sum_{i=1}^{2}z^2c_i)^{1/2}}{(\epsilon_0\epsilon_r)^{3/2}R_u^{1/2}T^{3/2}}\left(\sum_{i=1}^{2}z^2N_i\right)\frac{\partial T}{\partial x}. \tag{5.17}$$

Here, e is the elementary charge (i.e., $e = 1.6\times10^{-19}$ C). Finally, the reversible and irreversible heat generation rates due to redox reactions were uniform in the Stern layer and can be expressed as [77]

$$\dot{q}_F(t) = \dot{q}_{F,rev}(t) + \dot{q}_{F,irr}(t) = \frac{j_F(t)}{H}\Pi(t) + \frac{j_F(t)}{H}\eta(t). \tag{5.18}$$

Here, $\eta(t)$ is the overpotential defined as the difference between the electric potential at the electrode/electrolyte interface and the equilibrium potential of the chemical reaction (i.e., $\eta(t) = \psi(x = H, t) - \psi_{eq}$ [86]). On the other hand $\Pi(t)$ is the Peltier coefficient (in J/C) representing the amount of heat carried per unit charge and is typically constant for hybrid supercapacitors [77].

5.1.3 Initial and boundary conditions

Initially, at $t = 0$, the electric potential $\psi(x, 0)$ was set to 0 V throughout the entire domain, i.e., [75]

$$\psi(x,0) = 0 \text{ V} \qquad \text{for all } x. \tag{5.19}$$

For galvanostatic cycling, the boundary condition at the current collector/electrode interface (i.e., $x = -L - L_P$) was [81]

$$j_s(-L-L_P,t) = \begin{cases} j_s & \text{for } \psi_{min} < \psi_s < \psi_{max} \text{ and } d\psi/dt > 0 \text{ or } \psi_s = \psi_{min} \\ -j_s & \text{for } \psi_{min} < \psi_s < \psi_{max} \text{ and } d\psi/dt < 0 \text{ or } \psi_s = \psi_{max}, \end{cases} \tag{5.20}$$

where j_s is the imposed current, and $\psi_{min} = 0$ V and $\psi_{max} = 0.5$ V are the minimum and maximum electric potentials, respectively. Indeed this was an appropriate boundary condition consistent with experiments [77].

Furthermore, at the electrolyte center-line (i.e., $x = 0$) the imposed potential was 0 V at all times to simulate a reference electrode in a three-electrode experimental setup [136], i.e.,

$$\psi(0, t) = 0 \text{ V}. \tag{5.21}$$

In addition, the electric potential and current density were continuous at the electrode/electrolyte interface located at $x = -L$ so that [140]

$$\psi(-L^-, t) = \psi(-L^+, t) \quad \text{and} \quad \sigma_e \frac{\partial \psi}{\partial x}(-L^-, t) = \varepsilon_0 \varepsilon_r \frac{\partial^2 \psi}{\partial x \partial t}(-L^+, t). \tag{5.22}$$

Finally, the electric potential as well as the electric displacement were continuous at the Stern/diffuse layer interface located at $x = -L + H$, i.e. [121, 140, 152],

$$\psi(-L + H^-, t) = \psi(-L + H^+, t) \quad \text{and} \quad \frac{\partial \psi}{\partial x}(-L + H^-, t) = \frac{\partial \psi}{\partial x}(-L + H^+, t). \tag{5.23}$$

The initial concentrations $c_i(x, t)$ in the electrolyte and $c_{1,P}(x, t)$ in the pseudocapacitive electrode were [75, 77]

$$c_i(x, 0) = c_\infty \text{ for } -L < x \leq 0 \tag{5.24}$$

$$\text{and } c_{1,P}(x, 0) = c_{1,P,0} \text{ for } -L - L_P < x \leq -L. \tag{5.25}$$

The concentrations of both ion species at the electrolyte center-line (i.e., $x = 0$) were taken as the bulk ion concentrations, i.e.,

$$c_1(0, t) = c_2(0, t) = c_\infty. \tag{5.26}$$

The flux of the second ion species (i.e., $i = 2$) vanished at the electrode/electrolyte interface

as these ions could not intercalate into the electrodes, i.e.,

$$N_2(-L+H,t) = 0 \text{ mol/m}^2 \cdot \text{s}. \tag{5.27}$$

Furthermore, Li^+ ion intercalation into the electrode from the electrolyte was driven by redox reactions and such that

$$N_{1,P}(-L,t) = N_1(-L+H,t) = \frac{j_F(t)}{zF}. \tag{5.28}$$

However, no Li^+ ions intercalated into the current collector, i.e.,

$$N_{1,P}(-L-L_P,t) = 0 \text{ mol/m}^2 \cdot \text{s}. \tag{5.29}$$

The initial condition for the energy conservation equation consisted of imposed uniform ambient temperature throughout the entire computational domain as [75]

$$T(x,0) = T_0 \qquad \text{for all } x. \tag{5.30}$$

The simulated domain was thermally insulated at the current collector surface and at the electrolyte center-line so that

$$\frac{\partial T}{\partial x}(-L-L_P,t) = \frac{\partial T}{\partial x}(0,t) = 0 \text{ K/m} \tag{5.31}$$

In addition, the temperature and heat flux were continuous at the electrode/electrolyte interface located at $x = -L$ as

$$T(-L^-,t) = T(-L^+,t) \quad \text{and} \quad k_P \frac{\partial T}{\partial x}(-L^-,t) = k \frac{\partial T}{\partial x}(-L^+,t). \tag{5.32}$$

Similarly, they were also continuous at the Stern/diffuse layer interface located at $x =$

$-L+H$, i.e., [75]

$$T(-L+H^-,t) = T(-L+H^+,t) \quad \text{and} \quad \frac{\partial T}{\partial x}(-L+H^-,t) = \frac{\partial T}{\partial x}(-L+H^+,t). \tag{5.33}$$

5.1.4 Constitutive relationships

The present study focuses on MnO_2 pseudocapacitive electrode and the electrolyte consisting of $LiClO_4$ salt dissolved in propylene carbonate (PC) at room temperature with $\varepsilon_r = 64.4$ [153]. The electrical conductivity σ_P of MnO_2 was reported to range between 1 and 10^{-2} S/m [154] and was arbitrarily taken as $\sigma_P = 0.1$ S/m. The solvated ion diameter a was assumed to be 0.67 nm and the diffusion coefficient D of was 2×10^{-10} m^2/s [155]. The concentration of each ion species in the bulk of electrolyte c_∞ was assumed to be 1 M. Moreover, the minimum and maximum electric potential were limited to $\psi_{s,min} = 0$ V and $\psi_{s,max} = 0.5$ V, respectively. The equilibrium potential ψ_{eq}(t) (in V) was that of MnO_2 thick films, proposed by Guillemet et al. [156] and expressed as

$$\Delta\psi_{eq}(t) = 10.5[4 - c_{1,P}(t)/c_{1,P,max}] - 39.9. \tag{5.34}$$

Table 5.1 summarizes the parameters used in the simulations which were taken from the literature when available.

5.1.5 Charge and mass transfer resistances

The faradaic current j_F, given by the Frumkin-Butler-Wolmer equation [86], arose from the redox reaction in the Stern layer and was driven by the surface overpotential η. Thus, the charge transfer resistance R_{ct} associated with such reaction can be expressed as [86]

$$R_{ct} = \frac{\eta}{j_F}. \tag{5.35}$$

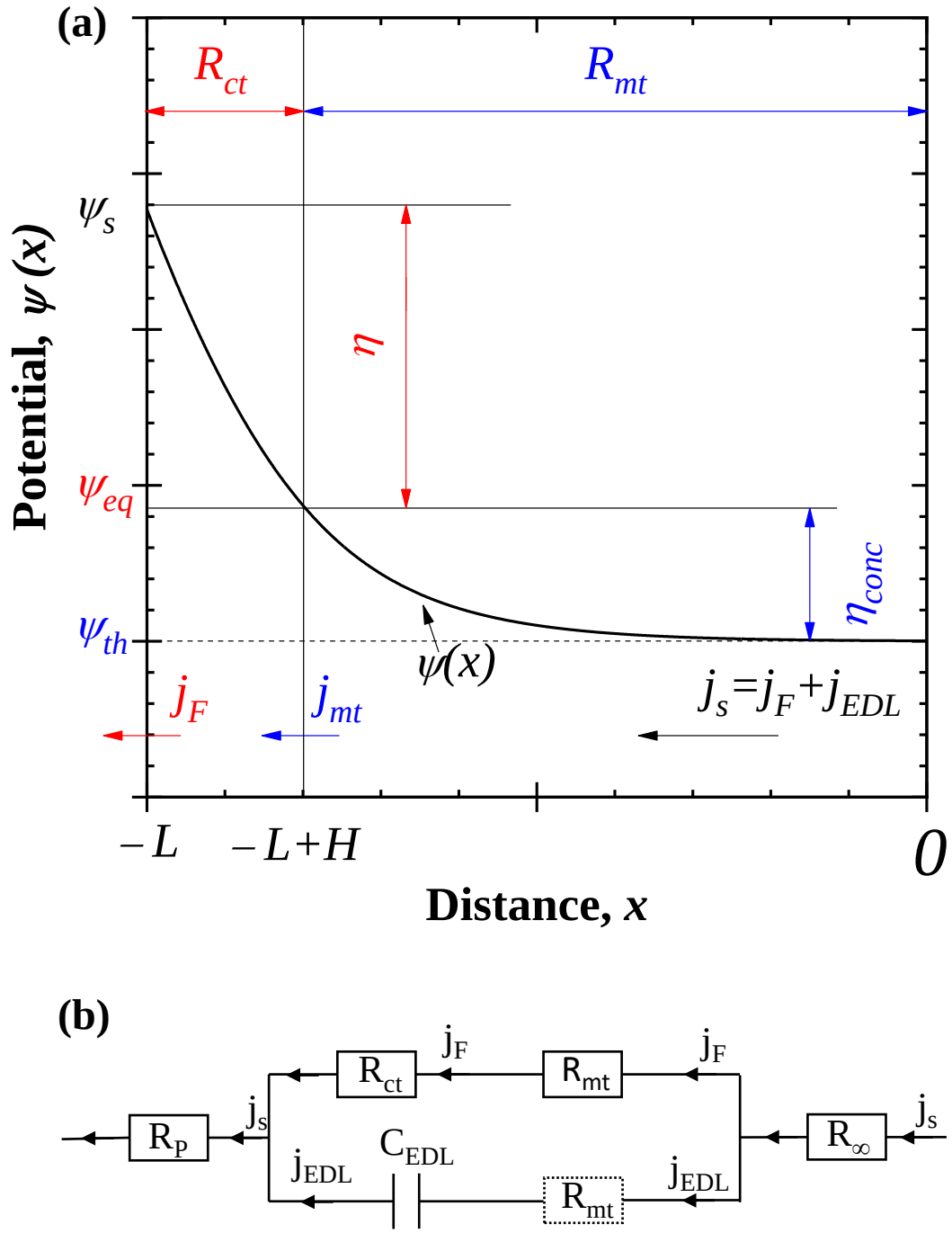

Figure 5.2: (a) Electric potential profile near the electrode with the charge transfer resistance R_{ct} and the mass transfer resistance R_{mt} and (b) the corresponding RC circuit scheme of the proposed model.

Table 5.1: Values and range of electrode and electrolyte properties and dimensions used in the simulations.

Parameter	**Symbol**	**Value**	**Unit**
Pseudocapacitive electrode conductivity	σ_P	0.1	S/m
Maximum Li^+ concentration in electrode	$c_{1,P,max}$	31.9	mol/L
Initial Li^+ concentration in electrode	$c_{1,P,0}$	6.38	mol/L
Reaction rate constant	k_0	10^{-8}	$m^{1+3\,\alpha}mol^{-\alpha}s^{-1}$
Transfer coefficient	α	0.5	-
Li^+ diffusion coefficient in the electrode	$D_{1,P}$	10^{-14}	m^2/s
Bulk ion concentration	c_∞	1	mol/L
Ion valency	z	± 1	-
Dielectric constant of PC	ϵ_r	64.4	-
Ion diameter	a	0.67	nm
Diffusion coefficient of ions in PC	D	1.7 x 10^{-10}	m^2/s
Pseudocapacitive electrode thickness	L_P	100	nm
Electrolyte thickness	L	1	μm
Imposed current	j_s	1 - 5	mA/cm^2
Lower potential limit	ψ_{min}	0	V
Upper potential limit	ψ_{max}	0.5	V
Ambient temperature	T	298	K

Similarly, the mass transfer resistance R_{mt} in the presence of an external electric field can be expressed as [86]

$$R_{mt} = \frac{-\eta_{conc}}{j_{mt}}. \tag{5.36}$$

Here, j_{mt} represents the current flowing through the mass transfer resistance and the concentration overpotential η_{conc} is given by the Nernst equation [86] accounting for the external electric field and expressed as

$$\eta_{conc} = \left(\frac{R_u T}{zF} + \Delta\psi_D \right) \ln Q_r. \tag{5.37}$$

Here $\Delta\psi_D$ is the potential drop across the diffuse layer defined as $\Delta\psi_D = \psi(-L + H, t) - \psi(0, t)$ while Q_r is the reaction quotient for insoluble electrodes expressed as [86]

$$Q_r = \frac{j_s - j_{mt}}{j_s}. \tag{5.38}$$

Here, j_s is the imposed current during galvanostatic cycling. Substituting Equation (5.38) into Equation (5.37) and neglecting higher order terms in the Taylor series expansion of $\ln Q_r$ yields

$$\eta_{conc} = -\left(\frac{R_u T}{zF} + \Delta\psi_D \right) \frac{j_{mt}}{j_s}. \tag{5.39}$$

Moreover, substituting Equation (5.39) into Equation (5.36), and identifying the thermal potential as $\Delta\psi_{th} = R_u T/zF$ [86] yields

$$R_{mt} = \frac{\Delta\psi_{th} + \Delta\psi_D}{|j_s|}. \tag{5.40}$$

Recognizing that at room temperature $\Delta\psi_D$ is at least one order of magnitude larger than $\Delta\psi_{th} \approx 0.01V$ realistically, Equation (5.40) further simplifies to

$$R_{mt} = \frac{\Delta\psi_D}{|j_s|}. \tag{5.41}$$

Finally, the mass transfer current j_{mt} passing through the mass transfer resistance is either associated with (a) the redox reaction consuming ions in the Stern layer (i.e., $j_{mt} = j_F$), or (b) the ability of the system to transport ions to the reaction site (i.e., $j_{mt} = j_{EDL}$), so that

$$j_{mt} = \begin{cases} j_F & \text{if } j_F < j_{EDL}. \\ j_{EDL} & \text{if } j_{EDL} < j_F. \end{cases} \tag{5.42}$$

Furthermore, irreversible heat generation rate due to charge transfer and ion transport can be expressed as resistive losses through the charge transfer and mass transfer resistance so that

$$\dot{Q}_{ct} = R_{ct} j_F^2 = \eta j_F \tag{5.43}$$

$$\text{and } \dot{Q}_{mt} = R_{mt} j_{mt}^2 = -\eta_{conc} j_{mt}. \tag{5.44}$$

Figure 5.2(a) shows the electric potential profile near the pseudocapacitive electrode featuring the charge transfer resistance R_{ct} and the mass transfer resistance R_{mt}. Moreover, it shows the electric potentials η and η_{conc} driving the faradaic j_F and mass transfer j_{mt} currents though the charge R_{ct} and R_{mt} resistances, respectively. Figure 5.2(b) shows the equivalent RC circuit and indicates that R_{mt} is associated with the branch through which the smaller of the two currents (i.e., j_F or j_{EDL}) passes. Please note that in EDLCs no redox reactions occur, hence, the faradaic current j_F vanishes and the charge transfer resistance R_{ct} becomes infinite. Thus, the irreversible heat generation due to charge transfer resistance vanishes. Conversely, no current flows through R_{mt}. Then, the irreversible heat generation due to mass transfer resistance also vanishes and the model reduces to Joule heating.

The total time-averaged irreversible heat generation rate can be computed as

$$\overline{\dot{Q}}_T = \overline{\dot{Q}}_J + \overline{\dot{Q}}_{ct} + \overline{\dot{Q}}_{mt}. \tag{5.45}$$

$\bar{\dot{Q}}_T$ computed using Equation (5.45) was compared to the simulated total instantaneous heat generation rate obtained by solving Equations (5.8) to (5.18) averaged over one cycle and computed as

$$\bar{\dot{Q}}_T = \frac{1}{t_{cd}} \int_{nt_{cd}}^{(n+1)t_{cd}} \dot{Q}_T(t)\, \mathrm{d}t. \tag{5.46}$$

Indeed, by definition, time-averaging the reversible heat generation rate over the entire cycle equals to zero, thus Equation (5.46) corresponds to the average instantaneous irreversible heat generation rate.

5.1.6 Validation

The three-electrode setup model was validated against results from the electrochemical transport and heat generation model under galvanostatic conditions reported by d'Entremont and Pilon [75, 77, 149].

5.2 Results and discussion

5.2.1 Nyquist plot

Electrochemical impedance spectroscopy (EIS) simulations were performed with a bias DC potential $\psi_{DC} = 0.05$ V over a frequency range of f from 2 to 80,000 Hz. Figure 5.3 shows the Nyquist plot obtained from EIS featuring two semi-circles attributed to (i) the electrolyte resistance $R_e = L/\sigma_e$, and (ii) the sum $R_{ct} + R_{mt}$ of the charge and mass transfer resistances [89]. Moreover, the ohmic resistance from $Z(Re) = 0$ to the beginning of the first semi-circle was attributed to the electrode resistance $R_P = L_P/\sigma_P$ [1, 89]. The sum of the electrode and the electrolyte resistances$R_s = R_P + R_e$ obtained from EIS simulations was $R_s = 1.782 \times 10^{-6} \Omega$ m^2 and was in agreement with the computed resistance $R_s = 1.7828 \times 10^{-6} \Omega$ m^2. Then, the resistance obtained from the EIS simulations was used to predict the irreversible heat generation due to Joule heating as

$$\bar{\dot{Q}}_J = R_s j_s^2. \tag{5.47}$$

In addition, the predicted Joule heating $\bar{\dot{Q}}_J$ [Equation (5.47)] was compared to the time-averaged total heat generation rate $\bar{\dot{Q}}_T$ [Equation (5.46)]. The comparison revealed that the time-averaged heat generation rate $\bar{\dot{Q}}_T$ exceeded the predicted Joule heating $\bar{\dot{Q}}_J$.

5.2.2 Galvanostatic cycling

Figures 5.4(a) to 5.4(c) show the normalized imposed current density $j_s/|j_s|$, faradaic current density $j_F/|j_s|$, and capacitive current density $j_{EDL}/|j_s|$, as well as the surface overpotential

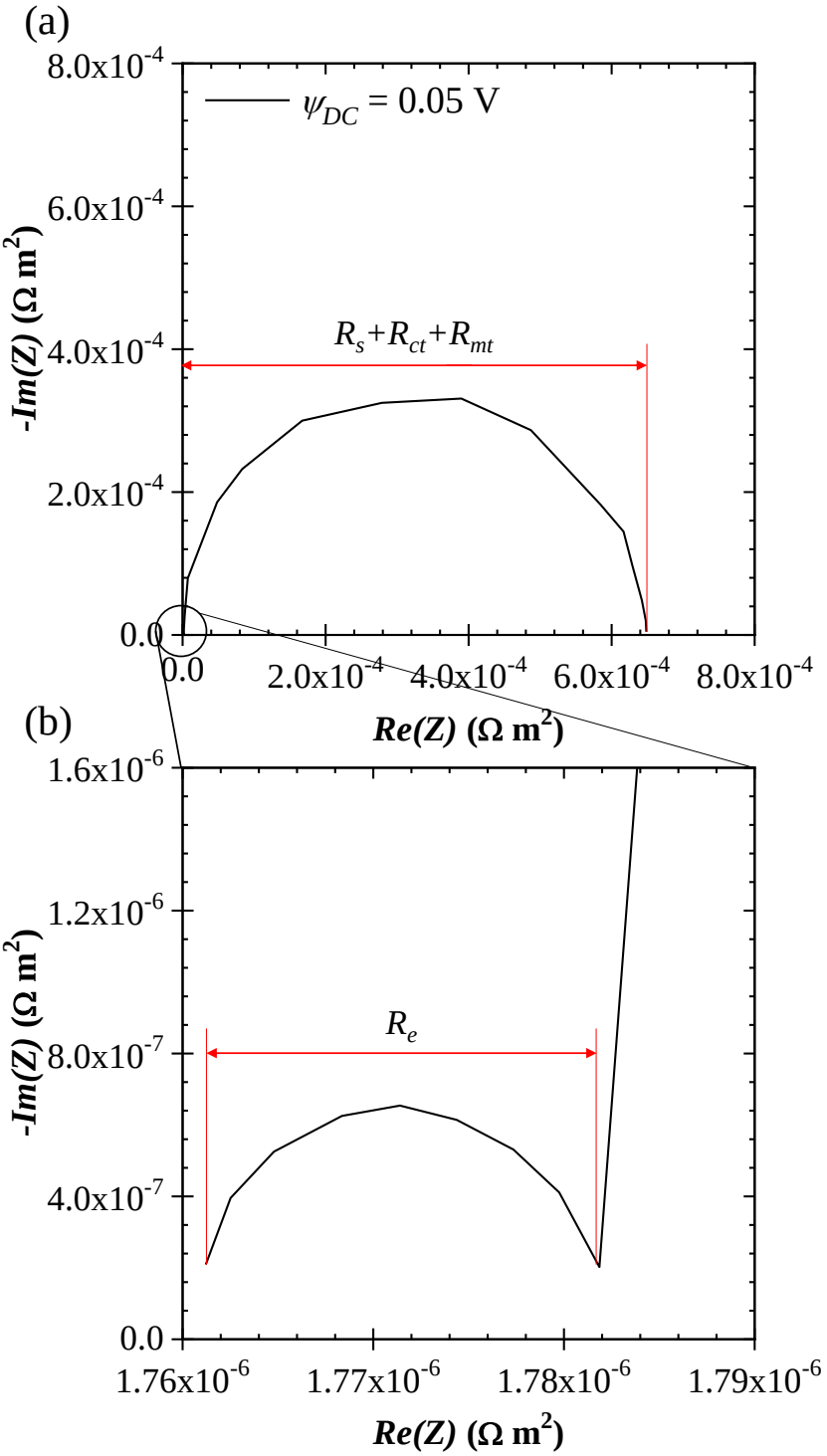

Figure 5.3: Nyquist plot obtained from electrochemical impedance spectroscopy simulations of the baseline case for $\psi_{DC} = 0.05$ V. (a) The end of the bigger semi-circle corresponds to the sum of the device resistance R_s and the charge and mass transfer resistances $R_{ct} + R_{mt}$ while (b) a zoomed-in small-semi circle corresponds to the electrolyte resistance R_e.

η for three imposed current densities $j_s = 1$, 2, and 4 mA/cm^2 as a function of dimensionless time t/t_{cd}. Here, two regimes of operation were identified as (i) the faradaic regime (i.e., $j_F > j_{EDL}$), and (ii) the capacitive regime (i.e., $j_{EDL} > j_F$). Moreover, Figure 5.4(d) shows the potential ψ_s for each of the imposed current densities as a function of dimensionless time t/t_{cd}. During fast charging, the fraction of faradaic current decreased and the capacitive regime dominated for the majority of the cycle. This was attributed to the slower redox reactions giving rise to the faradaic current compared to the faster EDL formation giving rise to the capacitive current. Moreover, Figures 5.4(a) to 5.4(c) establish, that the faradaic current j_F is the largest for small values of surface overpotential η [86]. In addition, the potential curves [Figure 5.4(d)] overlapped at the beginning of the cycle and then deviated from each other as the faradaic current j_F exhibited a local maximum. For smaller imposed current density $j_s = 1$ mA/cm^2 redox reactions were more intense and the fraction of faradaic current j_F/j_s was larger. Therefore, the potential ψ_s deviated more from the ideal triangular shape typical for EDLCs. Indeed, for the largest imposed current density $j_s = 4$ mA/cm^2 the fraction of faradaic current was the smallest and potential ψ_s evolution was nearly triangular. Finally, the potential vs. time curves [Figure 5.4(d)] during the discharging step changed their slopes when the faradaic current j_F [Figure 5.4(a)-5.4(c)] changed from concave shape to convex shape. This also coincided with the flattening of the overpotential η.

5.2.3 Instantaneous and time-averaged heat generation rates

Figure 5.5(a) shows the simulated total instantaneous heat generation rate $\dot{Q}_T(t)$ as a function of dimensionless time t/t_{cd} for three imposed current densities $j_s = 1$, 2, and 4 mA/cm^2. At the beginning of the charging cycle the heat generation was endothermic due to the non-spontaneous deintercalation of Li^+ from the pseudocapacitive electrode. Towards the end of the charging step, the deintercalation process slowed down due to the Li^+ ion starvation in the pseudocapacitive electrode. Then, the electric double layer (EDL) formation began to dominate the charge storage, thus the capacitive current j_{EDL} dominated over the faradaic current j_F [Figure 5.4(a)-5.4(c)] causing an exothermic total instantaneous heat generation rate. Furthermore, at the beginning of the discharging step, the total instantaneous heat

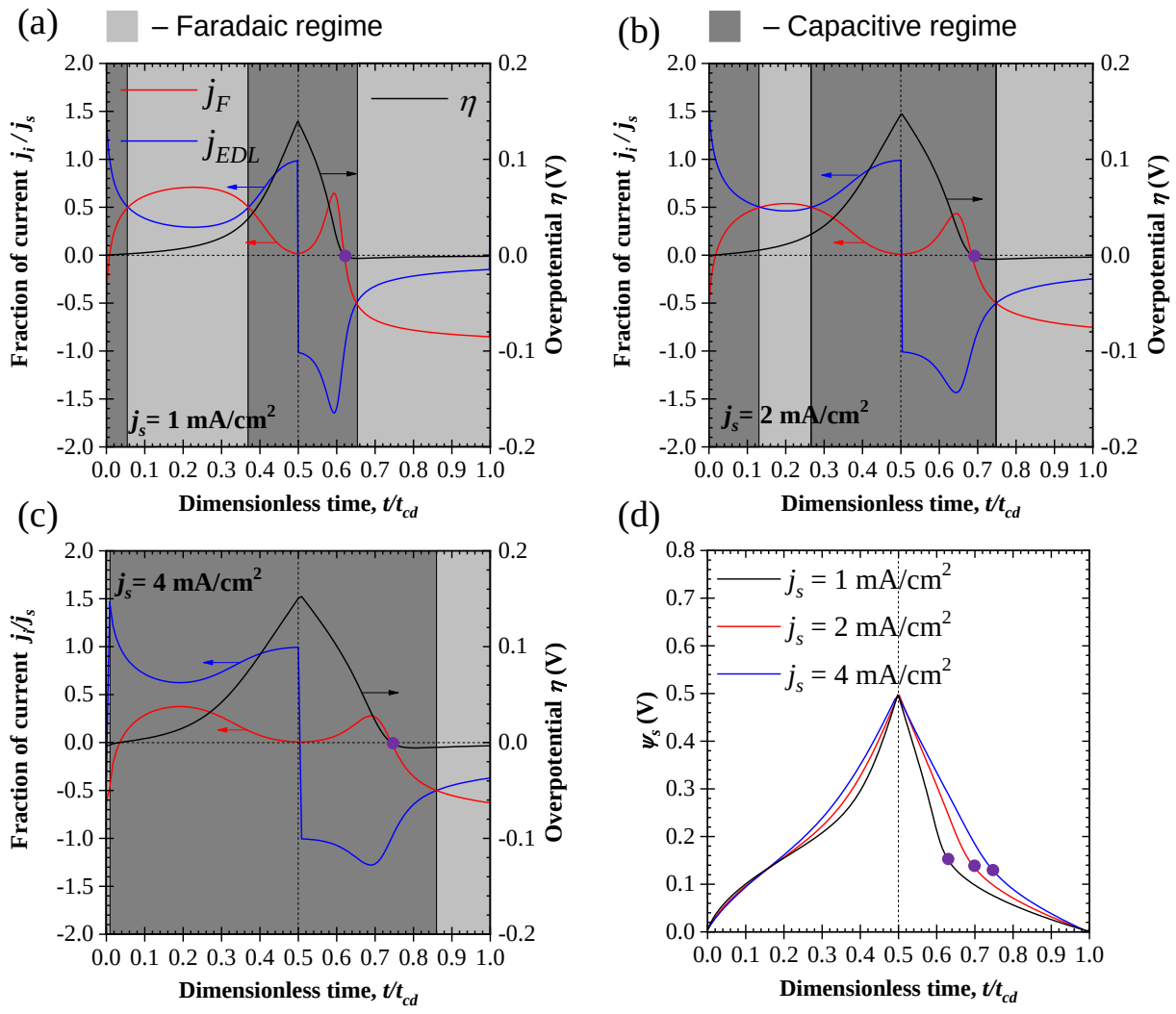

Figure 5.4: Faradaic and capacitive fractions of the current for imposed current of (a) $j_s = 1$ mA/cm^2, (b) $j_s = 2$ mA/cm^2, and (c) $j_s = 4$ mA/cm^2, and the corresponding potential as a function of dimensionless time t/t_{cd} and (d) the potential vs. dimensionless time curves for imposed current density j_s.

generation rate was dominated by the endothermic EDL dissolution and j_{EDL} dominated over j_F. Finally, at the end of the discharging step, the total heat generation was dominated by the exothermic Li^+ ion intercalation into the pseudocapacitive electrode.

Figure 5.5(b) shows the time-averaged irreversible heat generation rate $\bar{\dot{Q}}_T$ computed from $\dot{Q}_T(t)$ using Equation(5.46) as a function of j_s^2. This irreversible heat generation was compared to the total irreversible heat generation rate computed using Equation (5.45) and accounting for the contributions from all resistances, namely, $\bar{\dot{Q}}_T = \bar{\dot{Q}}_J + \bar{\dot{Q}}_{ct} + \bar{\dot{Q}}_{mt}$. Figure 5.5(b) also shows the charge transfer and mass transfer contributions to the average total irreversible heat generation rate. First, the time-averaged irreversible heat generation rate exceeded the predicted Joule heating. Furthermore, the total heat generation rates $\bar{\dot{Q}}_T$ computed from Equation (5.45) and Equation (5.46) were practically identical, collapsing on top of each other. This established that the additional irreversibilities in the system were caused only by the charge transfer process and ion transport. The difference between Joule heating $\bar{\dot{Q}}_J$ and total irreversible heat generation $\bar{\dot{Q}}_T$ increased rapidly at lower current density and then slowed down with increasing current density j_s. This was in good agreement with experimental observations by Munteshari et al. [24]. Using a square root fit, it was determined that the evolution of the time-averaged irreversible heat generation rate $\overline{\dot{Q}_T}$ increased linearly with imposed current j_s with R^2 of 0.999.

5.2.4 Discussion

Figure 5.6(a) shows the charge transfer resistance R_{ct} as a function of dimensionless time t/t_{cd} indicating that R_{ct} was dependent on the state of charge of the electrode. The charge transfer resistance was small in the faradaic regime, and increased rapidly when the surface overpotential increased towards the end of the charging step. Therefore, the charge transfer resistance was not constant, but it was dependent on the state of charge of the pseudocapacitive electrode. It is important to note that the faradaic current decreased when the charge transfer resistance increased, due to the Li^+ ion starvation in the electrode. Thus, although the charge transfer resistance R_{ct} was large, it did not contribute much to the irreversible

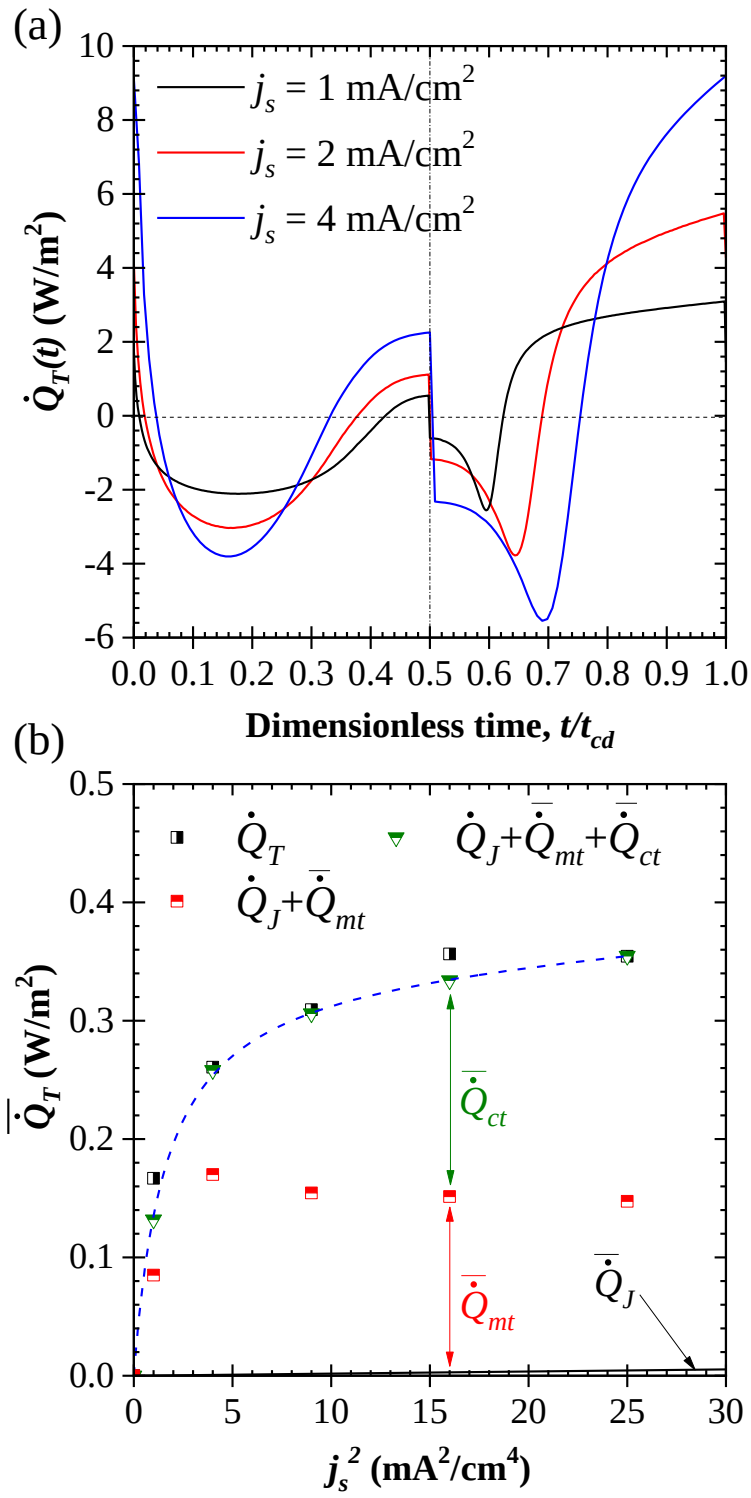

Figure 5.5: (a) Simulated total instantaneous heat generation rate $\dot{Q}_T$(t) for imposed current j_s = 1, 2, and 4 mA/cm^2, and (b) quantitative comparison of the time-averaged total irreversible heat generation rate $\bar{\dot{Q}}_T$ vs. j_s^2 computed from Equation (5.45) and Equation (5.46).

heat generation at the end of the charging step. Furthermore, Figure 5.6(b) shows the mass transfer resistance R_{mt} as a function of dimensionless time t/t_{cd} indicating that R_{mt} was also dependent on the state of charge of the pseudocapacitive electrode. The mass transfer resistance R_{mt} was small at the beginning of the charging step and it increased towards the maximum which occurred at the end of the charging step. At the beginning of the discharging step R_{mt} exhibited a steeper drop. As the discharging progressed, R_{mt} changed slope as the faradaic current j_F became convex [Figure 5.4(a)-5.4(c)] indicating the transition from the capacitive to faradaic regime.

Figure 5.7(a) shows the instantaneous irreversible heat generation rate due to the charge transfer resistance $\dot{Q}_{ct}(t)$ as a function of dimensionless time t/t_{cd} for current density $j_s = 1$, 2, and 4 mA/cm^2. The magnitude of $\dot{Q}_{ct}$ increased with increasing current density j_s. At the beginning of the charging, $\dot{Q}_{ct}(t)$ gradually increased and reached its local maximum around the time when the surface overpotential η began to rapidly increase [Figure 5.4(a)-5.4(c)]. After the local maximum $\dot{Q}_{ct}(t)$ rapidly decreased as the faradaic current j_F flowing through R_{ct} decreased. At the beginning of the discharging step $\dot{Q}_{ct}(t)$ increased and reached its global maximum when faradaic current j_F reached its local maximum. Then, $\dot{Q}_{ct}(t)$ dropped steeply with the diminishing faradaic current j_F. Moreover, $\dot{Q}_{ct}(t)$ touched the x-axis (i.e., $\dot{Q}_{ct} = 0$) when the faradaic current switched signs. Indeed, $\dot{Q}_{ct}(t)$ has a Joule-heating like form, thus it cannot be negative and can only vanish when j_F vanishes. Finally, towards the end of the discharging step $\dot{Q}_{ct}(t)$ increased before slowly decreasing until the end of discharging.

On the other hand, Figure 5.7(b) shows the instantaneous irreversible heat generation rate due to the mass transfer resistance $\dot{Q}_{mt}(t)$ as a function of dimensionless time t/t_{cd} for current density $j_s = 1$, 2, and 4 mA/cm^2. At the beginning of the charging step $\dot{Q}_{mt}(t)$ increased. However, for smaller imposed current density j_s, the increase was cut short by the mass transfer limitations. Under these circumstances, the chemical reactions in the Stern layer were so rapid that the Li^+ cations deintercalating from the pseudocapacitive electrode could not be transported away from the reaction site fast enough. Indeed, Figure 5.7(b) features a non-smooth change of $\dot{Q}_{mt}(t)$ during charging resulting from the diffusion limitations.

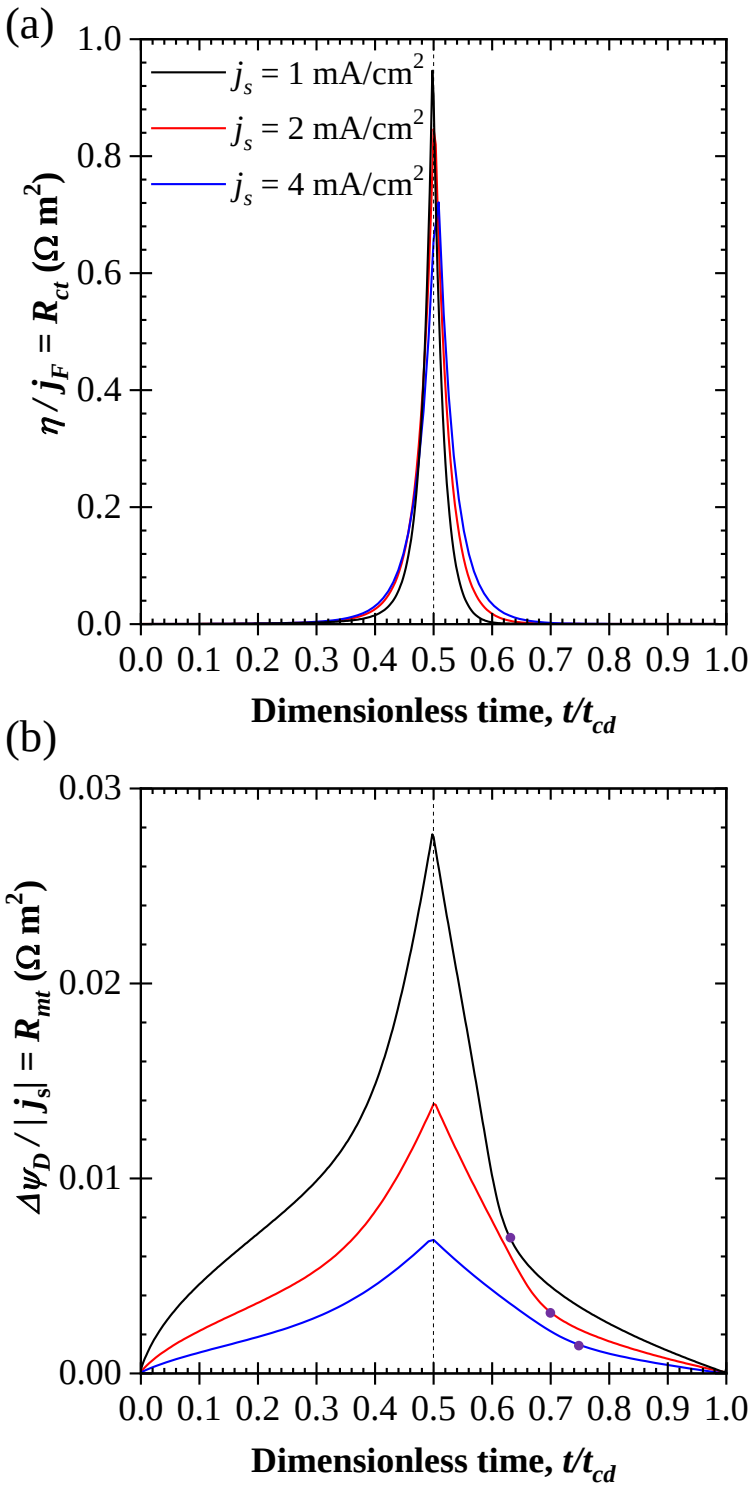

Figure 5.6: (a) The charge transfer resistance R_{ct} as a function of dimensionless time t/t_{cd}, and (b) the mass transfer resistance R_{mt} as a function of time t/t_{cd}, for imposed current j_s = 1, 2, and 4 mA/cm^2.

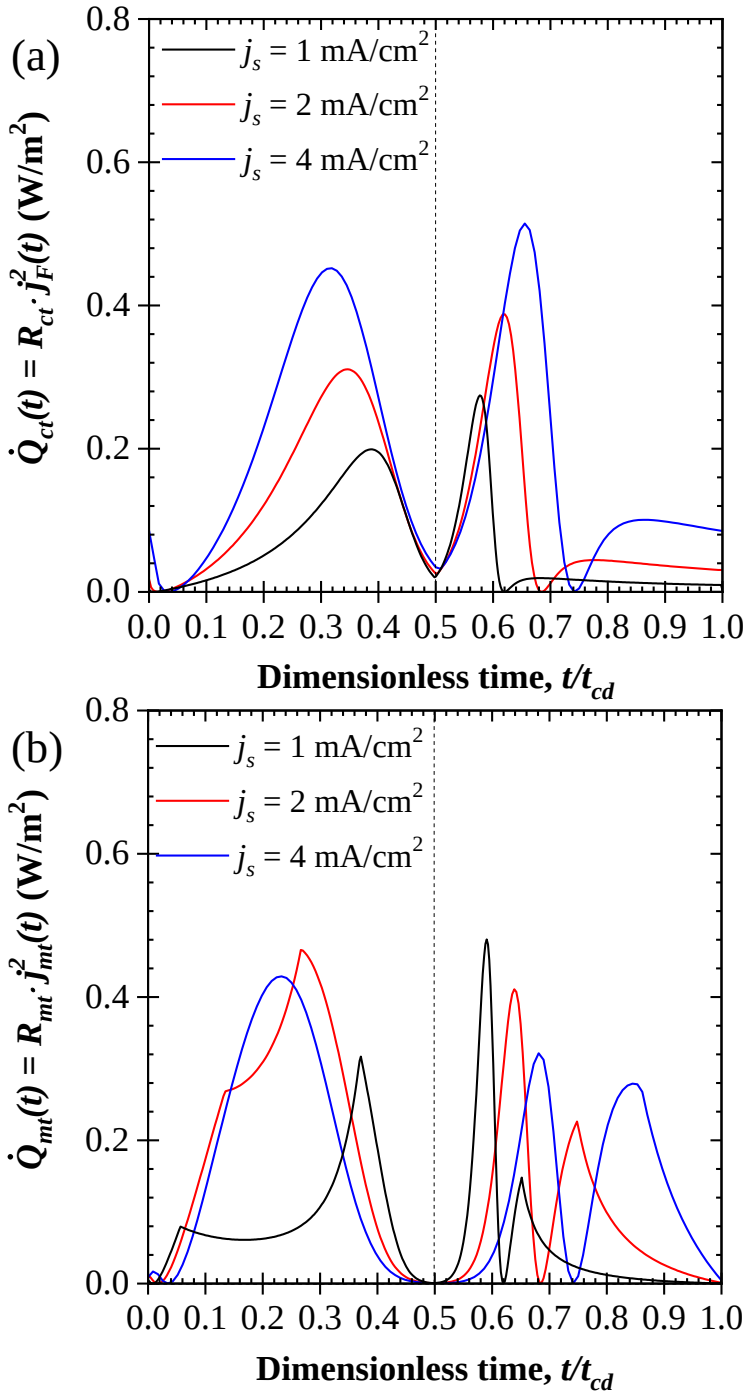

Figure 5.7: (a) The instantaneous irreversible heat generation rate due to the charge transfer resistance R_{ct} as a function of dimensionless time t/t_{cd}, and (b) the instantaneous irreversible heat generation rate due to the mass transfer resistance R_{mt} as a function of dimensionless time t/t_{cd}, for imposed current $j_s = 1$, 2, and 4 mA/cm^2.

Interestingly, for higher values of the imposed current density j_s (i.e. $j_s = 4$ mA/cm^2), the mass transfer was not limiting. At the beginning of the discharging step, a large spike in the heat generation rate was observed for all current densities j_s. It was followed by an increase in the heat generation rate which was cut short by the mass transfer limitation for small values of the imposed current $j_s = 1$ and 2 mA/cm^2. Similar to the charging cycle, the change of $\dot{Q}_{mt}(t)$ was not smooth. For higher value of $j_s = 4$ mA/cm^2, the mass transfer limitation was not present. Interestingly, the magnitude of $\dot{Q}_{mt}(t)$ decreased with increasing imposed current j_s. However, due to the mass transfer limitations the average heat generation due to the mass transfer resistance $\dot{Q}_{mt}(t)$ initially increased and then decreased with increasing current density j_s [Figure 5.5(b)].

5.3 Conclusion

This study proposed a newly developed model for the prediction of the instantaneous irreversible heat generation rates due to the charge transfer and mass transfer resistances. First, the total instantaneous heat generation rates for varying current densities were predicted from numerical simulations. Then, they were averaged over the charge/discharge cycle to calculate the average irreversible heat generation rate. Simultaneously, the charge and mass transfer resistances and their irreversible heat generation rates were computed and added to the predicted Joule heating. Then, the two results were compared and were found to be practically identical. Thus, it was concluded that the charge and mass transfer resistances are solely responsible for the additional irreversible heat generation beyond Joule heating in the simulated domain. Therefore, the heat generation due to the charge and mass transfer resistances must be accounted for when designing a hybrid supercapacitor cell. Finally, the computations indicate, that the effect of heat generation due to the charge and mass transfer resistances is more pronounced at lower operating currents, and then approaches Joule heating as a linear function of the imposed current. This was explained by the decrease of the faradaic fraction of the current density as the imposed current density increased. Indeed, as the imposed current density increased the faradaic (redox) reactions became less intense

making it possible for ion transport to keep up with them.

CHAPTER 6

Potentiometric entropic measurements inform the structural evolution of $Li_xNa_{1.5-x}VOPO_4F_{0.5}$

This chapter aims to elucidate the charging mechanism and the origin of the excellent rate performance of $Li_xNa_{1.5-x}VOPO_4F_{0.5}$ (LNVOPF). To do so, entropic potential evolution was calculated via a theoretical model of solid solution with ion ordering. Moreover, potentiometric entropic potential measurements were also performed. The coin cells consisted of an LNVOPF based cathode and an elemental Li anode LNVOPF with 1 M $LiPF_6$ in EC:DMC electrolyte and the potential window between 3.0 and 4.5 V vs. Li/Li^+. LNVOPF was synthesized via electrochemical Li exchange of $Na_{1.5}VOPO_4F_{0.5}$ (NVOPF). The LNVOPF particles were either micron sized (i.e., *micronbricks*) or nano sized (i.e., *nanoparticles*). Moreover, the binders were either P3HT or PVDF. Overall, three coin cells with (i) LNVOPF *micronbricks* and P3HT, (ii) LNVOPF *nanoparticles* and P3HT, and (iii) LNVOPF *nanoparticles* and PVDF were tested. The entropic potential was measured and the apparent diffusion coefficient of Li in LNVOPF was computed for each coin cell during delithiation and lithiation. The measured and calculated entropic potentials exhibited the same trends for all investigated coin cells. Moreover, it was found that the extent of Li exchange can impact the entropic potential and the apparent diffusion coefficient of Li in the electrode during lithiation. Concretely, higher concentration of the exchanged Li resulted in a more pronounced oscillations in the entropic potential at higher values of the open circuit voltage. Moreover, the apparent diffusion coefficient of Li in the electrode was also higher for higher concentration of the exchanged Li.

6.1 Background

6.1.1 NVOPF and LNVOPF

The use of $Na_{1.5}VOPO_4F_{0.5}$ (NVOPF) has been proven advantageous over its non-fluorinated counterpart $Na_3V_2(PO_4)_3$ due to its (i) larger capacity (130 mAh/g vs. 120 mAh/g) and (ii) increased upper limit ψ_{max} of the operating potential window (3.8 V vs. 3.6 V) [33, 157]. This improvement was attributed to the faster ion transport occurring in NVOPF due to the enhancement by the $[VO_5F]$ octahedra and $[PO_4]$ tetrahedra in the stoichiometric structure and the increased oxidation stability limit [158,159]. Materials structurally similar to NVOPF, such as $Na_3V_2(PO_4)_2F_3$ [158] and $Na_3V_2(PO_4)_3$ [160], feature two Na sites in the lattice (termed Na1 and Na2) that the intercalated Na ions can occupy [158,160,161]. As Na1 and Na2 have different binding energy, intercalated Na preferentially occupies the sites with lower binding energy [158,160,161]. Additionally, the transport of Na in layered structures is fast in the planes between the layers resulting in high rate capability of such materials [32]. This effect is also enhanced by the large energy barriers for interplane transport [32].

To further improve the electrochemical performance, Li exchange of Na in NVOPF has been considered [33]. The increased capacity and improved rate performance stems from the lower standard reduction potential, lower atomic weight, and smaller ionic radius of Li compared to Na [160–163]. Indeed, Li faces a smaller activation barrier compared to Na and can accommodate higher currents via faster in plane transport within the layers of the electrode material [160]. Li exchange of NVOPF can be performed either chemically or electrochemically. During this process, x amount of Na is substituted by Li resulting in a compound with the stoichiometric chemical formula of $Li_xNa_{1.5-x}VOPO_4F_{0.5}$ (LNVOPF). Chemical Li exchange is governed by diffusion and performed by immersing pristine NVOPF in a Li rich electrolyte solution ($\geq$ 5 M) such as LiBr in hexanol [161,164,165] or acetonitrile [161]. The time and temperature of chemical Li exchange vary from 6 to 48 hours and 85 to 160 °C with higher level of Li substitution at longer exchange time and higher exchange temperature [161, 164, 165]. Chemical Li exchange resulted in the amount of substituted Li ranging between $x = 1.1$ and $x = 1.34$ [161, 165]. On the other hand, electrochemical Li

exchange can be performed at room temperature, with less concentrated electrolytes ($\geq$ 1 M), and much faster ($\leq$ 4 h) compared to chemical Li exchange [4,33,163]. It resulted in the amount of substituted Li normally between $x = 0.9$ and $x = 0.95$ [33] but in some cases as low as $x = 0.4$ [4]. By analogy, LNVOPF derived from NVOPF by the means of Li exchange features two Li sites with different binding energies in the lattice (Li1 and Li2) [161].

6.1.2 Interpretation of the entropic potential evolution

Recently, Baek et al. [31] established guidelines to interpret the entropic signature of the phenomena occurring in batteries during cycling based on experimental and theoretical results. They identified the simultaneous trends in $U_{ocv}(x,T)$ and $\partial U_{ocv}(x,T)/\partial T$ related to (i) ion ordering in a solid solution, (ii) phase transformation with a two phase coexistence, and (iii) phase transformation with a stable intermediate phase [31]. They found that in a solid solution $U_{ocv}(x,T)$ and $\partial U_{ocv}(x,T)/\partial T$ changed linearly during charging/discharging [31]. However, during ion ordering, the slope of $U_{ocv}(x,T)$ increased while $\partial U_{ocv}(x,T)/\partial T$ followed a tilde shape [31]. Moreover, they found that during a phase transformation with two phase coexistence $U_{ocv}(x,T)$ and $\partial U_{ocv}(x,T)/\partial T$ remained constant [31]. Finally, during a phase transformation with a stable intermediate phase $U_{ocv}(x,T)$ and $\partial U_{ocv}(x,T)/\partial T$ initially exhibited a plateau. Then, when the system passed over the stable intermediate phase, they exhibited a rapid change leading to a second plateau [31].

Several studies measured the entropic potential of various metal oxide battery electrodes exhibiting (i) ion ordering [31,93–97], (ii) phase transformation with two phase coexistence [166, 167], and (iii) phase transformation with a stable intermediate phase [31]. Indeed, $U_{ocv}(x,T)$ and $\partial U_{ocv}(x,T)/\partial T$ evolution vs. x in materials such as Li_xTiS_2 [95], Li_xCoO_2 [31], $Li_xPNb_9O_25$ [93], $Li_xTiNb_2O_7$ [94], and $Li_{1-\delta}Mn_2O_4$ [96, 97] featured the same trends as observed in theoretical models [31]. Interestingly, in Li_xTiS_2, Li_xCoO_2, $Li_xPNb_9O_25$, and $Li_xTiNb_2O_7$, ion ordering occurred at lower Li compositions [31,93–95]. Moreover, at higher x composition Li_xCoO_2 featured a plateau in both $U_{ocv}(x,T)$ and $\partial U_{ocv}(x,T)/\partial T$ indicative a first order phase transition [93]. On the other hand, $Li_{1-\delta}Mn_2O_4$ first exhibited solid

solution behavior followed by ion ordering at $1-\delta = 0.5$ leading into another solid solution region at higher values of $1-\delta \geq 0.6$ [96, 97].

6.2 Analysis

A model consisting of two sublattices with different Li binding energies and without Li-Li interactions was considered [31]. Here, each sublattice contributed half of the Li sites to the lattice [31]. Then, the Gibbs free energy of the Li_xMA electrode can be expressed as [31]

$$\begin{aligned} g_{Li_xMA}(x,T) &= g_{MA}(T) + \epsilon_1 x_1 + \epsilon_2 x_2 \\ &+ k_B T[x_1 ln(x_1) + (1-x_1) ln(1-x_1)] + k_B T[x_2 ln(x_2) + (1-x_2) ln(1-x_2)]. \end{aligned} \tag{6.1}$$

Here, $g_{Li_xMA}(x,T)$ is the Gibbs free energy of an ideal solid solution (in J), $g_{MA}(x)$ is the Gibbs free energy of the metal oxide electrode (in J), ϵ_1 and ϵ_2 are the energies of the Li sites in each sublattice and such that $\epsilon_1 \geq \epsilon_2$. Moreover, x_1 and x_2 represent the occupied fraction of Li sites in each sublattice and are confined between 0 and 1. They are related to the overall Li composition as $x = (x_1 + x_2)/2$ [31]. Thus, x_1 and x_2 are not independent variables and Li can order between Li sites to minimize the Gibbs free energy of the system. Indeed, the amount of Li in one sublattice can be expressed as a function of the other and the overall concentration as $x_2 = 2x - x_1$ [31]. Please note, that in thermodynamic equilibrium (i.e., infinite relaxation time) the value of x_1 is such that the Gibbs free energy [Equation (6.1)] is minimized [31]. Equation (6.1) is also dependent on the binding energy of each site ϵ_1 and ϵ_2 as their value dictate the manner in which the Li sites in the sublattices are filled. Then, their ratio $\theta = \epsilon_1/\epsilon_2$ ($\theta \geq 1$) describes different scenarios with $\theta = 1$ being the case of an ideal solid solution. In this study, the value of ϵ_1 was taken as 0.2 eV and θ ranged from 1 to 10 which was consistent with the values obtained from DFT calculations reported in the literature for typical electrode materials [31, 168].

6.3 Materials and Methods

6.3.1 NVOPF synthesis

The hydrothermal method used to synthesize NVOPF was described in detail in Ref. [33] and need not be repeated. In brief, 100 mg of NH_4VO_3 (99.4 %, Sigma Aldrich), 100 mg of $NH_4H_2PO_4$ (Sigma Aldrich), and 50 mg of NaF (Sigma Aldrich) were dissolved in DI water at 60 °C in a 3:2:2:3 (Na:V:P:F) molar ratio. NVOPF *nanoparticles* were formed on reduced graphene oxide (r-GO) by adding 50 mg of GO (Ref. [120]) and 10 mL of ethanol (Sigma Aldrich) to the solution. The mixture was then stirred in a beaker using a magnetic stirrer for 10 minutes to insure a homogeneous mixture. For NVOPF *micronbricks*, 10 mL of ethanol was added to the solution without GO. Next, for both synthesis routes, 10 mL of N,N-dimethylformamide (DMF, Anhydrous, Sigma Aldrich) was added dropwise to the solution while stirring vigorously with a magnetic stirrer. Then, the solution was stirred for additional 30 minutes. Finally, the solution was transferred into a 45 mL Teflon liner and sealed in a stainless steel Parr bomb for heating. The *nanoparticles* were heated at 180 °C for 16 h and the *micronbricks* were heated at 140 °C for 40 h. Figure 6.1 shows the SEM images of (a) *micronbricks* and (b) *nanoparticles* powders as synthesized. The images establish that the *micronbricks* were larger and feature elongated particles on micron scale. Moreover, *nanoparticles* were smaller (i.e., sub micron) and did not exhibit any preferential growth direction.

6.3.2 Electrode fabrication and device assembly

NVOPF *nanoparticles* were mixed with either polyvinylidene fluoride (PVDF, Kynar HSV 900) or poly(3-hexylthiophene-2, 5-diyl)(P3HT, Sigma Aldrich) binder without any conductive additives in a 9:1 weight ratio using a pestle and mortar into a homogeneous slurry. Moreover, NVOPF *micronbricks* were hand mixed with carbon black SuperP (Sigma Aldrich) and P3HT binder (Sigma Aldrich) in a 8:1:1 weight ratio. The slurry with PVDF binder were mixed in N-Methyl-2-pyrrolidone (NMP, Anhydrous, Sigma Aldrich) with mass concen-

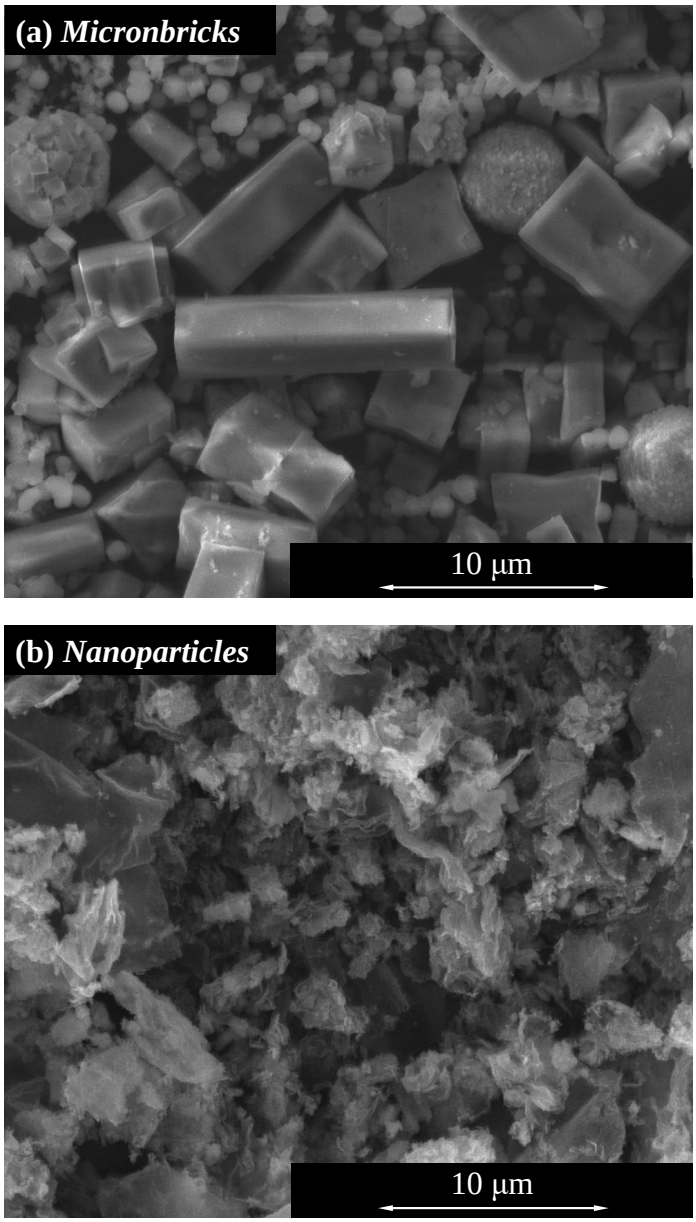

Figure 6.1: SEM images of (a) *micronbricks* and (b) *nanoparticles* powders as synthesized.

tration of 20 g/L. Moreover, the slurries with P3HT binder were mixed in o-Xylene (Sigma Aldrich) with a mass concentration of 10 g/L. Then, the electrodes were doctor bladed onto carbon-coated aluminum current collectors and left to dry on a hot plate at 40 °C before being transferred into a vacuum oven for storage at 120 °C. After drying, the electrodes were punched into discs 10 mm in diameter and assembled into 2032 coin cells using a coin

Table 6.1: Characteristics of the investigated coin cells.

Property/parameter	**Device 1**	**Device 2**	**Device 3**
LNVOPF particle size	*Micronbricks*	*Nanoparticles*	*Nanoparticles*
Binder	P3HT	P3HT	PVDF
LNVOPF mass loading, m_a (mg)	3.30	2.08	1.29

cell press (MTI) with a 260 μm thick glass fiber separator (GE) and Li-metal foil as a counter electrode. The coin cells were assembled in a glove box under Ar atmosphere and impregnated with 1 M $LiPF_6$ in a 1:1 mixture of ethylene carbonate (EC, Anhydrous, Sigma Aldrich) and dimethyl carbonate (DMC, Anhydrous, Sigma Aldrich). Table 6.1 summarizes the characteristics of the investigated batteries.

6.3.3 Lithium exchange cyclic voltammetry

The three coin cells were subjected to cyclic voltammetry for three cycles at scan rate ν of 0.1 mV/s and potential between $\psi_{s,min} = 3.0$ V and $\psi_{s,max} = 4.5$ V as recommended by Ref. [33]. This resulted in the electrochemical exchange of Na in NVOPF ($Na_{1.5}VOPO_4F_{0.5}$) with Li to form LNVOPF ($Li_xNa_{1.5-x}VOPO_4F_{0.5}$) as described in Ref. [33].

6.3.4 Entropic potential measurements

Entropic potential measurement consists of galvanostatic intermittent titration technique (GITT) with imposed step temperature changes to measure the open circuit voltage $U_{ocv}(x,T)$ change with respect to temperature T, termed entropic potential $\partial U_{ocv}(x,T)/\partial T$. During delithiation the current pulse of C/10 was applied for 30 minutes followed by a 4 hour relaxation period to allow for the potential to relax to its open circuit value (i.e., $\partial U_{ocv}(x,T)/\partial t <$ 1 mV/h [93,94]). During the last 30 minutes of the relaxation, a step function of temperature was imposed via a thermoelectric cold plate in increments of 5 °C, between 15 and 25 °C, for 10 minutes at each temperature. On the other hand, the current pulse during lithiation was

C/20 to ensure sufficient measurement resolution. It was also applied for 30 minutes followed by a 4 hour relaxation period with the same temperature variations as during delithiation. The measurements were then interpreted according to the guidelines established in Ref. [31].

6.4 Results and discussion

6.4.1 Calculations of the model

Figure 6.2 shows (a) the filling fraction of Li in the guest matrix x_v, (b) the entropy of Li_xMA electrode $s_{Li_xMA}(x,T)$, (c) the open circuit voltage of the battery cell $U_{ocv}(x,T)$, and (d) the entropic potential of the battery cell $\partial U_{ocv}(x,T)/\partial T$ as functions of the lithium composition x for θ ranging from 1 to 10. Figure 6.2(a) established a preferential delithiation of the lower binding energy sites (Li2) before the higher binding energy sites (Li1). The preference became more evident at larger value of θ. As Li2 sites became vacant (i.e., $x = 0.5$) ion ordering occurred. This could be observed as a dip in the entropy of the electrode $s_{Li_xMA}(x,T)$ [Figure 6.2(b)] due to a larger degree of order in the electrode. Here, the dip in $s_{Li_xMA}(x,T)$ gradually appeared and then became deeper as θ increased due to the increased ion ordering. Moreover, $U_{ocv}(x,T)$ curves [Figure 6.2(c)] initially overlapped before deviating from each other with increasing θ as the Li filling fractions x_v [Figure 6.2(a)] started to deviate from each other. Finally, the entropic potential of the battery cell $\partial U_{ocv}(x,T)/\partial T$ [Figure 6.2(d)] corresponding to $U_{ocv}(x,T)$ [Figure 6.2(c)] followed a tilde-shape centered around $x = 0.5$ typical for Li ordering between Li1 and Li2 sites [31]. The tilde-shape was not observed for $\theta = 1$, and became increasingly more visible as θ increased.

6.4.2 Lithium exchange

Figure 6.3 shows the cyclic voltammograms of the electrochemical Li exchange for three consecutive cycles for (a) Device 1, (b) Device 2, and (c) Device 3 for scan rate ν of 0.1 mV/s vs Li/Li^+. The potential vs. Li/Li^+ was confined between 3.0 and 4.5 V as recommended by Ref. [33]. Cyclic voltammograms indicated the shift of the redox peaks closer together typical

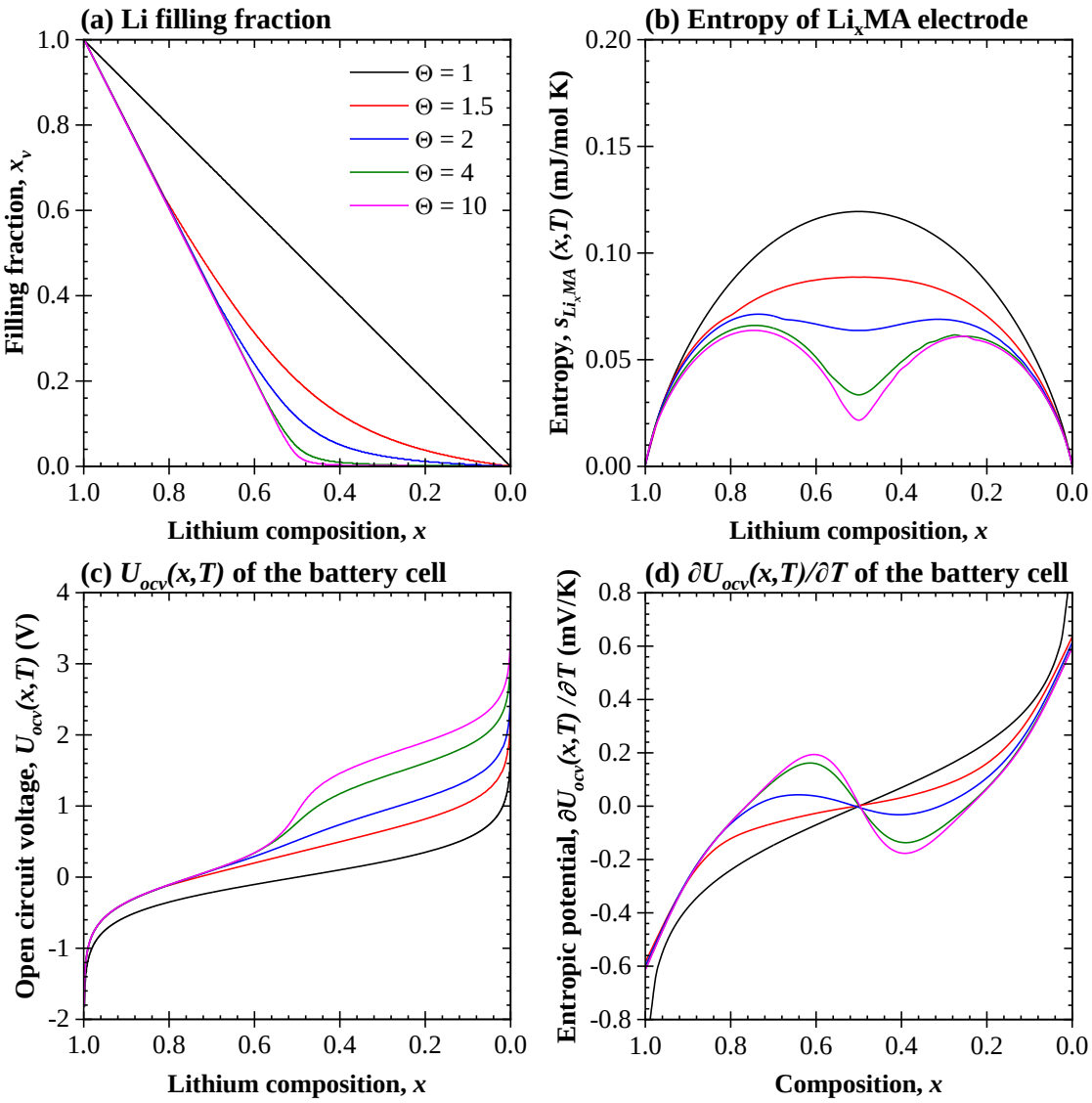

Figure 6.2: Calculated (a) Li vacant filling fraction x_v, (b) entropy of the Li_xMA electrode $s_{Li_xMA}(x,T)$, (c) open circuit voltage of the battery cell $U_{ocv}(x,T)$, and (d) entropic potential of the battery cell $\partial U_{ocv}(x,T)/\partial T$ for a range of binding energy ratios θ and as functions of lithium composition x.

of electrochemical exchange of Na with Li. Concretely, the redox peaks shifted to 3.85 V (Li2) and 4.15 V (Li1) typical of V^{5+}/V^{4+} redox in LNVOPF [33]. Moreover, the difference between cyclic voltammograms of the last two cycles was negligible and indicated the completion of Li exchange. Finally, Lai et al. [33] found that under the same CV conditions smaller amount of Na was substituted with Li in *micronbricks* compared to *nanoparticles* due to diffusion

limitations [33]. Therefore, Device 1 retained the most Na, followed by Device 2, while Device 3 retained the least Na after Li exchange.

6.4.3 GITT measurements

Figure 6.4 shows the GITT curves of (a, b, c) the delithiation at C/10, and (d, e, f) lithiation at C/20 for (a, d) Device 1, (b, e) Device 2, and (c, f) Device 3 as functions of gravimetric capacity C_g. The gravimetric capacity during delithiation was larger than lithiation in all devices. Moreover, the polarization was also larger during delithiation than lithiation indicating more sluggish Li diffusion. Furthermore, all devices featured two "faux plateaus" in $U_{ocv}(x,T)$ at 3.85 V and 4.15 V corresponding to V^{5+}/V^{4+} redox, respectively. The "faux plateaus" were consistent with redox peaks observed in Li exchange cyclic voltammograms [Figure 6.3] and data reported in Ref. [33]. Please note, that the increase of the slope of $U_{ocv}(x,T)$ was observed between the two "faux plateaus". Moreover, the larger gravimetric capacity of Device 1 was attributed to a larger electrical conductivity as carbon black was added to the slurry during electrode fabrication. On the other hand, *nanoparticles* were grown on reduced graphene oxide (r-GO) and contained less carbon than the *micronbricks* therefore Device 1 had larger gravimetric capacity than Device 2 and Device 3.

6.4.4 Entropic potential

Figure 6.5 shows the open circuit voltage of the cell $U_{ocv}(x,T)$ and the corresponding entropic potential $\partial U_{ocv}(x,T)/\partial T$ during (a, b, c) delithiation at of C/10, and (d, e, f) lithiation at C/20 for (a, d) Device 1, (b, e) Device 2, and (c, f) Device 3 as functions of gravimetric capacity C_g. The trends and magnitude of $U_{ocv}(x,T)$ and $\partial U_{ocv}(x,T)/\partial T$ were similar for all devices. During delithiation [Figure 6.5(a)-6.5(c)], $U_{ocv}(x,T)$ initially exhibited a "faux plateau" at 3.85 V while $\partial U_{ocv}(x,T)/\partial T$ increased linearly. As the delithiation progressed, the slope of $U_{ocv}(x,T)$ increased while $\partial U_{ocv}(x,T)/\partial T$ rapidly dropped. Finally, at the end of the delithiation, $U_{ocv}(x,T)$ exhibited another "faux plateau" at 4.15 V while $\partial U_{ocv}(x,T)/\partial T$ increased linearly. This behavior was attributed to ion ordering in solid solution with the

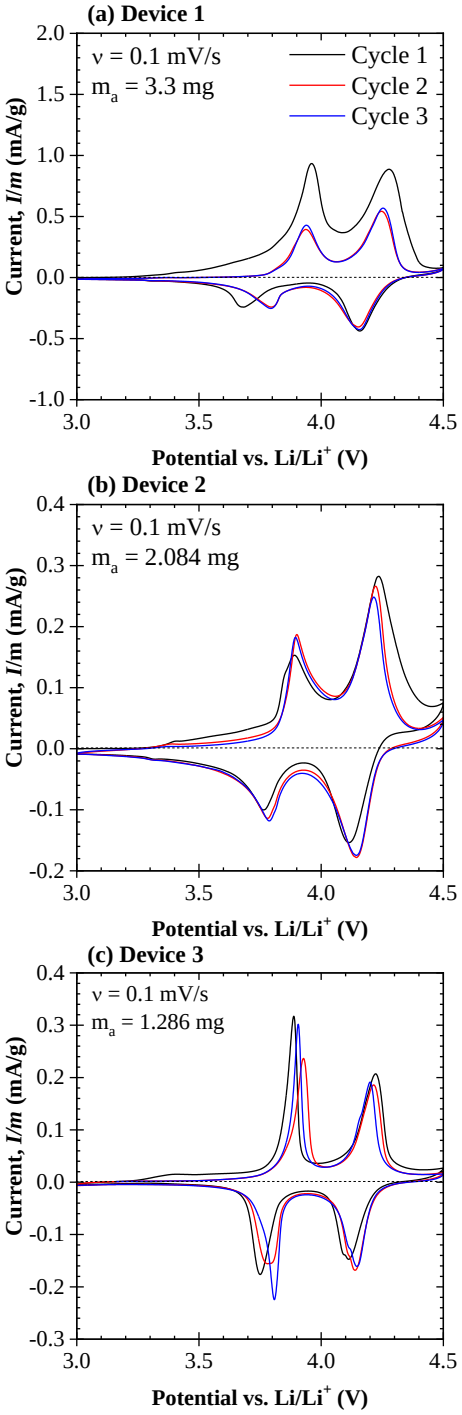

Figure 6.3: Cyclic voltammograms of the three electrochemical Li exchange cycles for (a) Device 1, (b) Device 2, and (c) Device 3 as functions of potential vs. Li/Li^+ for scan rate ν of 0.1 mV/s.

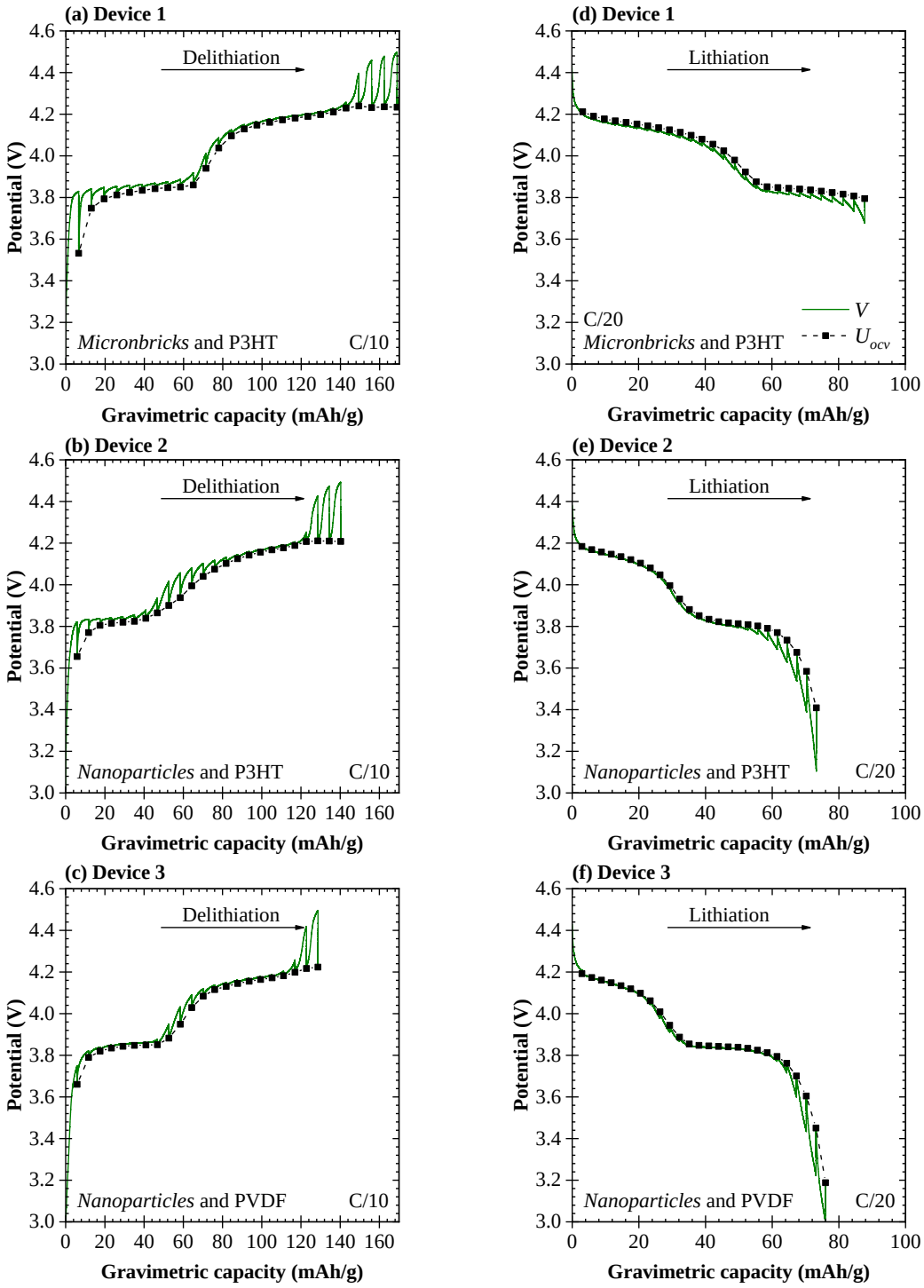

Figure 6.4: GITT curves of (a, b, c) Delithiation at C/10, and (d, e, f) lithiation at C/20 for (a, d) Device 1, (b, e) Device 2, and (c, f) Device 3 as functions of gravimetric capacity C_g.

first $U_{ocv}(x,T)$ "faux plateau" corresponding to the delithiation of Li2 sites and the second $U_{ocv}(x,T)$ "faux plateau" corresponding to the delithiation of Li1 sites. This was consistent with theoretical [31, 96, 97] and experimental [93, 94, 96, 97] studies of similar materials. During lithiation [Figure 6.5(d)-6.5(f)], $U_{ocv}(x,T)$ first exhibited a "faux plateau" at 4.15 V and $\partial U_{ocv}(x,T)/\partial T$ decreased linearly as Li intercalated into the electrode and lithiated Li1 sites. Then, $U_{ocv}(x,T)$ dropped rapidly while $\partial U_{ocv}(x,T)/\partial T$ rapidly increased as the intercalated Li ordered between Li1 and Li2 sites. Then, $U_{ocv}(x,T)$ settled at another "faux plateau" at 3.85 V while $\partial U_{ocv}(x,T)/\partial T$ linearly increased as Li2 sites were lithiated.

Moreover, Figure 6.6 shows the entropic potential $\partial U_{ocv}(x,T)/\partial T$ as a function of open circuit voltage $U_{ocv}(x,T)$ for all three devices during (a) delithiation at C/10 and (b) lithiation at C/20. During delithiation [Figure 6.6(a)] $\partial U_{ocv}(x,T)/\partial T$ vs. $U_{ocv}(x,T)$ curves overlapped throughout the entire cycle. This indicated that Li deintercalation and ordering was independent of (i) LNVOPF particle size, (ii) binder used, and (iii) conductive additives in the electrode. On the one hand, during lithiation [Figure 6.6(b)], $\partial U_{ocv}(x,T)/\partial T$ vs. $U_{ocv}(x,T)$ curves were in good agreement at lower $U_{ocv}(x,T)$ (between 3.75 and 4.0 V) when Li2 sites were lithiated. On the other hand, at higher $U_{ocv}(x,T)$ (between 4.0 and 4.2 V) a dip was observed in $\partial U_{ocv}(x,T)/\partial T$ which was the most shallow for Device 1 while it was the deepest for Device 3. Please note, that Device 1 retained the most while Device 3 retained the least Na in LNVOPF particles after Li exchange [33].

6.4.5 Apparent diffusion coefficient

Figure 6.7 shows the open circuit voltage of the cell $U_{ocv}(x,T)$ and the corresponding apparent diffusion coefficient of Li in the electrode D_{Li^+} during (a, b, c) delithiation at C/10, and (d, e, f) lithiation at C/20 for (a, d) Device 1, (b, e) Device 2, and (c, f) Device 3 as functions of gravimetric capacity C_g. The apparent diffusion coefficient of Li in the electrode D_{Li^+} featured similar trends for all devices during delithiation and lithiation. During delithiation [Figure 6.7(a)-6.7(c)], D_{Li^+} was initially high at the beginning of the lower "faux plateau" of $U_{ocv}(x,T) = 3.85$ V and then it decreased. This was attributed to the decreasing occupancy

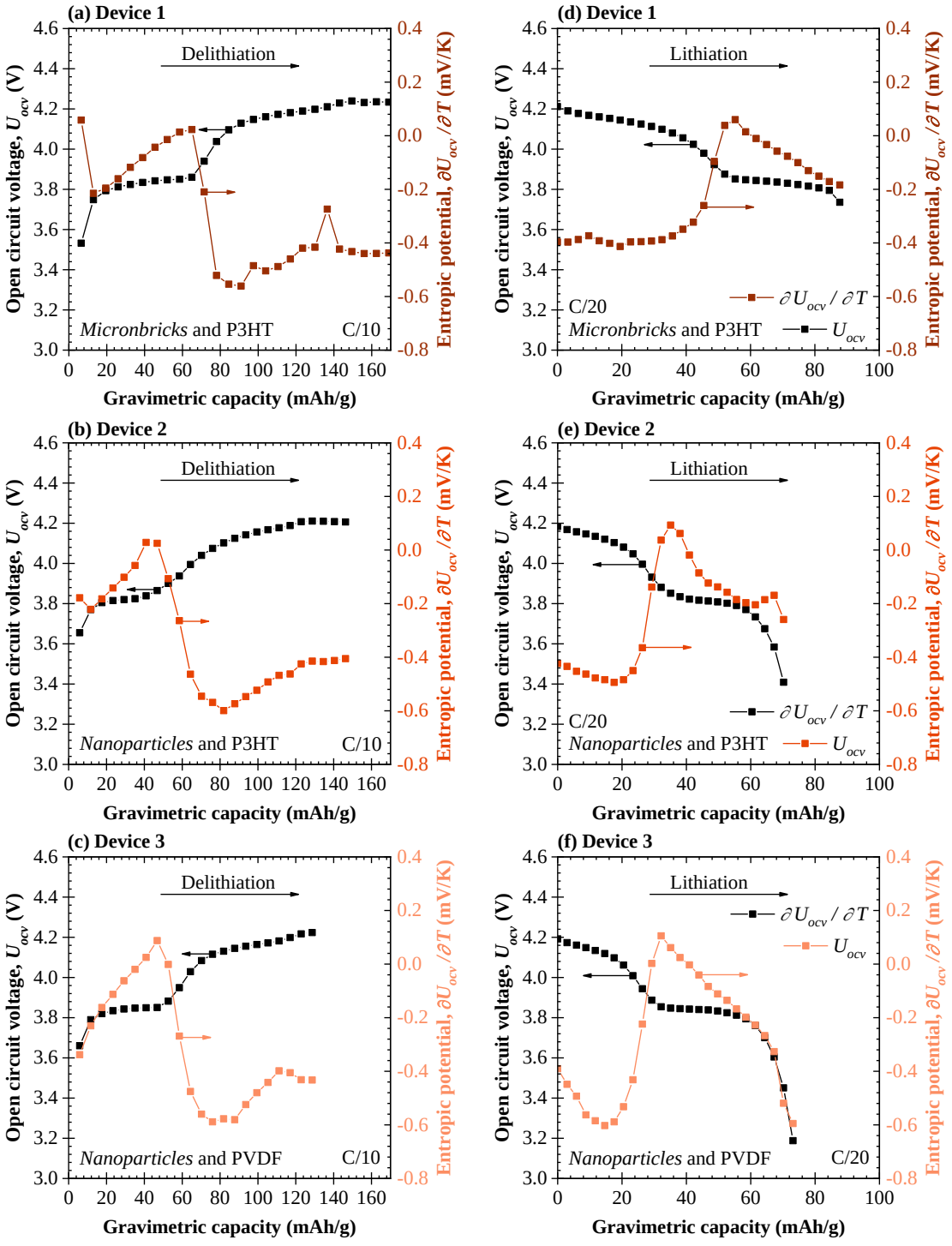

Figure 6.5: The open circuit voltage of the cell $U_{ocv}(x,T)$ and the corresponding entropic potential $\partial U_{ocv}(x,T)/\partial T$ during (a, b, c) delithiation at C/10, and (d, e, f) lithiation at C/20 for (a, d) Device 1, (b, e) Device 2, and (c, f) Device 3 as functions of gravimetric capacity C_g.

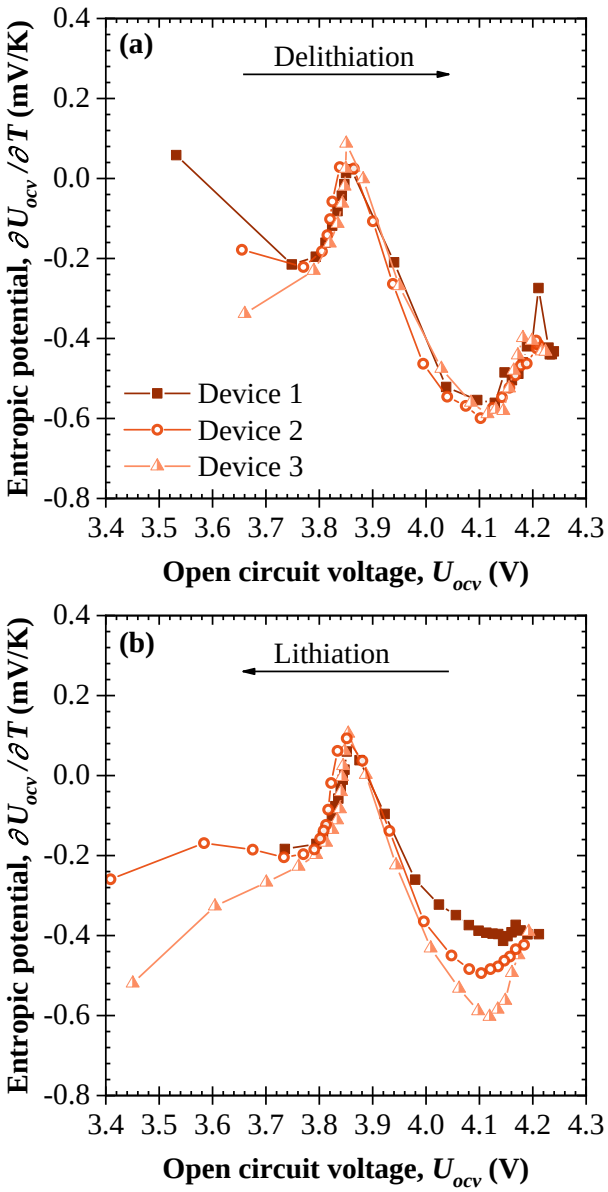

Figure 6.6: The entropic potential $\partial U_{ocv}(x,T)/\partial T$ as a function of open circuit voltage $U_{ocv}(x,T)$ for all three devices during (a) delithiation at C/10 and (b) lithiation at C/20.

of Li2 sites resulting in less diffusing Li as it deintercalated from the electrode into the electrolyte. As the slope of $U_{ocv}(x,T)$ increased, D_{Li^+} increased as Li in the lattice ordered between Li1 and Li2 sites. Then, at higher "faux plateau" of $U_{ocv(x,T)} = 4.15$ V, D_{Li^+} decreased again due to the decreasing occupancy of Li1 sites and decreasing amount of diffusing Li due to its continued deintercalation from the electrode into the electrolyte.

Moreover, during lithiation [Figure 6.7(d)-6.7(f)], D_{Li^+} exhibited two minima, corresponding to each U_{ocv} "faux plateau" possibly due to Coulombic interactions between guest-host and guest-guest ions as previously observed for $Li_xMn_2O_4$ spinel phase [169]. Indeed, even at low x compositions, Li ions are not isolated from each other due to the layered structure of LNVOPF. Moreover, between the two U_{ocv} "faux plateaus", Li ordering between Li1 and Li2 sites occurred and caused an increase in Li mobility and D_{Li^+}. Similar observation were reported for a $Li_{1-\delta}Mn_2O_4$ [97, 169].

Finally, Figure 6.8 shows the apparent diffusion coefficient of Li in the electrode D_{Li^+} as a function of open circuit voltage $U_{ocv}(x,T)$ for all three investigated devices during (a) delithiation at C/10 and (b) lithiation at C/20. In addition, Figure 6.8 also shows D_{Li^+} as a function of $U_{ocv}(x,T)$ extracted from Ref. [4] for LNVOPF with Li content $x = 0.4$. During the delithiation step [Figure6.8(a)] D_{Li^+} vs. $U_{ocv}(x,T)$ curves overlapped for all investigated devices. Here, D_{Li^+} decreased during the lower (i.e., 3.85 V) and higher (4.15 V) $U_{ocv}(x,T)$ "faux plateaus". This was attributed to delithiation of Li2 and Li1 sites in the lattice, respectively. On the other hand, during lithiation [Figure 6.8(b)] D_{Li^+} was the highest for Device 3 followed by Device 2, while it was the lowest for Device 1. Please note, that defects such as vacancies, dislocations, and impurities (i.e., residual Na ions) can irreversibly trap Li or block access to Li sites and transport paths in the LNVOPF particles [96, 97, 170]. In fact, D_{Li^+} decreased with increasing residual Na content of the electrode [i.e., $D_{Li^+}(\text{Device 1}) < D_{Li^+}(\text{Device 2}) < D_{Li^+}(\text{Device 3})$]. On the other hand, the dips in D_{Li^+} extracted from Ref. [4] were shifted to lower potentials. This was attributed to a lower concentration of the exchanged Li in the lattice ($x = 0.4$). Indeed, $U_{ocv}(x,T)$ at which the dips appeared shifted towards 3.7 V and 4.0 V. These values were associated with V^{5+}/V^{4+} redox in NVOPF electrodes [4].

Finally, the diminishing dip observed in $\partial U_{ocv}(x,T)/\partial T$ at the higher $U_{ocv}(x,T)$ "faux plateau" (i.e., 4.15 V) [Figure 6.6(b)] could be caused by the hindered Li transport [Figure 6.8(b)] due to the residual Na in the LNVOPF particles. Indeed, after Li exchange, Device 1 had the highest concentration of Na in the LNVOPF particles, followed by Device 2, while Device 3 had the lowest concentration of Na in the LNVOPF particles [33].

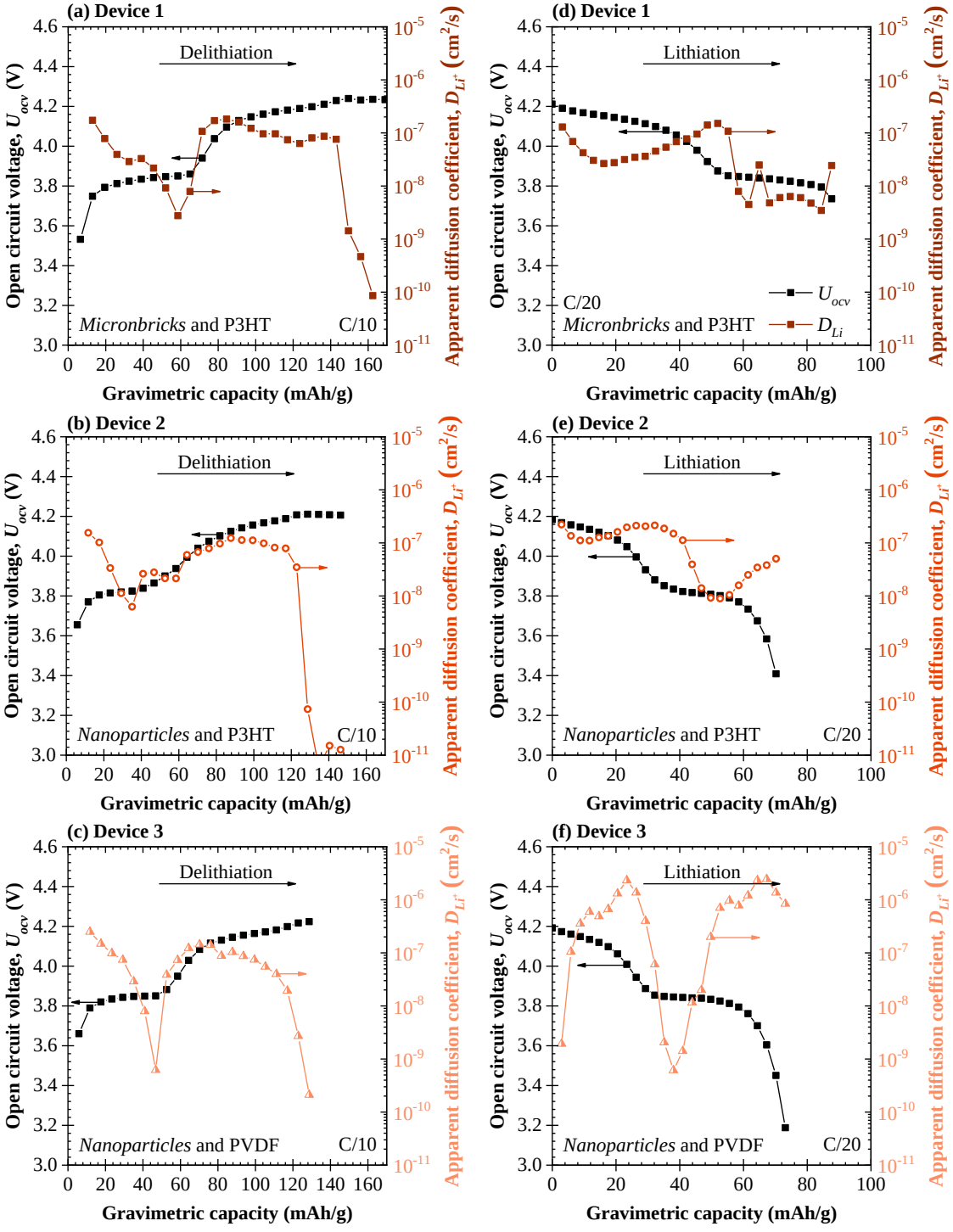

Figure 6.7: The open circuit voltage of the cell $U_{ocv}(x,T)$ and the corresponding apparent diffusion coefficient of Li in the electrode D_{Li^+} during (a, b, c) delithiation at C/10, and (d, e, f) lithiation at C/20 for (a, d) Device 1, (b, e) Device 2, and (c, f) Device 3 as functions of gravimetric capacity C_g.

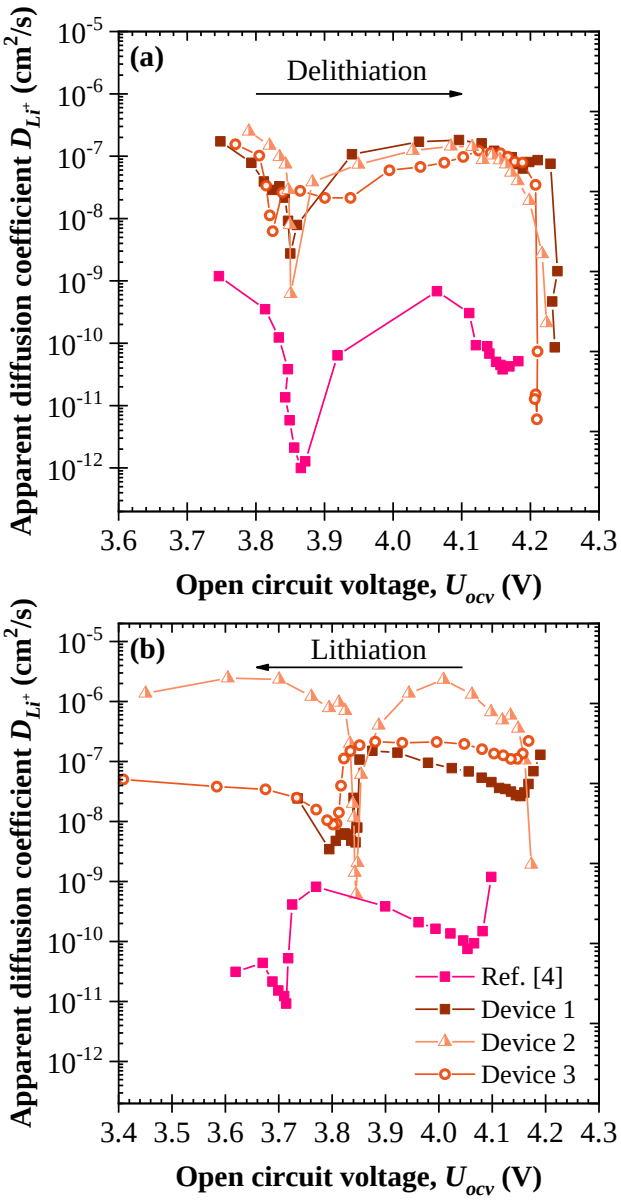

Figure 6.8: The apparent diffusion coefficient of Li^+ ions in the electrode D_{Li^+} as a function of open circuit voltage $U_{ocv}(x,T)$ for all three devices during (a) delithiation at C/10 and (b) lithiation at C/20. GITT current in data extracted from Ref. [4] was 0.13 A/g.

6.5 Conclusion

This study reported the open circuit voltage, entropic potential, and apparent diffusion coefficient of Li in $Li_xNa_{1.5-x}VOPO_4F_{0.5}$ (LNVOPF) for three different coin cells. Moreover, it also qualitatively compared the measured entropic potential with the one calculated for

a solid solution with ion ordering. Finally, it compared the apparent diffusion coefficient of Li in LNVOPF particles for Li content between 0.9 and 0.95 with the values reported in literature for the Li content of 0.4. The coin cells consisted of elemental Li anode and a LNVOPF based cathode of varying particles sizes with either P3HT or PVDF binder in 1 M $LiPF_6$ in EC:DMC electrolyte. Three LNVOPF cathodes were fabricated, namely (i) *micronbricks* with P3HT, (ii) *nanoparticles* with P3HT, and (iii) *nanoparticles* with PVDF. First, Li exchange was performed for each coin cell via cyclic voltammetry at scan rate $\nu =$ 0.1 mV/s and potential between 3.0 and 4.5 V vs. Li/Li^+. Then, GITT measurements with temperature control were performed at C/10 for delithiation and C/20 for lithiation. The results indicated that LNVOPF exhibited solid solution behavior with ion ordering during both lithiation and delithiation resulting in excellent high rate performance. Moreover, it established that the charging mechanism was independent of LNVOPF particle size and binder used. Furthermore, it was observed that the lower amount of exchanged Li hindered Li transport in LNVOPF particles. This was attributed to the residual Na irreversibly trapping Li and/or blocking Li sites and transport paths in LNVOPF particles.

CHAPTER 7

Conclusions and future work

7.1 Conclusions

The objectives of this study were (i) to investigate the effect of ion species on the operating potential window of hybrid supercapacitors with aqueous electrolytes, (ii) to identify the thermal signature of ion solvation during cycling, (iii) to investigate the effect of cation species on the charging mechanism of hybrid supercapacitors, (iv) to formulate and numerically compute the heat generation rates due to the charge and mass transfer resistances, and (v) to clarify the structural evolution of LNVOPF based cathodes during delithiation and lithiation. These objectives were set to advance the use of isothermal *operando* calorimetry as a diagnostic tool for hybrid supercapacitors and batteries. They were also selected to deepen the practical and theoretical understanding of kinetics and thermodynamics of electrodes used in high power density applications.

The first three objectives were achieved by using isothermal *operando* calorimetry of hybrid supercapacitors consisting of a positive α-MnO_2 electrode and an AC counter electrode immersed in aqueous electrolytes. The aqueous electrolytes investigated included (i) Li_2SO_4, (ii) Na_2SO_4, (iii) K_2SO_4, (iv) Cs_2SO_4, and (v) $MgSO_4$. They were chosen for their different ion sizes, valencies, and hydration enthalpy. Overall, the thermal signature at the AC electrodes was attributed to the EDL formation/dissolution. Concretely, the heat generation was exothermic during EDL formation and endothermic during EDL dissolution. However, for 0.5 M Li_2SO_4 aqueous electrolyte the endothermic heat generation measured at the AC electrode was attributed to the non-spontaneous redox reactions of Li wish AC electrode. On the other hand, the thermal signature at the α-MnO_2 was attributed to surface redox reac-

tions. It was endothermic when redox reactions were non-spontaneous and exothermic when they were spontaneous. It was found that for an aqueous K_2SO_4 and Cs_2SO_4 electrolyte, the onset of hydrolysis was delayed to a potential window of 1.8 V and 2.0 V, respectively, and exceeded the electrochemical stability window of water of 1.23 V. This was attributed to the thinner solvation shell surrounding Cs^+ cations compared to K^+ cations, thus limiting the amount of water near the electrode surface.

Furthermore, when ions are adsorbed or intercalated into the electrode they partially or fully shed their solvation shell. Then, the thermal signature of solvation/desolvation is proportional to the enthalpy of solvation and superimposed onto the thermal signature of other phenomena. However, solvation/desolvation has been difficult to distinguish from desorption/adsorption as the salts typically used in aqueous electrolytes have small enthalpy of solvation and the thermal signature is dominated by that of desorption/adsorption. In fact, it was found that in $MgSO_4$ aqueous electrolyte the thermal signature of ion solvation/desolvation dominated over the thermal signature of other phenomena occurring during cycling. Then, the heat generation rate measured at the α-MnO_2 electrodes was strictly positive and featured two different plateaus during charging and discharging, respectively.

The effect of ion size on the charging mechanisms in hybrid supercapacitors was investigated using (i) Li_2SO_4, (ii) Na_2SO_4, and (iii) Cs_2SO_4 aqueous electrolytes. The heat generation rates revealed that the smaller Li^+ cations possibly participated in non-spontaneous fast surface redox reactions at high potential at the AC electrode resulting in an endothermic thermal signature. This was not observed with larger Na^+ and Cs^+ cations as they did not undergo redox reactions.

The fourth objective was achieved by recognizing that heat generation rate due to the charge and mass transfer resistances could be formulated as resistive losses and expressed like Joule heating. It was found that both the charge and the mass transfer resistances were dependent on the state of charge of the electrode. Their temporal evolution was calculated under galvanostatic cycling for several current densities and added to the predicted Joule heating. The heat generation rates were averaged over the entire cycle and compared to the total time-averaged heat generation rate. Both methods yielded the same local heat

generation rate, thus confirming that the charge and mass transfer resistances contribute to the irreversible heat generation rate in addition to Joule heating.

The fifth objective was achieved by measuring the entropic potential evolution of LNVOPF cathodes made with different particle sizes and binders. Here, cathodes made of LNVOPF *micronbricks* and *nanoparticles* with either P3HT or PVDF binders were considered. They were assembled into coin cells with Li metal anode in 1 M $LiPF_6$ in EC:DMC electrolyte. The entropic potential evolution revealed that LNVOPF particles exhibited solid solution behavior with Li ion ordering between two Li sites which was corroborated by the results of a theoretical model of solid solution with ion ordering. Moreover, the charging mechanism was found to be independent of particle size and of the binder chosen. The apparent diffusion coefficient was the smallest for LNVOPF *micronbricks* with P3HT and the largest for LNVOPF *nanoparticles* with PVDF. Indeed, residual Na in LNVOPF particles could irreversibly trap Li in the lattice and block or obstruct Li sites and transport paths. By identifying the charging mechanism of LNVOPF the study connected solid solution behavior with ion ordering to the excellent rate performance and large capacity of LNVOPF cathodes.

7.2 Future work

7.2.1 Calorimetry of ECs with water-in-salt electrolytes ("WISE")

Calorimetric measurements presented in Chapter 2 demonstrate that a thinner solvation shell of cations results in the delayed onset of hydrolysis and the expansion of the operating potential window of hybrid supercapacitors by limiting the amount of solvent present at the electrode. However, the use of water-in-salt ("WISE") electrolyte can achieve the same result by limiting the overall amount of solvent in the electrolyte [124]. Therefore, future work should consider the use of isothermal *operando* calorimetry on hybrid supercapacitors with "WISE" electrolyte under galvanostatic cycling. The hybrid supercapacitor will consist of a positive α-MnO_2 electrode and an AC counter electrode separated by a mesh separator impregnated with a "WISE" electrolyte. The α-MnO_2 and AC electrodes are suggested

to enable direct comparison with the results reported in this study. The electrolyte can consist of an aqueous solution of LiTFSI with concentration of (i) 5 M, (ii) 10 M, (iii) 15 M, and (iv) 20 M and is suggested based on its high solubility in water. This study would provide additional understanding of the delay of hydrolysis attributed to the limited amount of solvent present in the electrolyte resulting in the expansion of the operating potential window.

7.2.2 Potentiometric study of LNVOPF at elevated temperatures

Chapter 6 clarified the structural evolution of LNVOPF and its excellent rate performance during cycling. It was found that for the entire composition range LNVOPF exhibits solid solution behavior with Li ion ordering. However, the literature suggests that cycling at elevated temperature can reduce ion ordering and promote solid solution behavior in $Li_xMn_2O_4$, $LiCoO_2$, and 2H-$LiTaS_2$ [96, 97, 171, 172]. In fact, increasing the temperature to 405 K for $Li_xMn_2O_4$ [96, 97], to 335 K for $LiCoO_2$ [171], and to 320 K for 2H-$LiTaS_2$ [172] completely suppressed ion ordering and the material exhibited purely solid solution behavior. Future work should investigate the effect of elevated temperature on the charging mechanism of LNVOPF. Elevated temperature could broaden the "faux plateaus" associated with solid solution behavior as the solubility of most solid and liquid solutions increases at elevated temperatures. Consequently, it could further improve the high rate capabilities of LNVOPF. However, the energy density might decrease at elevated temperature due to the reduced ion ordering.

7.2.3 Accounting for heating due to solvation in the MPNP model

The current thermal model accounts for the different contributions to the instantaneous heat generation rate in EDLCs and hybrid supercapacitors [75, 77]. It includes the reversible heat generation due to (i) ion adsorption/desorption and (ii) redox reactions at the pseudocapacitive electrode. It also accounts for the irreversible heat generation due to (i) Joule heating and (ii) redox reactions at the pseudocapacitive electrode [75, 77]. However, in its current

form, it does not account for the contributions of ion (partial) desolvation during ion adsorption or surface redox. Conversely, it does not account for ion (partial) solvation during ion desorption. Chapter 3 showed that in electrolytes with high enthalpy of solvation, such as aqueous $MgSO_4$, the thermal signature of solvation/desolvation can overshadow the thermal signature of other charging mechanisms. Moreover, due to the hysteretic concentration profile at the pseudocapacitive electrode, part of the heat generated due to solvation/desolvation may contribute to the irreversible heat generation rate analogous to that of charge and mass transfer resistances. Therefore, future work should focus on expanding the model for the local and time-dependent heat generation rate to include solvation/desolvation. To do so, the difference in ion size between solvated and bare ions must be modeled. Then, the heat generation rate released based on the enthalpy of solvation of the ions can be determined. Therefore, the process of solvation and desolvation must be studied in detail to determine how the ion size changes during this process.

APPENDIX A

Supplementary Material for Chapter 4

Three-electrode cyclic voltammograms

Figure A.1 shows the CV curves of AC and α-MnO_2 electrodes in a three-electrode setup measured at scan rate ν of 10 mV/s in (a) 0.25 M, (b) 0.75 M, and (c) 1.0 M $MgSO_4$ aqueous electrolyte, respectively. The potential window for AC electrodes ranged between -0.8 V and 0 V and between 0 V and 0.8 V for α-MnO_2 electrodes, both vs. $Ag^+/AgCl$.

Full device cyclic voltammograms

Figure A.2 shows the measured CV curves for (a) Device 1, (b) Device 2, and (c) Device 3, for scan rate ν between 5 and 50 mV/s and a cell potential window $\Delta\psi_s = 1.6$ V imposed at the α-MnO_2 electrode vs. the AC electrode. First, for any given scan rate ν and cell potential $\psi_s(t)$, the magnitude of the current response $I(t)$ increased with increasing $MgSO_4$ concentration thanks to the larger amount of ions contributing to charge storage. Similarly, for all devices, the magnitude of the current response $I(t)$ increased and the CV curves changed from a rectangular to a leaf-like shape with increasing scan rate ν.

Modeled heat generation contributions

Figure A.3 shows the predicted instantaneous heat generation rate $\dot{Q}_i(t)$ and its contributions at (a) an AC electrode, and an α-MnO_2 electrode in (b) $MgSO_4$ and (c) Cs_2SO_4 aqueous electrolytes as functions of dimensionless time t/t_{cd}. Both $\dot{Q}_{T,AC}(t)$ and $\dot{Q}_{T,MnO_2}(t)$ were qualitatively similar to heat generation rates in Devices 1, 2, and 3. Moreover, $\dot{Q}_{T,MnO_2}(t)$ was dominated by the large enthalpy of solvation in $MgSO_4$ aqueous electrolyte [Figure

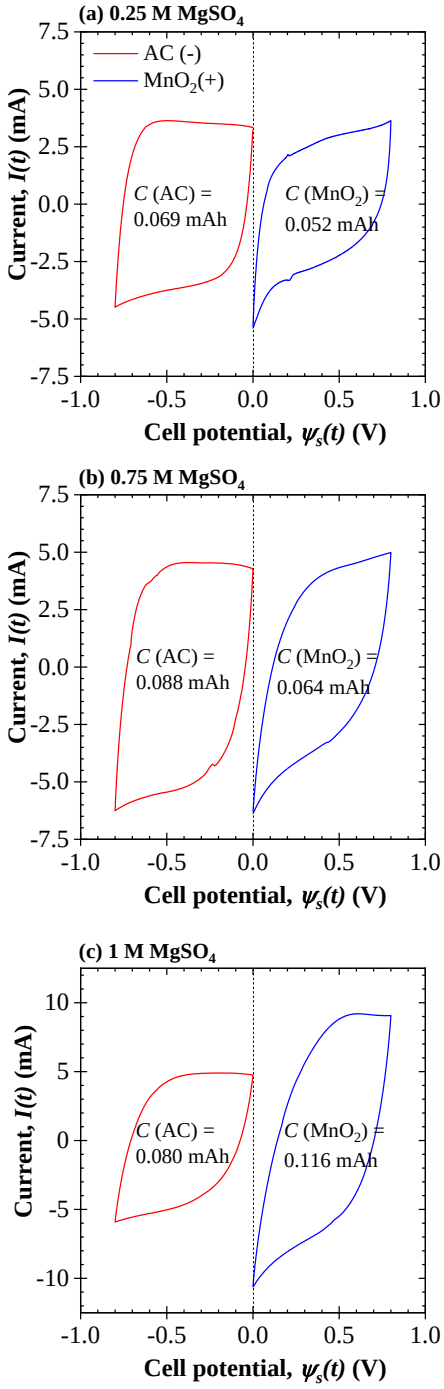

Figure A.1: CV curves of AC and α-MnO_2 electrodes in a three-electrode setup measured at scan rate ν of 10 mV/s in (a) 0.25 M, (b) 0.75 M, and (c) 1.0 M $MgSO_4$ aqueous electrolyte, respectively, and potential window between -0.8 and 0 V for AC and 0 V and 0.8 V for α-MnO_2 electrodes.

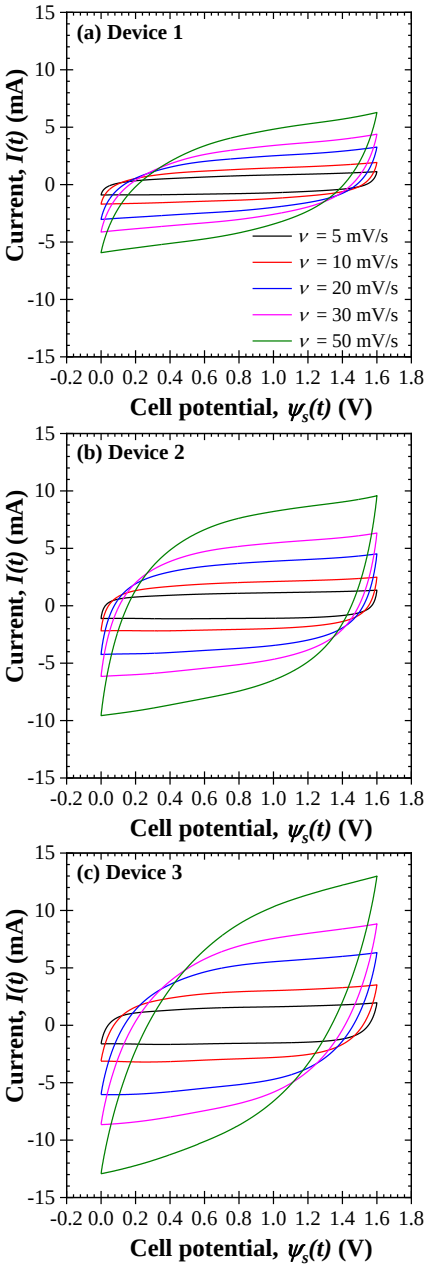

Figure A.2: CV curves measured at different scan rates ν ranging between 5 and 50 mV/s for (a) Device 1, (b) Device 2, and (c) Device 3, and for potential window between 0 and 1.6 V.

A.3(b)]. Interestingly, $\dot{Q}_{T,MnO_2}(t)$ was dominated by ion adsorption/desorption and surface redox in aqueous Cs_2SO_4 electrolyte [Figure A.3(c)].

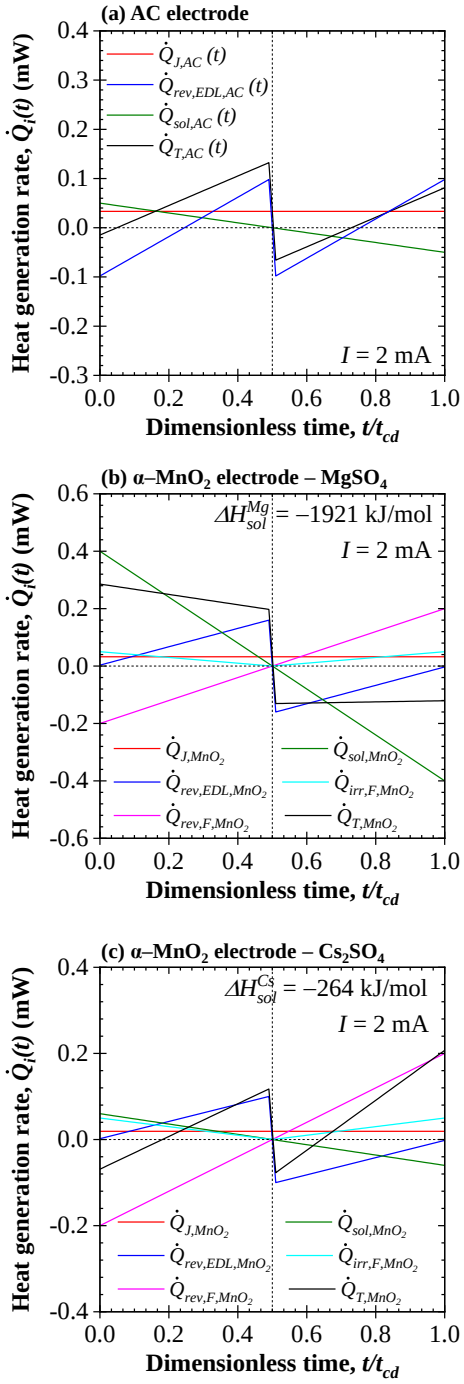

Figure A.3: Predicted instantaneous heat generation rate $\dot{Q}_i(t)$ and its contributions at (a) an AC electrode and an α-MnO_2 electrode in (b) $MgSO_4$ and (c) Cs_2SO_4 aqueous electrolytes as functions of dimensionless time t/t_{cd}.

References

[1] B.-A. Mei, O. Munteshari, J. Lau, B. Dunn, and L. Pilon, "Physical interpretations of Nyquist plots for EDLC electrodes and devices", *The Journal of Physical Chemistry C*, vol. 122, no. 1, pp. 194–206, 2018.

[2] M. Frajnkovič, A. Likitchatchawankun, C. Douard, Y. Zhou, S. W. Baek, I. Catton, O. Crosnier, T. Brousse, and L. Pilon, "Calorimetry can detect the early onset of hydrolysis in hybrid supercapacitors with aqueous electrolytes", *Journal of Power Sources*, vol. 548, pp. 232069, 2022.

[3] H.-L. Girard, B. Dunn, and L. Pilon, "Simulations and interpretation of three-electrode cyclic voltammograms of pseudocapacitive electrodes", *Electrochimica Acta*, vol. 211, pp. 420–429, 2016.

[4] J.-Z. Guo, Y. Yang, D.-S. Liu, X.-L. Wu, B.-H. Hou, W.-L. Pang, K.-C. Huang, J.-P. Zhang, and Z.-M. Su, "A practicable Li/Na-ion hybrid full battery assembled by a high-voltage cathode and commercial graphite anode: Superior energy storage performance and working mechanism", *Advanced Energy Materials*, vol. 8, no. 10, pp. 1702504, 2018.

[5] B. Conway, *Electrochemical Supercapacitors: Scientific Fundamentals and Technological Applications*, Kluwer Academic/Plenum, New York, NY, 1999.

[6] P. Guillemet, Y. Scudeller, and T. Brousse, "Multi-level reduced-order thermal modeling of electrochemical capacitors", *Journal of Power Sources*, vol. 157, no. 1, pp. 630–640, 2006.

[7] J. R. Miller, "Electrochemical capacitor thermal management issues at high-rate cycling", *Electrochimica Acta*, vol. 52, no. 4, pp. 1703–1708, 2006.

[8] A. Burke, "Ultracapacitors: why, how, and where is the technology", *Journal of Power Sources*, vol. 91, no. 1, pp. 37–50, 2000.

[9] A. Burke, "R&D considerations for the performance and application of electrochemical capacitors", *Electrochimica Acta*, vol. 53, no. 3, pp. 1083–1091, 2007.

[10] J. Miller and A. Burke, "Electrochemical capacitors: Challenges and opportunities for real-world applications", *Electrochemical Society Interface*, vol. 17, no. 1, pp. 53–57, 2008.

[11] M. Winter and R. J. Brodd, "What are batteries, fuel cells, and supercapacitors?", *Chemical Reviews*, vol. 104, no. 10, pp. 4245–4270, 2004.

[12] P. Simon, Y. Gogotsi, and B. Dunn, "Where do batteries end and supercapacitors begin?", *Science*, vol. 343, no. 6176, pp. 1210–1211, 2014.

[13] F. Béguin and E. Frackowiak, Ed., Supercapacitors: Materials, Systems and Applications, Wiley-VCH, Weinheim, Germany, 2013.

[14] US Department of Energy, Basic Research Needs for Electrical Energy Storage: Report of the Basic Energy Sciences Workshop on Electrical Energy Storage, www.osti.gov/accomplishments/documents/fullText/ACC0330.pdf.

[15] B. E. Conway, V. Birss, and J. Wojtowicz, "The role and utilization of pseudocapacitance for energy storage by supercapacitors", *Journal of Power Sources*, vol. 66, no. 1-2, pp. 1–14, 1997.

[16] M. R. Lukatskaya, B. Dunn, and Y. Gogotsi, "Multidimensional materials and device architectures for future hybrid energy storage", *Nature Communications*, vol. 7, no. 1, 2016.

[17] M. Toupin, T. Brousse, and D. Bélanger, "Charge storage mechanism of MnO_2 electrode used in aqueous electrochemical capacitor", *Chemistry of Materials*, vol. 16, no. 16, pp. 3184–3190, 2004.

[18] Y. Zhu, L. Peng, D. Chen, and G. Yu, "Intercalation pseudocapacitance in ultrathin $VOPO_4$ nanosheets: Toward high-rate alkali-ion-based electrochemical energy storage", *Nano Letters*, vol. 16, no. 1, pp. 742–747, 2015.

[19] S.-B. Ma, K.-Y. Ahn, E.-S. Lee, K.-H. Oh, and K.-B. Kim, "Synthesis and characterization of manganese dioxide spontaneously coated on carbon nanotubes", *Carbon*, vol. 45, no. 2, pp. 375–382, 2007.

[20] D. Choi, G. E. Blomgren, and P. N. Kumta, "Fast and reversible surface redox reaction in nanocrystalline vanadium nitride supercapacitors", *Advanced Materials*, vol. 18, no. 9, pp. 1178–1182, 2006.

[21] J. R. Miller and P. Simon, "Electrochemical capacitors for energy management", *Science*, vol. 321, no. 5889, pp. 651–652, 2008.

[22] W. Sugimoto, T. Kizaki, K. Yokoshima, Y. Murakami, and Y. Takasu, "Evaluation of the pseudocapacitance in RuO_2 with a RuO_2/GC thin film electrode", *Electrochimica Acta*, vol. 49, no. 2, pp. 313–320, 2004.

[23] V. Augustyn, J. Come, M. A. Lowe, J. W. Kim, P.-L. Taberna, S. H. Tolbert, H. D. Abruna, P. Simon, and B. Dunn, "High-rate electrochemical energy storage through Li^+ intercalation pseudocapacitance", *Nature Materials*, vol. 12, no. 6, pp. 518–522, 2013.

[24] O. Munteshari, J. Lau, A. Likitchatchawankun, B.-A. Mei, C. S. Choi, D. Butts, B. Dunn, and L. Pilon, "Thermal signature of ion intercalation and surface redox reactions mechanisms in model pseudocapacitive electrodes", *Electrochimica Acta*, vol. 307, pp. 512–524, 2019.

[25] J. W. Long, B. Dunn, D. R. Rolison, and H. S. White, "Three-dimensional battery architectures", *Chemical Reviews*, vol. 104, no. 10, pp. 4463–4492, 2004.

[26] J. A. Rogers, "Electronics for the human body", *JAMA*, vol. 313, no. 6, pp. 561, 2015.

[27] H. Nishide and K. Oyaizu, "Toward flexible batteries", *Science*, vol. 319, no. 5864, pp. 737–738, 2008.

[28] A. Meintz, J. Zhang, R. Vijayagopal, C. Kreutzer, S. Ahmed, I. Bloom, A. Burnham, R. B. Carlson, F. Dias, E. J. Dufek, J. Francfort, K. Hardy, A. N. Jansen, M. Keyser, A. Markel, C. Michelbacher, M. Mohanpurkar, A. Pesaran, D. Scoffield, M. Shirk, T. Stephens, and T. Tanim, "Enabling fast charging - vehicle considerations", *Journal of Power Sources*, vol. 367, pp. 216–227, 2017.

[29] M. Walter, M. V. Kovalenko, and K. V. Kravchyk, "Challenges and benefits of post-lithium-ion batteries", *New Journal of Chemistry*, vol. 44, no. 5, pp. 1677–1683, 2020.

[30] B. Guo, X. Yu, X.-G. Sun, M. Chi, Z.-A. Qiao, J. Liu, Y.-S. Hu, X.-Q. Yang, J. B. Goodenough, and S. Dai, "A long-life lithium-ion battery with a highly porous $TiNb_2O_7$ anode for large-scale electrical energy storage", *Energy & Environmental Science*, vol. 7, no. 7, pp. 2220–2226, 2014.

[31] S. W. Baek, M. Saber, A. Van der Ven, and L. Pilon, "Thermodynamic analysis and interpretative guide to entropic potential measurements of lithium-ion battery electrodes", *The Journal of Physical Chemistry C*, vol. 126, no. 14, pp. 6096–6110, 2022.

[32] D. Chao, C.-H. (M.) Lai, P. Liang, Q. Wei, Y.-S. Wang, C. (R.) Zhu, G. Deng, V. V. T. Doan-Nguyen, J. Lin, L. Mai, H. J. Fan, B. Dunn, and Z. X. Shen, "Sodium vanadium fluorophosphates (NVOPF) array cathode designed for high-rate full sodium ion storage device", *Advanced Energy Materials*, vol. 8, no. 16, pp. 1800058, 2018.

[33] C.-H. (M.) Lai, D. Ashby, N. H. Bashian, J. Schoiber, T.-C. Liu, G. Lee, S.-Y. Chen, P.-W. Wu, B. C. Melot, and B. Dunn, "Designing the charge storage properties of Li-exchanged sodium vanadium fluorophosphate for powering implantable biomedical devices", *Advanced Energy Materials*, vol. 9, no. 18, pp. 1900226, 2019.

[34] Z. Zhao, S. Hao, P. Hao, Y. Sang, A. Manivannan, N. Wu, and H. Liu, "Lignosulphonate-cellulose derived porous activated carbon for supercapacitor electrode", *Journal of Materials Chemistry A*, vol. 3, no. 29, pp. 15049–15056, 2015.

[35] B. Zhang, J. Liang, C. L. Xu, B. Q. Wei, D. B. Ruan, and D. H. Wu, "Electric double-layer capacitors using carbon nanotube electrodes and organic electrolyte", *Materials Letters*, vol. 51, no. 6, pp. 539–542, 2001.

[36] K. L. Van Aken, C. R. Pérez, Y. Oh, M. Beidaghi, Y. J. Jeong, M. F. Islam, and Y. Gogotsi, "High rate capacitive performance of single-walled carbon nanotube aerogels", *Nano Energy*, vol. 15, pp. 662–669, 2015.

[37] H.-J. Liu, W.-J. Cui, L.-H. Jin, C.-X. Wang, and Y.-Y. Xia, "Preparation of three-dimensional ordered mesoporous carbon sphere arrays by a two-step templating route and their application for supercapacitors", *Journal of Materials Chemistry*, vol. 19, no. 22, pp. 3661, 2009.

[38] V. Augustyn, P. Simon, and B. Dunn, "Pseudocapacitive oxide materials for high-rate electrochemical energy storage", *Energy & Environmental Science*, vol. 7, no. 5, pp. 1597–1614, 2014.

[39] T. Brousse, D. Belanger, K. Chiba, M. Egashira, F. Favier, J. Long, J. R. Miller, M. Morita, P. Simon K. Naoi, and W. Sugimoto, *Springer Handbook of Electrochemical Energy*, chapter 16: Materials for electrochemical capacitors, pp. 495–561, Springer, Heidelberg, Germany, 2017.

[40] G. A. Snook, P. Kao, and A. S. Best, "Conducting-polymer-based supercapacitor devices and electrodes", *Journal of Power Sources*, vol. 196, no. 1, pp. 1–12, 2011.

[41] Q. Li, X.-F. Lu, H. Xu, Y.-X. Tong, and G.-R. Li, "Carbon/MnO_2 double-walled nanotube arrays with fast ion and electron transmission for high-performance supercapacitors", *ACS Applied Materials & Interfaces*, vol. 6, no. 4, pp. 2726–2733, 2014.

[42] Z. Lei, F. Shi, and L. Lu, "Incorporation of MnO_2-coated carbon nanotubes between graphene sheets as supercapacitor electrode", *ACS Applied Materials & Interfaces*, vol. 4, no. 2, pp. 1058–1064, 2012.

[43] S. W. Lee, J. Kim, S. Chen, P. T. Hammond, and Y. Shao-Horn, "Carbon nanotube/manganese oxide ultrathin film electrodes for electrochemical capacitors", *ACS Nano*, vol. 4, no. 7, pp. 3889–3896, 2010.

[44] P. Yang, Y. Ding, Z. Lin, Z. Chen, Y. Li, P. Qiang, M. Ebrahimi, W. Mai, C. P. Wong, and Z. L. Wang, "Low-cost high-performance solid-state asymmetric supercapacitors based on MnO_2 nanowires and Fe_2O_3 nanotubes", *Nano Letters*, vol. 14, no. 2, pp. 731–736, 2014.

[45] M. S. Whittingham, "Electrical energy storage and intercalation chemistry", *Science*, vol. 192, no. 4244, pp. 1126–1127, 1976.

[46] J. O. Besenhard, "The electrochemical preparation and properties of ionic alkali metal- and NR4-graphite intercalation compounds in organic electrolytes", *Carbon*, vol. 14, no. 2, pp. 111–115, 1976.

[47] K. Mizushima, P. C. Jones, P. J. Wiseman, and J. B. Goodenough, "Li_xCoO_2 (0<x<-1): A new cathode material for batteries of high energy density", *Materials Research Bulletin*, vol. 15, no. 6, pp. 783–789, 1980.

[48] H. Zhang, Y. Yang, D. Ren, L. Wang, and X. He, "Graphite as anode materials: Fundamental mechanism, recent progress and advances", *Energy Storage Materials*, vol. 36, pp. 147–170, 2021.

[49] J. Asenbauer, T. Eisenmann, M. Kuenzel, A. Kazzazi, Z. Chen, and D. Bresser, "The success story of graphite as a lithium-ion anode material – fundamentals, remaining challenges, and recent developments including silicon (oxide) composites", *Sustainable Energy & Fuels*, vol. 4, no. 11, pp. 5387–5416, 2020.

[50] T.-H. Park, J.-S. Yeo, M.-H. Seo, J. Miyawaki, I. Mochida, and S.-H. Yoon, "Enhancing the rate performance of graphite anodes through addition of natural graphite/carbon nanofibers in lithium-ion batteries", *Electrochimica Acta*, vol. 93, pp. 236–240, 2013.

[51] K. Ise, S. Morimoto, Y. Harada, and N. Takami, "Large lithium storage in highly crystalline $TiNb_2O_7$ nanoparticles synthesized by a hydrothermal method as anodes for lithium-ion batteries", *Solid State Ionics*, vol. 320, pp. 7–15, 2018.

[52] Z. Zhu, S. Tang, J. Yuan, X. Qin, Y. Deng, R. Qu, and G. M. Haarberg, "Effects of various binders on supercapacitor performances", *International Journal of Electrochemical Science*, pp. 8270–8279, 2016.

[53] N. Böckenfeld, S. S. Jeong, M. Winter, S. Passerini, and A. Balducci, "Natural, cheap and environmentally friendly binder for supercapacitors", *Journal of Power Sources*, vol. 221, pp. 14–20, 2013.

[54] J. Gamby, P. L. Taberna, P. Simon, J. F. Fauvarque, and M. Chesneau, "Studies and characterisations of various activated carbons used for carbon/carbon supercapacitors", *Journal of Power Sources*, vol. 101, no. 1, pp. 109–116, 2001.

[55] Q. T. Qu, B. Wang, L. C. Yang, Y. Shi, S. Tian, and Y. P. Wu, "Study on electrochemical performance of activated carbon in aqueous Li_2SO_4, Na_2SO_4 and K_2SO_4 electrolytes", *Electrochemistry Communications*, vol. 10, no. 10, pp. 1652–1655, 2008.

[56] B. Wei, J. C. Tokash, G. Chen, M. A. Hickner, and B. E. Logan, "Development and evaluation of carbon and binder loading in low-cost activated carbon cathodes for air-cathode microbial fuel cells", *RSC Advances*, vol. 2, no. 33, pp. 12751–12758, 2012.

[57] Q. Gao, L. Demarconnay, E. Raymundo-Piñero, and F. Béguin, "Exploring the large voltage range of carbon/carbon supercapacitors in aqueous lithium sulfate electrolyte", *Energy & Environmental Science*, vol. 5, no. 11, pp. 9611, 2012.

[58] T. Osaka, X. Liu, M. Nojima, and T. Momma, "An electrochemical double layer capacitor using an activated carbon electrode with gel electrolyte binder", *Journal of The Electrochemical Society*, vol. 146, no. 5, pp. 1724–1729, 1999.

[59] M. P. Bichat, E. Raymundo-Piñero, and F. Béguin, "High voltage supercapacitor built with seaweed carbons in neutral aqueous electrolyte", *Carbon*, vol. 48, no. 15, pp. 4351–4361, 2010.

[60] L. Demarconnay, E. Raymundo-Piñero, and F. Béguin, "A symmetric carbon/carbon supercapacitor operating at 1.6 V by using a neutral aqueous solution", *Electrochemistry Communications*, vol. 12, no. 10, pp. 1275–1278, 2010.

[61] O. Munteshari, J. Lau, D. S. Ashby, B. Dunn, and L. Pilon, "Effects of constituent materials on heat generation in individual EDLC electrodes", *Journal of The Electrochemical Society*, vol. 165, no. 7, pp. A1547–A1557, 2018.

[62] A. G. Pandolfo, G. J. Wilson, T. D. Huynh, and A. F. Hollenkamp, "The influence of conductive additives and inter-particle voids in carbon EDLC electrodes", *Fuel Cells*, vol. 10, no. 5, pp. 856–864, 2010.

[63] D. Weingarth, D. Cericola, F. C. F. Mornaghini, T. Hucke, and R. Kötz, "Carbon additives for electrical double layer capacitor electrodes", *Journal of Power Sources*, vol. 266, pp. 475–480, 2014.

[64] Y. Qiu, X. Zhang, and S. Yang, "High performance supercapacitors based on highly conductive nitrogen-doped graphene sheets", *Physical Chemistry Chemical Physics*, vol. 13, no. 27, pp. 12554, 2011.

[65] K. Zhang, L. Mao, L. L. Zhang, H. S. O. Chan, X. S. Zhao, and J. Wu, "Surfactant-intercalated, chemically reduced graphene oxide for high performance supercapacitor electrodes", *Journal of Materials Chemistry*, vol. 21, no. 20, pp. 7302, 2011.

[66] M. R. Bailey, J. A. Denman, and S. W. Donne, "Electrode additives and the rechargeability of the alkaline manganese dioxide cathode", *Journal of The Electrochemical Society*, vol. 161, no. 3, pp. A403–A409, 2014.

[67] C.-C. Ji, M.-W. Xu, S.-J. Bao, C.-J. Cai, R.-Y. Wang, and D.-Z. Jia, "Effect of alkaline and alkaline–earth cations on the supercapacitor performance of MnO_2 with various crystallographic structures", *Journal of Solid State Electrochemistry*, vol. 17, no. 5, pp. 1357–1368, 2013.

[68] J. Shin, J. K. Seo, R. Yaylian, A. Huang, and Y. S. Meng, "A review on mechanistic understanding of MnO_2 in aqueous electrolyte for electrical energy storage systems", *International Materials Reviews*, vol. 65, no. 6, pp. 356–387, 2019.

[69] S. Devaraj and N. Munichandraiah, "Effect of crystallographic structure of MnO_2 on its electrochemical capacitance properties", *The Journal of Physical Chemistry C*, vol. 112, no. 11, pp. 4406–4417, 2008.

[70] A. Boisset, L. Athouël, J. Jacquemin, P. Porion, T. Brousse, and M. Anouti, "Comparative performances of birnessite and cryptomelane MnO_2 as electrode material in neutral aqueous lithium salt for supercapacitor application", *The Journal of Physical Chemistry C*, vol. 117, no. 15, pp. 7408–7422, 2013.

[71] L. L. Zhang and X. S. Zhao, "Carbon-based materials as supercapacitor electrodes", *Chemical Society Reviews*, vol. 38, no. 9, pp. 2520–2531, 2009.

[72] E. Frackowiak, "Carbon materials for supercapacitor application", *Physical Chemistry Chemical Physics*, vol. 9, no. 15, pp. 1774, 2007.

[73] R.-S. Kühnel and A. Balducci, "Lithium ion transport and solvation in n-butyl-n-methylpyrrolidinium bis(trifluoromethanesulfonyl)imide–propylene carbonate mixtures", *The Journal of Physical Chemistry C*, vol. 118, no. 11, pp. 5742–5748, 2014.

[74] M. Salanne, "Ionic liquids for supercapacitor applications", *Topics in Current Chemistry*, vol. 375, no. 3, 2017.

[75] A. L. d'Entremont and L. Pilon, "First-principles thermal modeling of electric double layer capacitors under constant-current cycling", *Journal of Power Sources*, vol. 246, pp. 887–898, 2014.

[76] A. L. d'Entremont, H.-L. Girard, H. Wang, and L. Pilon, "Electrochemical transport phenomena in hybrid pseudocapacitors under galvanostatic cycling", *Journal of The Electrochemical Society*, vol. 163, no. 2, pp. A229–A243, 2015.

[77] A. L. d'Entremont and L. Pilon, "First-principles thermal modeling of hybrid pseudocapacitors under galvanostatic cycling", *Journal of Power Sources*, vol. 335, pp. 172–188, 2016.

[78] A. Burke and M. Miller, "Testing of electrochemical capacitors: Capacitance, resistance, energy density, and power capability", *Electrochimica Acta*, vol. 55, no. 25, pp. 7538–7548, 2010.

[79] S. Zhao, F. Wu, L. Yang, L. Gao, and A. Burke, "A measurement method for determination of DC internal resistance of batteries and supercapacitors", *Electrochemistry Communications*, vol. 12, no. 2, pp. 242–245, 2010.

[80] M. D. Stoller and R. S. Ruoff, "Best practice methods for determining an electrode material's performance for ultracapacitors", *Energy & Environmental Science*, vol. 3, no. 9, pp. 1294–1301, 2010.

[81] H. Wang, A. Thiele, and L. Pilon, "Simulations of cyclic voltammetry for electric double layers in asymmetric electrolytes: A generalized modified Poisson-Nernst-Planck model", *The Journal of Physical Chemistry C*, vol. 117, no. 36, pp. 18286–18297, 2013.

[82] H. Wang and L. Pilon, "Reply to comments on "intrinsic limitations of impedance measurements in determining electric double layer capacitances" by H. Wang, L. Pilon [Electrochimica Acta 63 (2012) 55]", *Electrochimica Acta*, vol. 76, pp. 529–531, 2012.

[83] C. Song, H. Wang, X.-Z. Yuan, and J. Zhang, *Electrochemical Impedance Spectroscopy in PEM Fuel Cells*, Springer-Verlag, Heidelberg, Germany, 2009.

[84] D. Pech, M. Brunet, H. Durou, P. Huang, V. M., Y. Gogotsi, P.-L. Taberna, and P. Simon, "Ultrahigh-power micrometre-sized supercapacitors based on onion-like carbon", *Nature Nanotechnology*, vol. 5, no. 9, pp. 651–654, 2010.

[85] H. Itoi, H. Nishihara, T. Kogure, and T. Kyotani, "Three-dimensionally arrayed and mutually connected 1.2-nm nanopores for high-performance electric double layer capacitor", *Journal of the American Chemical Society*, vol. 133, no. 5, pp. 1165–1167, 2011.

[86] A. J. Bard and L. R. Faulkner, *Electrochemical Methods: Fundamentals and Applications*, John Wiley & Sons, New York, NY, 2000.

[87] A. Lasia, *Electrochemical Impedance Spectroscopy and its Applications*, Springer-Verlag, Heidelberg, Germany, 2014.

[88] M. E. Orazem and B. Tribollet, *Electrochemical Impedance Spectroscopy*, Wiley-Interscience, Hoboken, NJ, 2008.

[89] B.-A. Mei, J. Lau, T. Lin, S. H. Tolbert, B. Dunn, and L. Pilon, "Physical interpretations of electrochemical impedance spectroscopy of redox active electrodes for electrical energy storage", *The Journal of Physical Chemistry C*, vol. 122, no. 43, pp. 24499–24511, 2018.

[90] W. Weppner and R. A. Huggins, "Determination of the kinetic parameters of mixed-conducting electrodes and application to the system Li_3Sb", *Journal of The Electrochemical Society*, vol. 124, no. 10, pp. 1569–1578, 1977.

[91] C. J. Wen, "Thermodynamic and mass transport properties of "LiAl"", *Journal of The Electrochemical Society*, vol. 126, no. 12, pp. 2258, 1979.

[92] A. Van der Ven, "Lithium diffusion in layered Li_xCoO_2", *Electrochemical and Solid-State Letters*, vol. 3, no. 7, pp. 301, 1999.

[93] S. W. Baek, M. B. Preefer, M. Saber, K. Zhai, M. Frajnkovič, Y. Zhou, B. S. Dunn, A. Van der Ven, R. Seshadri, and L. Pilon, "Potentiometric entropy and *operando* calorimetric measurements reveal fast charging mechanisms in PNb_9O_{25}", *Journal of Power Sources*, vol. 520, pp. 230776, 2022.

[94] S. W. Baek, K. E. Wyckoff, D. M. Butts, J. Bienz, A. Likitchatchawankun, M. B. Preefer, M. Frajnkovič, B. S. Dunn, R. Seshadri, and L. Pilon, "Operando calorimetry informs the origin of rapid rate performance in microwave-prepared $TiNb_2O_7$ electrodes", *Journal of Power Sources*, vol. 490, pp. 229537, 2021.

[95] J. R. Dahn and R. R. Haering, "Entropy measurements on Li_xTiS_2", *Canadian Journal of Physics*, vol. 61, no. 7, pp. 1093–1098, 1983.

[96] S.-I. Pyun and S.-W. Kim, "Thermodynamic approach to electrochemical lithium intercalation into $Li_{1-\delta}Mn_2O_4$ electrode prepared by sol-gel method", *Molecular Crystals and Liquid Crystals Science and Technology. Section A. Molecular Crystals and Liquid Crystals*, vol. 341, no. 2, pp. 155–162, 2000.

[97] S.-W. Kim and S.-I. Pyun, "Thermodynamic and kinetic approaches to lithium intercalation into a $Li_{1-\delta}Mn_2O_4$ electrode using Monte Carlo simulation", *Electrochimica Acta*, vol. 46, no. 7, pp. 987–997, 2001.

[98] Y. Dandeville, P. Guillemet, Y. Scudeller, O. Crosnier, L. Athouël, and T. Brousse, "Measuring time-dependent heat profiles of aqueous electrochemical capacitors under cycling", *Thermochimica Acta*, vol. 526, no. 1-2, pp. 1–8, 2011.

[99] O. Munteshari, J. Lau, A. Krishnan, B. Dunn, and L. Pilon, "Isothermal calorimeter for measurements of time-dependent heat generation rate in individual supercapacitor electrodes", *Journal of Power Sources*, vol. 374, pp. 257–268, 2018.

[100] A. Likitchatchawankun, G. Whang, J. Lau, O. Munteshari, B. Dunn, and L. Pilon, "Effect of temperature on irreversible and reversible heat generation rates in ionic liquid-based electric double layer capacitors", *Electrochimica Acta*, vol. 338, pp. 135802, 2020.

[101] A. Likitchatchawankun, R. H. DeBlock, G. Whang, O. Munteshari, M. Frajnkovič, B. Dunn, and L. Pilon, "Heat generation in electric double layer capacitors with neat and diluted ionic liquid electrolytes under large potential window between 5 and 80 °C", *Journal of Power Sources*, vol. 488, 229368, 2021.

[102] O. Munteshari, A. Borenstein, R. H. DeBlock, J. Lau, G. Whang, Y. Zhou, A. Likitchatchawankun, R. B. Kaner, B. Dunn, and L. Pilon, "*In Operando* calorimetric measurements for activated carbon electrodes in ionic liquid electrolytes under large potential windows", *ChemSusChem*, vol. 13, no. 5, pp. 1013–1026, 2020.

[103] L. H. Hess, A. Bothe, and A. Balducci, "Design and use of a novel in situ simultaneous thermal analysis cell for an accurate "Real time" monitoring of the heat and weight changes occurring in electrochemical capacitors", *Energy Technology*, vol. 9, no. 9, pp. 2100329, 2021.

[104] A. Likitchatchawankun, A. Kundu, O. Munteshari, T. S. Fisher, and L. Pilon, "Heat generation in all-solid-state supercapacitors with graphene electrodes and gel electrolytes", *Electrochimica Acta*, vol. 303, pp. 341–353, 2019.

[105] J. Schiffer, D. Linzen, and D. U. Sauer, "Heat generation in double layer capacitors", *Journal of Power Sources*, vol. 160, no. 1, pp. 765–772, 2006.

[106] M. F. Dupont, M. Forghani, A. P. Cameron, and S. W. Donne, "Effect of electrolyte cation on the charge storage mechanism of manganese dioxide for electrochemical capacitors", *Electrochimica Acta*, vol. 271, pp. 337–350, 2018.

[107] M. S. Hong, S. H. Lee, and S. W. Kim, "Use of KCl aqueous electrolyte for 2 V manganese oxide/activated carbon hybrid capacitor", *Electrochemical and Solid-State Letters*, vol. 5, no. 10, pp. A227–A230, 2002.

[108] A. Hauch, S. D. Ebbesen, S. H. Jensen, and M. Mogensen, "Highly efficient high temperature electrolysis", *Journal of Materials Chemistry*, vol. 18, no. 20, pp. 2331, 2008.

[109] C. Douard, L. Athouël, D. Brown, O. Crosnier, G. Rebmann, O. Schilling, and T. Brousse, "Electrode design for MnO_2-based aqueous electrochemical capacitors: Influence of porosity and mass loading", *Materials*, vol. 14, no. 11, pp. 2990–3009, 2021.

[110] R. D. Shannon, "Revised effective ionic radii and systematic studies of interatomic distances in halides and chalcogenides", *Acta Crystallographica Section A*, vol. 32, no. 5, pp. 751–767, 1976.

[111] J. Mähler and I. Persson, "A study of the hydration of the alkali metal ions in aqueous solution", *Inorganic Chemistry*, vol. 51, no. 1, pp. 425–438, 2011.

[112] T. Brousse, D. Bélanger, and J. W. Long, "To be or not to be pseudocapacitive?", *Journal of The Electrochemical Society*, vol. 162, no. 5, pp. A5185–A5189, 2015.

[113] Y. Marcus, "Ionic radii in aqueous solutions", *Chemical Reviews*, vol. 88, no. 8, pp. 1475–1498, 1988.

[114] A. M. Friedman and J. W. Kennedy, "The self-diffusion coefficients of potassium, cesium, iodide and chloride ions in aqueous solutions", *Journal of the American Chemical Society*, vol. 77, no. 17, pp. 4499–4501, 1955.

[115] K. Tanaka, "Measurements of tracer diffusion coefficients of sulphate ions in aqueous solutions of ammonium sulphate and sodium sulphate, and of water in aqueous sodium sulphate solutions", *Journal of the Chemical Society, Faraday Transactions 1*, vol. 84, no. 8, pp. 2895–2897, 1988.

[116] D. W. Smith, "Ionic hydration enthalpies", *Journal of Chemical Education*, vol. 54, no. 9, pp. 540–542, 1977.

[117] Y. Cheng, H. Zhang, S. Lu, C. V. Varanasi, and J. Liu, "Flexible asymmetric supercapacitors with high energy and high power density in aqueous electrolytes", *Nanoscale*, vol. 5, no. 3, pp. 1067–1073, 2013.

[118] S. M. H. Hashemi, P. Karnakov, P. Hadikhani, E. Chinello, S. Litvinov, C. Moser, P. Koumoutsakos, and D. Psaltis, "A versatile and membrane-less electrochemical reactor for the electrolysis of water and brine", *Energy & Environmental Science*, vol. 12, no. 5, pp. 1592–1604, 2019.

[119] H.-S. Kim, J. B. Cook, S. H. Tolbert, and B. Dunn, "The development of pseudocapacitive properties in nanosized-MoO_2", *Journal of The Electrochemical Society*, vol. 162, no. 5, pp. A5083–A5090, 2015.

[120] C.-H. Lai, D. Ashby, M. Moz, Y. Gogotsi, L. Pilon, and B. Dunn, "Designing pseudocapacitance for Nb_2O_5/carbide-derived carbon electrodes and hybrid devices", *Langmuir*, vol. 33, no. 37, pp. 9407–9415, 2017.

[121] H. Wang and L. Pilon, "Physical interpretation of cyclic voltammetry for measuring electric double layer capacitances", *Electrochimica Acta*, vol. 64, pp. 130–139, 2012.

[122] H. Dotan, A. Landman, S. W. Sheehan, K. D. Malviya, G. E. Shter, D. A. Grave, Z. Arzi, N. Yehudai, M. Halabi, N. Gal, N. Hadari, C. Cohen, A. Rothschild, and G. S. Grader, "Decoupled hydrogen and oxygen evolution by a two-step electrochemical–chemical cycle for efficient overall water splitting", *Nature Energy*, vol. 4, no. 9, pp. 786–795, 2019.

[123] J. Rumble, *CRC Handbook of Chemistry and Physics*, CRC Press/Taylor & Francis, Boca Raton, FL, 2020.

[124] L. Suo, O. Borodin, T. Gao, M. Olguin, J. Ho, X. Fan, C. Luo, C. Wang, and K. Xu, ""Water-in-salt" electrolyte enables high-voltage aqueous lithium-ion chemistries", *Science*, vol. 350, no. 6263, pp. 938–943, 2015.

[125] Y. Marcus, *Ions in Solution and their Solvation*, John Wiley & Sons, Hoboken, NJ, 2015.

[126] Y. Marcus, "Concentration dependence of ionic hydration numbers", *The Journal of Physical Chemistry B*, vol. 118, no. 35, pp. 10471–10476, 2014.

[127] H. S. Harned and R. M. Hudson, "The diffusion coefficient of magnesium sulfate in dilute aqueous solution at 25°", *Journal of the American Chemical Society*, vol. 73, no. 12, pp. 5880–5882, 1951.

[128] J. Zheng, G. Tan, P. Shan, T. Liu, J. Hu, Y. Feng, L. Yang, M. Zhang, Z. Chen, Y. Lin, J. Lu, J. C. Neuefeind, Y. Ren, K. Amine, L.-W. Wang, K. Xu, and F. Pan, "Understanding thermodynamic and kinetic contributions in expanding the stability window of aqueous electrolytes", *Chem*, vol. 4, no. 12, pp. 2872–2882, 2018.

[129] A. Platek-Mielczarek, E. Frackowiak, and K. Fic, "Specific carbon/iodide interactions in electrochemical capacitors monitored by EQCM technique", *Energy & Environmental Science*, vol. 14, no. 4, pp. 2381–2393, 2021.

[130] L. Qing, T. Long, H. Yu, Y. Li, W. Tang, B. Bao, and S. Zhao, "Quantifying ion desolvation effects on capacitances of nanoporous electrodes with liquid electrolytes", *Chemical Engineering Science*, vol. 240, pp. 116662, 2021.

[131] A. Berrueta, A. Ursua, I. San Martin, A. Eftekhari, and P. Sanchis, "Supercapacitors: Electrical characteristics, modeling, applications, and future trends", *IEEE Access*, vol. 7, pp. 50869–50896, 2019.

[132] P. Srimuk, J. Lee, Ö. Budak, J. Choi, M. Chen, G. Feng, C. Prehal, and V. Presser, "In situ tracking of partial sodium desolvation of materials with capacitive, pseudocapacitive, and battery-like charge/discharge behavior in aqueous electrolytes", *Langmuir*, vol. 34, no. 44, pp. 13132–13143, 2018.

[133] J. Chmiola, C. Largeot, P.-L. Taberna, P. Simon, and Y. Gogotsi, "Desolvation of ions in subnanometer pores and its effect on capacitance and double-layer theory", *Angewandte Chemie International Edition*, vol. 47, no. 18, pp. 3392–3395, 2008.

[134] W.-Y. Tsai, P.-L. Taberna, and P. Simon, "Electrochemical quartz crystal microbalance (EQCM) study of ion dynamics in nanoporous carbons", *Journal of the American Chemical Society*, vol. 136, no. 24, pp. 8722–8728, 2014.

[135] A. Likitchatchawankun, A. Kundu, O. Munteshari, T. S. Fisher, and L. Pilon, "Heat generation in all-solid-state supercapacitors with graphene electrodes and gel electrolytes", *Electrochimica Acta*, vol. 303, pp. 341–353, 2019.

[136] H.-L. Girard, H. Wang, A. L. d'Entremont, and L. Pilon, "Physical interpretation of cyclic voltammetry for hybrid pseudocapacitors", *The Journal of Physical Chemistry C*, vol. 119, no. 21, pp. 11349–11361, 2015.

[137] J. H. Masliyah and S. Bhattacharjee, *Electrokinetic and Colloid Transport Phenomena*, John Wiley & Sons, New York, NY, 2005.

[138] J. Come, V. Augustyn, J. W. Kim, P. Rozier, P.-L. Taberna, P. Gogotsi, J. W. Long, B. Dunn, and P. Simon, "Electrochemical kinetics of nanostructured Nb_2O_5 electrodes", *Journal of The Electrochemical Society*, vol. 161, no. 5, pp. A718–A725, 2014.

[139] L. Højgaard Olesen, M. Z. Bazant, and H. Bruus, "Strongly nonlinear dynamics of electrolytes in large AC voltages", *Physical Review E*, vol. 82, no. 1, pp. 011501, 2010.

[140] H. Wang and L. Pilon, "Intrinsic limitations of impedance measurements in determining electric double layer capacitances", *Electrochimica Acta*, vol. 63, pp. 55–63, 2012.

[141] M. S. Kilic, M. Z. Bazant, and A. Ajdari, "Steric effects in the dynamics of electrolytes at large applied voltages. II. Modified Poisson-Nernst-Planck equations", *Physical Review E*, vol. 75, no. 2, pp. 021503, 2007.

[142] M. Z. Bazant, M. S. Kilic, B. D. Storey, and A. Ajdari, "Towards an understanding of induced-charge electrokinetics at large applied voltages in concentrated solutions", *Advances in Colloid and Interface Science*, vol. 152, no. 1-2, pp. 48–88, 2009.

[143] F. P. Incropera, D. P. DeWitt, T. L. Bergman, and A. S. Lavine, *Fundamentals of Heat and Mass Transfer: 6^{th} edition*, John Wiley & Sons, Hoboken, NJ, 2006.

[144] R. B. Bird, W. E. Stewart, and E. N. Lightfoot, *Transport Phenomena*, John Wiley & Sons, Hoboken, NJ, 2006.

[145] Y.-H. Chen, C.-W. Wang, X. Zhang, and A.M. Sastry, "Porous cathode optimization for lithium cells: Ionic and electronic conductivity, capacity, and selection of materials", *Journal of Power Sources*, vol. 195, no. 9, pp. 2851–2862, 2010.

[146] A. M. Colclasure and R. J. Kee, "Thermodynamically consistent modeling of elementary electrochemistry in lithium-ion batteries", *Electrochimica Acta*, vol. 55, no. 28, pp. 8960–8973, 2010.

[147] C.-Y. Wang, "Fundamental models for fuel cell engineering", *Chemical Reviews*, vol. 104, no. 10, pp. 4727–4766, 2004.

[148] T. Berning, D. M. Lu, and N. Djilali, "Three-dimensional computational analysis of transport phenomena in a PEM fuel cell", *Journal of Power Sources*, vol. 106, no. 1-2, pp. 284–294, 2002.

[149] A. L. d'Entremont and L. Pilon, "Thermal effects of asymmetric electrolytes in electric double layer capacitors", *Journal of Power Sources*, vol. 273, pp. 196–209, 2015.

[150] J. S. Newman and K. E. Thomas-Alyea, *Electrochemical Systems*, Wiley John & Sons Ltd., Hoboken, NJ, 2004.

[151] R. F. Probstein, *Physicochemical Hydrodynamics: An Introduction, 2nd edition*, John Wiley & Sons, Hoboken, NJ, 2003.

[152] R. J. Hunter, *Foundations of Colloid Science*, Oxford University Press, Oxford, UK, 2001.

[153] G. J. Janz and R. P. T. Tomkins, *Nonaqueous Electrolytes Handbook. Vol. 1.*, Academic Press, New York, NY, 1972.

[154] R. N. De Guzman, A. Awaluddin, Y.-F. Shen, Z. R. Tian, S. L. Suib, S. Ching, and C.-L. O'Young, "Electrical resistivity measurements on manganese oxides with layer and tunnel structures: Birnessites, todorokites, and cryptomelanes", *Chemistry of Materials*, vol. 7, no. 7, pp. 1286–1292, 1995.

[155] K. Nishikawa, Y. Fukunaka, T. Sakka, Y. H. Ogata, and J. R. Selman, "Measurement of $LiClO_4$ diffusion coefficient in propylene carbonate by Moire pattern", *Journal of The Electrochemical Society*, vol. 153, no. 5, pp. A830, 2006.

[156] P. Guillemet, T. Brousse, O. Crosnier, Y. Dandeville, L. Athouël, and Y. Scudeller, "Modeling pseudo capacitance of manganese dioxide", *Electrochimica Acta*, vol. 67, pp. 41–49, 2012.

[157] Y. Xu, Q. Wei, C. Xu, Q. Li, Q. An, P. Zhang, J. Sheng, L. Zhou, and L. Mai, "Layer-by-layer $Na_3V_2(PO_4)_3$ embedded in reduced graphene oxide as superior rate and ultralong-life sodium-ion battery cathode", *Advanced Energy Materials*, vol. 6, no. 14, pp. 1600389, 2016.

[158] R. A. Shakoor, D.-H. Seo, H. Kim, Y.-U. Park, J. Kim, S.-W. Kim, H. Gwon, S. Lee, and K. Kang, "A combined first principles and experimental study on $Na_3V_2(PO_4)_2F_3$ for rechargeable Na batteries", *Journal of Materials Chemistry*, vol. 22, no. 38, pp. 20535, 2012.

[159] W. Massa, O. V. Yakubovich, and O. V. Dimitrova, "Crystal structure of a new sodium vanadyl(IV) fluoride phosphate $Na_3V_2O_2F[PO_4]_2$", *Solid State Sciences*, vol. 4, no. 4, pp. 495–501, 2002.

[160] W. Song, X. Ji, C. Pan, Y. Zhu, Q. Chen, and C. E. Banks, "A $Na_3V_2(PO_4)_3$ cathode material for use in hybrid lithium ion batteries", *Physical Chemistry Chemical Physics*, vol. 15, no. 34, pp. 14357, 2013.

[161] Y.-U. Park, D.-H. Seo, B. Kim, K.-P. Hong, H. Kim, S. Lee, R. A. Shakoor, K. Miyasaka, J.-M. Tarascon, and K. Kang, "Tailoring a fluorophosphate as a novel 4 V cathode for lithium-ion batteries", *Scientific Reports*, vol. 2, no. 1, 2012.

[162] N. V. Kosova, D. O. Rezepova, S. A. Petrov, and A. B. Slobodyuk, "Electrochemical and chemical Na^+/Li^+ ion exchange in Na-based cathode materials: $Na_{1.56}Fe_{1.22}P_2O_7$ and $Na_3V_2(PO_4)_2F_3$", *Journal of The Electrochemical Society*, vol. 164, no. 1, pp. A6192–A6200, 2016.

[163] N. Kosova and D. Rezepova, "$Na_{1+y}VPO_4F_{1+y}$ ($0 \leq y \leq 0.5$) as cathode materials for hybrid Na/Li batteries", *Inorganics*, vol. 5, no. 2, pp. 19, 2017.

[164] M. Xu, P. Xiao, S. Stauffer, J. Song, G. Henkelman, and J. B. Goodenough, "Theoretical and experimental study of vanadium-based fluorophosphate cathodes for rechargeable batteries", *Chemistry of Materials*, vol. 26, no. 10, pp. 3089–3097, 2014.

[165] Y.-U. Park, J. Bai, L. Wang, G. Yoon, W. Zhang, H. Kim, S. Lee, S.-W. Kim, J. P. Looney, K. Kang, and F. Wang, "*In Situ* tracking kinetic pathways of Li^+/Na^+ substitution during ion-exchange synthesis of $Li_xNa_{1.5-x}VOPO_4F_{0.5}$", *Journal of the American Chemical Society*, vol. 139, no. 36, pp. 12504–12516, 2017.

[166] W. Lu, I. Belharouak, J. Liu, and K. Amine, "Thermal properties of $Li_{4/3}Ti_{5/3}O_4/LiMn_2O_4$ cell", *Journal of Power Sources*, vol. 174, no. 2, pp. 673–677, 2007.

[167] J. Jiang, W. Shi, J. Zheng, P. Zuo, J. Xiao, X. Chen, W. Xu, and J.-G. Zhang, "Optimized operating range for large-format $LiFePO_4$/graphite batteries", *Journal of The Electrochemical Society*, vol. 161, no. 3, pp. A336–A341, 2013.

[168] M. Saber, M. B. Preefer, S. K. Kolli, W. Zhang, G. Laurita, B. Dunn, R. Seshadri, and A. Van der Ven, "Role of electronic structure in Li ordering and chemical strain in the fast charging Wadsley-Roth phase PNb_9O_{25}", *Chemistry of Materials*, vol. 33, no. 19, pp. 7755–7766, 2021.

[169] M.Y. Saïdi, J. Barker, and R. Koksbang, "Thermodynamic and kinetic investigation of lithium insertion in the $Li_{1-x}Mn_2O_4$ spinel phase", *Journal of Solid State Chemistry*, vol. 122, no. 1, pp. 195–199, 1996.

[170] Y. Xu, Y. Xu, X. Han, S. Wang, and J. Yu, "From 1D to 1D-2D-1D: new insights into Li^+ diffusion behavior in optimized MnO_2 with the cooperative effect of tunnel and interface", *Journal of Materials Chemistry A*, vol. 9, no. 43, pp. 24397–24405, 2021.

[171] J. N. Reimers and J. R. Dahn, "Electrochemical and in situ x-ray diffraction studies of lithium intercalation in Li_xCoO_2", *Journal of The Electrochemical Society*, vol. 139, no. 8, pp. 2091–2097, aug 1992.

[172] J. R. Dahn and W. R. McKinnon, "Lithium intercalation in 2H-Li_xTaS_2", *Journal of Physics C: Solid State Physics*, vol. 17, no. 24, pp. 4231–4243, 1984.